Termomehanička numerička analiza ispušnog sustava motora

Šubat, Andrej

Master's thesis / Diplomski rad

2017

Degree Grantor / Ustanova koja je dodijelila akademski / stručni stupanj: **University of Zagreb, Faculty of Mechanical Engineering and Naval Architecture / Sveučilište u Zagrebu, Fakultet strojarstva i brodogradnje**

Permanent link / Trajna poveznica: https://urn.nsk.hr/urn:nbn:hr:235:481227

Rights / Prava: In copyright/Zaštićeno autorskim pravom.

Download date / Datum preuzimanja: **2025-03-22**

UNIVERSITY OF ZAGREB

FACULTY OF MECHANICAL ENGINEERING AND NAVAL ARCHITECTURE

MASTER'S THESIS

Andrej Šubat

Zagreb, 2017

UNIVERSITY OF ZAGREB

FACULTY OF MECHANICAL ENGINEERING AND NAVAL ARCHITECTURE

THERMOMECHANICAL NUMERICAL ANALYSIS OF ENGINE EXHAUST MANIFOLD

Mentor: Student:

Prof. Zdenko Tonković, PhD   Andrej Šubat

Zagreb, 2017

Sveučilište u Zagrebu	
Fakultet strojarstva i brodogradnje	
Datum	Prilog
Klasa:	
Ur.broj:	

DIPLOMSKI ZADATAK

Student: **Andrej Šubat**   Mat. br.: 0035173047

Naslov rada na
hrvatskom jeziku: **Termomehanička numerička analiza ispušnog sustava motora**

Naslov rada na
engleskom jeziku: **Thermomechanical Numerical Analysis of Engine Exhaust Manifold**

Opis zadatka:

The structural temperatures of engine exhaust manifolds are mainly subject to the gas temperature, the geometry and either convective cooling (in case of water-cooled manifolds) or by conduction and radiation. However, it is conceivable that also the installation configuration of the engine in the vehicle has additional influence via air flow induced convection. The master thesis shall identify the differences between standard installations configurations (hot side front, hot side rear, transversal mounting, etc.) with respect to the heat exchange and the resulting structural temperature distributions. Subsequently, it shall be investigated, if the temperature difference has an actual impact on the low cycle fatigue in terms of thermomechanical fatigue (TMF). Investigation will be focused on the passenger cars only.

Based on everything said above in this study it is necessary to:

1. Study available literature on strength and thermal simulations employing finite element method.
2. Apply the thermal numerical model to a simple problem and compare the obtained results with the available theoretical ones.
3. Set-up of test models with different engine installation configurations.
4. Apply the TMF method developed by AVL-AST d.o.o. company to determine impact on thermal fatigue life:
   - Heat transfer analysis (steady state & transient over defined number of TMF cycles)
   - Nonlinear stress/strain analysis over defined number of TMF cycles
   - Damage evaluation.

During thesis preparation one must comply with the standard rules for preparation of master thesis. It is necessary to list all literature used and received assistance.

Zadatak zadan: Rok predaje rada: Predviđeni datumi obrane:

9. ožujka 2017.   11. svibnja 2017.   17., 18. i 19. svibnja 2017.

Zadatak zadao: Predsjednica Povjerenstva:

Prof. dr. sc. Zdenko Tonković   Prof. dr. sc. Tanja Jurčević Lulić

Izjavljujem da sam ovaj rad izradio samostalno, koristeći se pritom isključivo literaturom koja je citirana i navedena u popisu literature.

I hereby declare that this thesis is entirely the result of my own work, except where otherwise indicated. All used sources are given in the list of referenced literature.

Table of Contents

List of Figures

List of Tables

List of Abbreviations, Symbols and Units

Abbreviations

Abbreviation	Meaning
1D	One dimensional
2D	Two dimensional
3D	Three dimensional
AVL	Anstalt für Verbrennungskraftmaschinen List (Eng. Institute for Internal Combustion Engines List)
BC	Boundary condition
CFD	Computational fluid dynamics
EM	Exhaust manifold
FEM	Finite element method
HCF	High cycle fatigue
HS	Heat shield
HTBC	Heat transfer boundary condition
HTC	Convective heat transfer coefficient
ICE	Internal combustion engine
IP	In-phase
LCF	Low cycle fatigue
OP	Out-of-phase
RPM	Revolutions per minute
TC	Turbocharger
TMF	Thermo-mechanical fatigue

Latin symbols

Symbol	Unit	Description
a	m^2/s	Thermal diffusivity
a_i	/	Interpolation polynomials coefficients
b	/	Fatigue strength exponent (Basquin's exponent)
c	J/(kgK)	Specific heat capacity (thermal capacity)
c	/	Fatigue ductility exponent (Coffin-Manson exponent)
c_1, c_2	/	Material parameters
f	/	Function, yield function

Latin symbols - continued

Symbol	Unit	Description
g	/	Plastic potential
n	/	Number (exponent)
n'	/	Cyclic strain hardening exponent
q	W/m^2	Heat flux density
t	s	Time
Δt	s	Finite time increment
Δw	J/m^3	Plastic strain energy per cycle
u, v, w	m	Nodal displacements in Cartesian coordinate system
x, y, z	m	Cartesian spatial coordinates
A	m^2	Surface area
A_0	m^2	Initial surface area
C3D8	/	Abaqus® linear hexahedron element
C3D10	/	Abaqus® quadratic tetrahedron element
DC3D8	/	Abaqus® heat transfer linear hexahedron element
DC3D10	/	Abaqus® heat transfer quadratic tetrahedron element
DC3D15	/	Abaqus® heat transfer quadratic triangular prism element
D_f	/	Failure damage
E	N/m^2	Young's modulus (modulus of elasticity)
E_t	N/m^2	Tangent modulus
E^*	N/m^2	Cyclic modulus of elasticity
F	N	Force
Fo	/	Fourier number
G	N/m^2	Shear modulus
I_1, I_2, I_3	/	Stress invariants
J_1, J_2, J_3	/	Deviatoric stress invariants
K	/	Hardening modulus
K'	/	Cyclic hardening modulus
Mo	/	Molybdenum − chemical element
N	/	Number of cycles
N_0	/	Number of cycles for damage to initiate
N_f	/	Number of cycles until failure

Latin symbols - continued

Symbol	Unit	Description
N_i	/	Number of cycles until crack initiation
N_p	/	Number of cycles required for a crack to propagate to its critical size
N_{sta}	/	Number of cycles at which the material is stabilised
N11	˚C	Abaqus® nodal temperature
PEEQ	/	Abaqus® equivalent plastic strain
R	/	Load ratio
S	/	Surface (Solid body boundary, System boundary)
S_q	/	Surface with heat flux boundary condition
S_T	/	Surface with fixed temperature boundary condition
Si	/	Silicon – chemical element
T	˚C	Temperature
T_i	˚C	Initial temperature
T_S	˚C	Surface temperature
ΔT	˚C	Temperature difference
V	m³	Volume
c		Consistent heat capacity matrix
$\mathbf{f}_g$		Neumann boundary condition vector
$\mathbf{k}_T$		Heat conductance matrix
s		Stress deviator tensor
B		Strain-displacement matrix
C		Global consistent heat capacity matrix
D		Elastic stiffness tensor
$\mathbf{D}^{ep}$		Elasto-plastic stiffness tensor
$\mathbf{D}^{p}$		Plastic stiffness tensor
$\mathbf{F}_g$		Global Neumann boundary condition vector
q		Volume load vector
$\mathbf{q}_b$		Surface load vector
K		Global stiffness matrix
$\mathbf{K}_T$		Global heat conductance matrix
N		Shape function matrix

Latin symbols - continued

Symbol	Unit	Description
$\mathbf{N}_S$		Edge shape function matrix
$\mathbf{R}$		Global nodal force vector
$\mathbf{R}^{\text{ext}}$		Global external force vector
$\mathbf{R}^{\text{int}}$		Global internal force vector
$\mathbf{T}$		Nodal temperature matrix
$\mathbf{V}$		Global nodal displacement vector
$\overline{\mathbf{V}}$		Initial (reference) displacement vector

Greek symbols

Symbol	Unit	Description
α	W/m^2	Convective heat transfer coefficient
α_{T}	m/(mK)	Thermal expansion coefficient
δ	/	Infinitesimal variance
δ	/	Kronecker symbol
δ	m	Thickness
ε	/	Surface emissivity factor
ε	/	Strain
ε^{e}	/	Elastic strain
ε^{ep}	/	Elasto-plastic strain
ε^{p}	/	Plastic strain
$\varepsilon^{\text{mech}}$	/	Mechanical strain
$\varepsilon^{\text{therm}}$	/	Thermal strain
ε^{vp}	/	Viscoplastic strain
κ	/	Strain hardening parameter
λ	W/m	Thermal conductivity coefficient
λ	/	Lamé parameter
μ	/	Lamé parameter
ν	/	Poisson's ratio
π	/	Pi number, $\pi = 3.14159\ldots$
ρ	kg/m^3	Density
σ	W/(m^{2}K^4)	Stefan-Boltzmann constant, $\sigma = 6.6704 \cdot 10^{-8}$ W/(m^{2}K^4)
σ	N/m^2	Stress, true stress

Greek symbols - continued

Symbol	Unit	Description
σ_0	N/m^2	Engineering stress, technical stress
σ_Y	N/m^2	Yield stress, yield strength
τ	N/m^2	Shear stress
ω	/	Surface ratio
$\boldsymbol{\varepsilon}$		Strain tensor
$\boldsymbol{\sigma}$		Stress tensor

Sažetak (Abstract in Croatian)

Naslov rada: Termomehanička numerička analiza ispušnog sustava motora

Ključne riječi: Termomehanički zamor, Niskociklički zamor, Zamor ispušne grane, Metoda konačnih elemenata, Termalna analiza, Sekvencijalno spregnuta termomehanička analiza

Autor: Andrej Šubat

Raspodjela temperatura po strukturi bilo koje komponente motora s unutarnjim izgaranjem je definirana temperaturom plinova (koji predstavljaju termalno opterećenje), stanjem okoliša, geometrijom i materijalnim svojstvima te mehanizma prijenosa topline i njegovim intenzitetom. To se također odnosi i na ispušnu granu motora s unutarnjim izgaranjem te se može pretpostaviti da će konfiguracija (orijentacija) ugradnje motora u prostoru motora i pozicija ugradnje ispušne grane utjecati na raspodjelu temperatura po njenoj strukturi. Do tog učinka dolazi zbog promjene slike strujanja zraka u prostoru motora, uzrokovane gibanjem vozila, što posljedično određuje intenzitet prijenosa topline konvekcijom između ispušne grane i njenog okoliša.

Cilj ovog diplomskog rada je utvrditi razlike do kojih eventualno dolazi u pogledu intenziteta prijenosa topline i rezultirajuće raspodijele temperatura po strukturi analiziranih komponenata između tri standardne konfiguracije ugradnje motora i pozicije ispušne grane koristeći pritom metodu konačnih elemenata.

Tri standardne konfiguracije su simulirane na istom proračunskom modelu varirajući samo ambijentalne termalne rubne uvijete nametnute na površine komponenata motora koje su izložene direktnom strujanju zraka u prostoru motora.

Novo definirani i nametnuti termalni rubni uvjeti su određeni na temelju rezultata nekoliko 3D analiza strujanja zraka kroz prostor motora izvedenih primjenom računalne dinamike fluida koje je omogućila tvrtka AVL List GmbH.

U konačnici je ispitan utjecaj različite raspodijele temperatura i temperaturnih gradijenata po strukturi između ispitivanih konfiguracija na termomehanički zamor ispušne grane motora.

Numeričke simulacije procijene životnog vijeka ispušne grane, za sve konfiguracije, izvedene su prema AVL-ovoj provjerenoj proceduri za ispitivanje termomehaničkog zamora.

Simulacije provedene u okviru ovog diplomskog rada izvedene su u programskom paketu SIMULIA Abaqus® koji razvija tvrtka Dassault Systèmes.

Abstract

Thesis title: Thermo-mechanical Numerical Analysis of Engine Exhaust Manifold

Keywords: Thermo-mechanical fatigue, Low cycle fatigue, Exhaust manifold fatigue, Finite element method, Thermal analysis, Sequentially coupled thermo-mechanical analysis

Author: Andrej Šubat

Structural temperature distribution of any internal combustion engine component is defined by the gas temperature (thermal load), surrounding conditions, geometry, material properties and the overall intensity of heat exchange mechanisms. This also applies to the internal combustion engine exhaust manifold and it can be presumed that installation configuration (orientation) of the engine and the mounting position of the exhaust manifold in the engine compartment will influence structural temperature distribution. The reason behind this effect is the alteration of the underhood airflow stream, induced by vehicle motion, which defines convective mode of heat exchange process between exhaust manifold and its surrounding.

The aim of this Master's thesis is to investigate the differences between three standard engine and exhaust manifold installation configurations in passenger cars with respect to the heat exchange and the resulting structural temperature distribution using the finite element method approach.

Three standard configurations are simulated on the same finite element model by varying ambient heat transfer boundary conditions applied to surfaces exposed to underhood airflow stream.

Newly defined and applied ambient heat transfer boundary conditions are based on the results of multiple 3D computational fluid dynamics underhood airflow simulations provided by AVL List GmbH.

Finally, influence of structural temperature and structural temperature gradient variation between each model variant on exhaust manifold thermo-mechanical fatigue life is investigated. Thermo-mechanical fatigue analyses are carried out in accordance with AVL's validated and tested thermo-mechanical fatigue simulation procedure for internal combustion engines. The numerical models of internal combustion engines were also provided by AVL List GmbH.

SIMULIA Abaqus® finite element software, developed by Dassault Systèmes is used in the scope of this thesis.

Prošireni sažetak (Extended Abstract in Croatian)

Ovaj rad je izrađen u suradnji s tvrtkama AVL-AST d.o.o. iz Zagreba i austrijske tvrtke AVL List GmbH.

AVL je automobilska tvrtka koja se bavi razvojem pogonskih sklopova, uglavnom pokretanih motorima s unutarnjim izgaranjem, vrlo široke primjene. Uz to, također se bavi i razvojem različite mjerne opreme i testnih stanica za automobilsku industriju.

U ovom radu bilo je potrebno numeričkim simulacijama utvrditi razlike do kojih dolazi u pogledu intenziteta prijenosa topline i rezultirajuće raspodijele temperatura po strukturi analiziranih komponenata između tri standardne konfiguracije ugradnje motora i pozicije ispušne grane unutar prostora motora.

Tri standardne konfiguracije su simulirane na istom proračunskom modelu varirajući samo ambijentalne termalne rubne uvjete nametnute na površine komponenata motora koje su izložene direktnom strujanju zraka u prostoru motora. Novo definirani i nametnuti termalni rubni uvjeti su određeni na temelju rezultata nekoliko 3D analiza strujanja zraka kroz prostor motora provedenih primjenom računalne dinamike fluida koje je omogućila tvrtka AVL List GmbH.

Konačno, ispitan je utjecaj različite raspodijele temperatura i temperaturnih gradijenata po strukturi između ispitivanih konfiguracija na životni vijek ispušne grane motora koja je izložena cikličkom termomehaničkom opterećenju.

Termomehanički zamor ispušne grane motora

Kako bi se zadovoljili strogi propisi o maksimalnoj dopuštenoj emisiji štetnih ispušnih plinova, razvoj novih motora s unutarnjim izgaranjem još uvijek ide u smjeru smanjivanja radnog obujma motora uz zadržavanje postojećih ili čak povećavanje performansi. Taj trend je u automobilskom svijetu poznat pod imenom *downsizing*. „Izvlačenje" iste snage iz motora manjeg radnog obujma ili veće snage uz zadržavanje istog radnog obujma neminovno povećava toplinska i mehanička opterećenja svih komponenata motora.

Kao i većina komponenata motora s unutarnjim izgaranjem, komponente ispušnog sustava motora s unutarnjim izgaranjem su također pod snažnim utjecajem istovremenog toplinskog i mehaničkog opterećenja.

Istovremeni utjecaj toplinskog i mehaničkog opterećenja naziva se termomehaničko opterećenje, a ukoliko je ono još i vremenski promjenjivog karaktera tada postaje izrazito nepovoljno u pogledu životnog vijeka komponente koja je izložena takvom opterećenju.

Stoga ne čudi što je glavni razlog oštećivanja tih komponenti upravo termomehanički zamor. Uz termomehanički zamor, životni vijek komponenti ispušnog sustava motora još značajno smanjuje utjecaj oksidacije i utjecaj puzanja materijala koji nastaju kao posljedica cikličkog opterećivanja i vrlo visokih temperatura. Temperature koje postižu komponente ispušnog sustava sežu i do 1000 ˚C, a kako bi se dobio bolji uvid koliko su zaista te komponente zagrijane, na Slici 1., prikazan je motor za vrijeme testiranja na testnoj stanici.
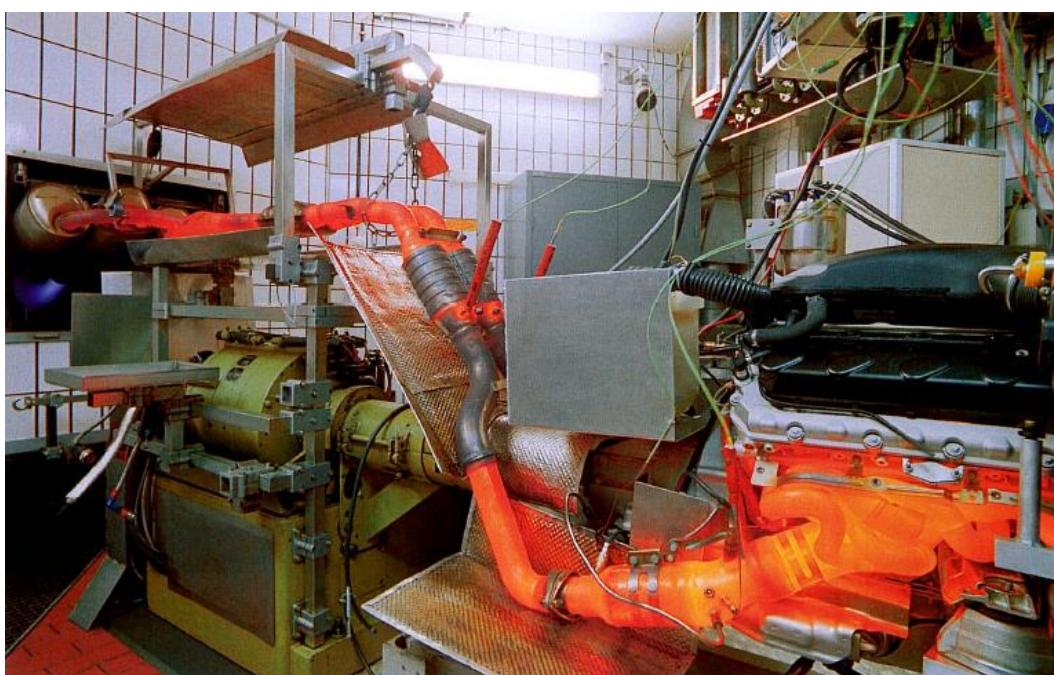
Slika 1. Ispitivanje motora na testnoj stanici [3]

Procedura evaluacije životnog vijeka ispušne grane motora

Procedura numeričkog proračuna životnog vijeka konstrukcije koji je uvjetovan termomehaničkim zamorom prikazana je na Slici 2.

```
                    ┌──────────────┐
                    │  CAD Model   │
                    └──────────────┘
        ┌──────────────┐         ┌──────────────┐
        │  MKV Model   │         │  MKE Model   │
        └──────────────┘         └──────────────┘
        ┌──────────────┐
        │ CFD Analysis │ Termalni rubni uvjeti
        └──────────────┘
                    ┌──────────────────────┐
Sekvencijalno      │ Tranzijentna termalna │
spregnuta          │       analiza         │
termomehanička     └──────────────────────┘
analiza                   Temperature
                    ┌──────────────────┐    ┌──────────────────────┐
                    │ Nelinearna analiza│◄──│ Napredni materijalni │
                    │      čvrstoće     │    │        model         │
                    └──────────────────┘    └──────────────────────┘
                         Naprezanja
                         Deformacije
                         Temperature
                    ┌──────────────────┐    ┌──────────────────┐
                    │ Proračun životnog│◄──│  Model oštećenja │
                    │       vijeka     │    └──────────────────┘
                    └──────────────────┘
                    ┌──────────────────┐
                    │ Predviđeni životni│
                    │       vijek       │
                    └──────────────────┘
```
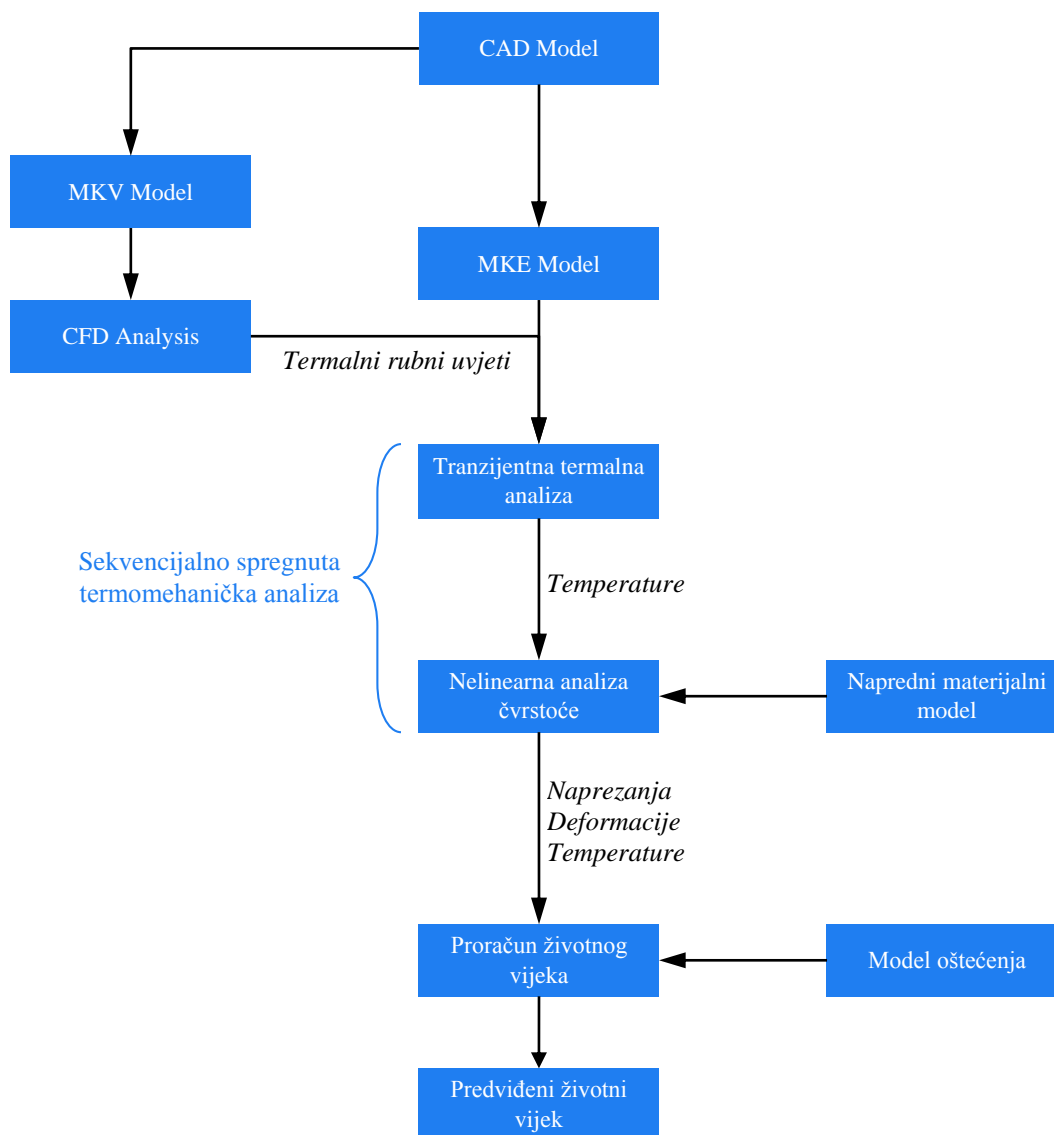
Slika 2. Generalizirani algoritam procedure numeričkog proračuna životnog vijeka konstrukcije

Zamor materijala i model oštećivanja

Zamor materijala je općenito definiran kao postupno oštećenje materijala koji je izložen vremenski promjenjivom opterećenju.

To oštećivanje materijala opisuje se prikladnim modelom oštećenja koji je može biti razvijen za pojedinačni razmatrani materijal ili za skupinu materijala sličnih mehaničkih svojstava.

Prema AVL-ovoj metodi za evaluaciju životnog vijeka ispušne grane motora smatra se da je njen maksimalni životni vijek dosegnut već prilikom pojave prve pukotine, a ne potpunim lomom konstrukcije.

To se može zapisati kao

$$N_i = N_f \tag{1}$$

gdje je N_i broj ciklusa potrebnih za iniciranje pukotine, a N_f ukupni broj ciklusa do potpunog loma konstrukcije.

Model oštećenja korišten u ovom radu za evaluaciju termomehaničkog zamora ispušne grane motora razvijen je od strane AVL-a. Točna definicija i parametri koji definiraju taj model se smatraju povjerljivim informacijama te kao takvi neće biti izneseni u potpunosti.

Model oštećenja temelji se na nekoliko parametara izračunatih tijekom zadnjeg ciklusa sekvencijalno spregnute termomehaničke analize.

Neki od parametara koji su uključeni u model oštećenja su raspon naprezanja, akumulirana viskoplastična deformacija, maksimalna temperatura i srednja temperatura.

U tom slučaju se životni vijek ispušne grane određuje kao broj ciklusa

$$N_f = N_f \left(\Delta S, \Delta \varepsilon^{vp}, T_{max}, T_{avg} \right), \tag{2}$$

gdje ΔS označava raspon naprezanja, $\Delta \varepsilon^{vp}$ akumuliranu viskoplastičnu deformaciju, T_{max} maksimalnu temperaturu, a T_{avg} srednju vrijednost temperature u zadnjem ciklusu.

Simulirane konfiguracije ugradnje motora i pozicije ispušne grane unutar prostora motora

Raspodjela temperatura po strukturi bilo koje komponente motora s unutarnjim izgaranjem je definirana temperaturom plinova (koji predstavljaju termalno opterećenje), stanjem okoliša, geometrijom i materijalnim svojstvima te mehanizma prijenosa topline i njegovim intenzitetom.

To se također odnosi i na ispušnu granu motora s unutarnjim izgaranjem te se može pretpostaviti da će konfiguracija (orijentacija) ugradnje motora u prostoru motora i pozicija ugradnje ispušne

grane utjecati na raspodjelu temperatura po njenoj strukturi. Do tog učinka dolazi zbog promjene slike strujanja zraka u prostoru motora, uzrokovane gibanjem vozila, što posljedično određuje intenzitet prijenosa topline konvekcijom između ispušne grane i njenog okoliša.

Kako bi se ispitalo koliki je taj utjecaj (i je li uopće zamjetan) simulirane su tri standardne konfiguracije ugradnje motora na istom proračunskom modelu varirajući samo ambijentalne termalne rubne uvjete nametnute na površine komponenata motora koje su izložene strujanju zraka u prostoru motora.

To znači da su mehaničke veze i ograničenja u modelu te sva nametnuta „unutarnja" toplinska opterećenja (od strane ispušnih plinova, ulja i rashladne tekućine) jednaka za sva simulirane modele.

Tablica 1. Tri simulirane konfiguracije ugradnje motora

Tri standardne konfiguracije ugradnje motora		
Varijanta	**Orijentacija motora**	**Pozicija ugradnje ispušne grane**
v00	poprečna	sa stražnje strane motora
v01	poprečna	s prednje strane motora
v02	uzdužna	s bočne strane motora
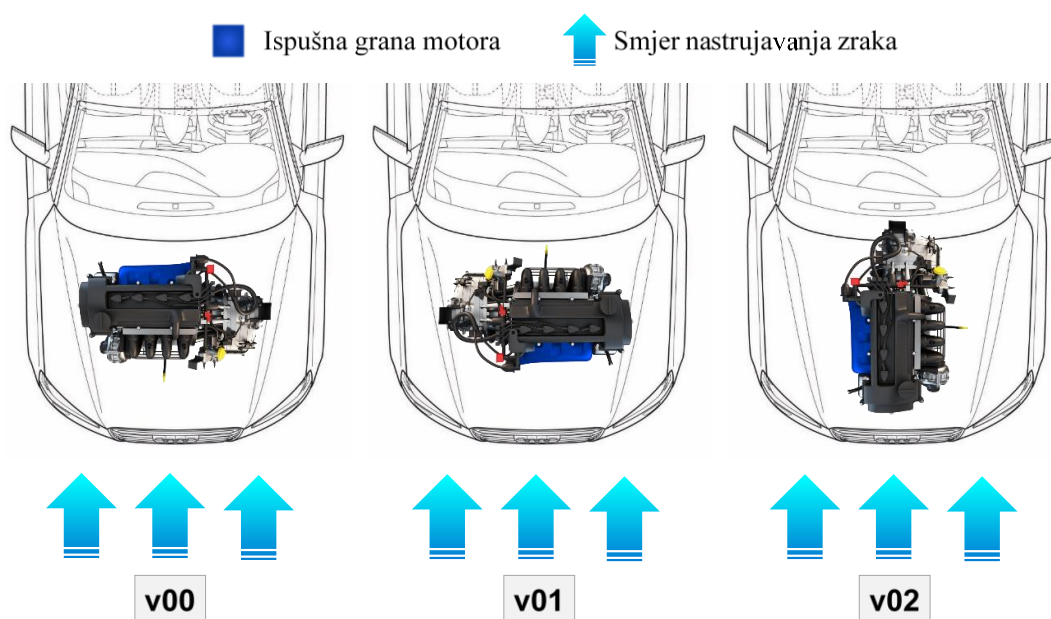
*Prikazani modeli motora i vozila su samo ilustrativne naravi!

Slika 3. Ilustracija triju simuliranih konfiguracija ugradnje motora i pozicije ispušne grane unutar prostora motora [36], [37]

Iz Slike 3. može se zaključiti da će se „slika" strujanja oko ispušna grane motora uvelike razlikovati od varijante do varijante. Također je vidljivo da će neke cijele komponente samo dijelovi tih komponenata biti nastrujavani izravnom (neometanom) strujom zraka, dok će drugi biti zaklonjeni od te struje bilo tom istom ili nekom drugom komponentom. Kako bi se to simuliralo, novi ambijentalni termalni rubni uvjeti su definirani za svaku simuliranu varijantu.

Novi ambijentalni termalni rubni uvjeti su definirani na temelju rezultata 3D analiza strujanja zraka kroz prostor motora provedenih primjenom računalne dinamike fluida koje je omogućila tvrtka AVL List GmbH.

Način na koji su novi ambijentalni rubni uvjeti definirani i nametnuti na simulirane varijante uzima u obzir i konfiguraciju ugradnje motora i brzinu vozila koja je definirana pojedinim simuliranim stanjem opterećenja.

Ambijentalni termalni rubni uvjeti nametnuti na varijantu v00 su u skladu s onima propisanim prema AVL-ovoj korištenoj i testiranoj metodi za analizu termomehaničkog zamora ispušne grane. Iz tog razloga je varijanta v00 proglašena referentnom varijantom i svi rezultati provedenih analiza su usporeeni s njom.

Trajanje simulacije i definirani termomehanički ciklus

Simulirani ciklus sačinjen je od tri pojedinačna stanja opterećenja. Ta tri stanja opterećenja opisana su u Tablici 2. Sva tri stanja opterećenja simuliraju uvjete vožnje koji su učestali prilikom normalne upotrebe automobila, ali su tako poredani da izazovu maksimalni termomehanički šok kod svih komponenti uključenih u simulacijski model.

Tablica 2. Simulirani termomehanički ciklus

Stanja opterećenja koja definiraju termomehanički ciklus		
Opterećenje	**Brzina vrtnje**	**Opis**
rated	4000 o/min	puno opterećenje, 100 km/h uzbrdo po autocesti
motored	4000 o/min	kočenje motorom, 130 km/h nizbrdo po autocesti
idle	800 o/min	prazan hod, vozilo miruje

Simulirana su ukupno tri termomehanička ciklusa te je ukupno trajanje simulacije jednako trostrukom trajanju pojedinačnog termomehaničkog ciklusa.

Numerički modeli korišteni u provedenim analizama

U numeričke modele uključena je samo „vruća" strana simuliranog motora s unutarnjim izgaranjem, tj. strana na koju su pričvršćene komponente poput ispušne grane, turbopunjača i filter krutih čestica (DPF).

Za svaku sekvencijalno spregnutu termomehaničku analizu korištena su dva numerička modela. Prvi (veći model) je korišten za toplinsku analizu dok je drugi (manji) korišten za nelinearnu analizu čvrstoće i procjenu životnog vijeka ispušne grane.

Detalji korištenih numeričkih modela prikazani su u Tablici 3. i na Slici 4.

Tablica 3. **Proračunski modeli korišteni u simulacijama**

Proračunski modeli i njihove mreže konačnih elemenata			
Proračunski model	**Broj elemenata**	**Broj čvorova**	**Korišteni elementi**
za termalnu analizu	519744	1027159	DC3D10, DC3D15
za analizu čvrstoće	288939	550841	C3D10I, C3D10M
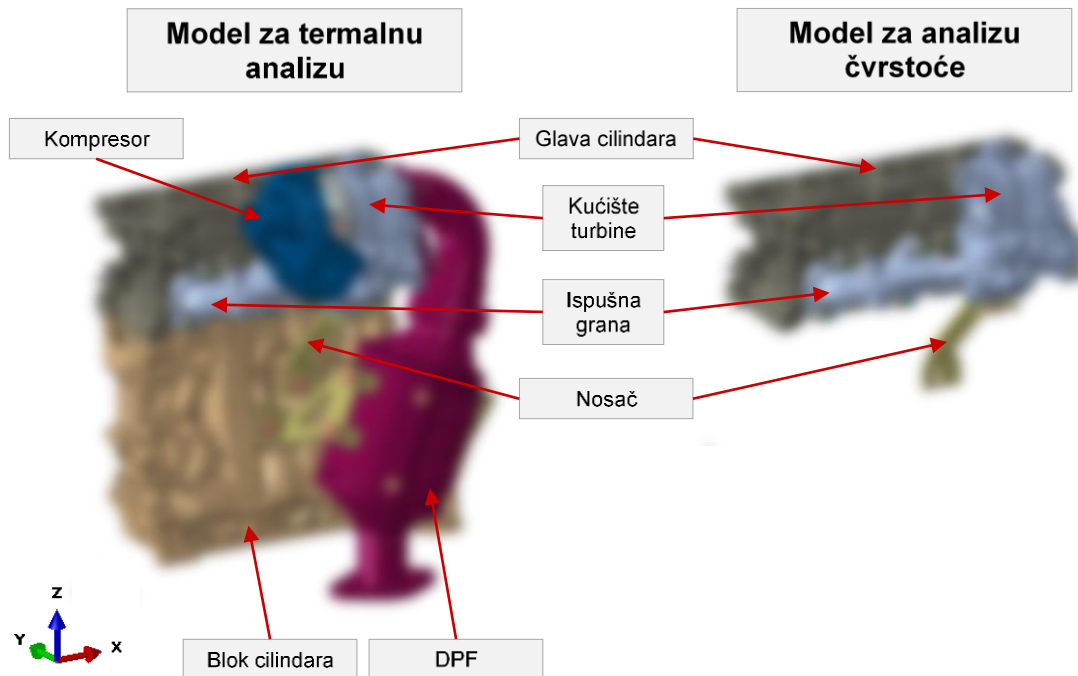
Slika 4. **Proračunski modeli korišteni u simulacijama**

Rezultati tranzijentne termalne analize

Evaluacijom rezultata tranzijentne termalne analize zaključuje se sljedeće :

- raspodjela temperatura po strukturi je u skladu s nametnutim ambijentalnim termalnim rubnim uvjetima kroz trajanje cijelog simulacijskog ciklusa,

- referentna varijanta v00 (s ispušnom granom postavljenom straga) je generalno gledajući najtoplija,

- varijanta v01 (s ispušnom granom postavljenom sprijeda) je generalno najhladnija i temperaturne razlike u odnosu na referentnu varijantu v00 su najveće,

- varijanta v02 (s bočno postavljenom ispušnom granom) je hladnija od referentne varijante v00, ali temperaturne razlike nisu tako velike kao što je to bio slučaj s v01,

- temperaturne razlike između varijanti uzrokovane varijacijom nametnutih termalnih rubnih uvjeta vidljive su kroz čitav simulirani ciklus (kroz *rated*, *motored* i *idle*),

- najveće temperaturne razlike nastaju tijekom (i na kraju) *motored* stanja opterećenja (jer se i nametnuti termalni rubni uvjeti najviše razlikuju za to stanje opterećenja),

- temperaturne razlike na kraju *idle* opterećenja su također primjetne, ali one su sada uglavnom posljedica razlika temperatura na kraju *motored* opterećenja jer su nametnuti rubni uvjeti tijekom *idle* opterećenja gotovo identični za sve varijante.
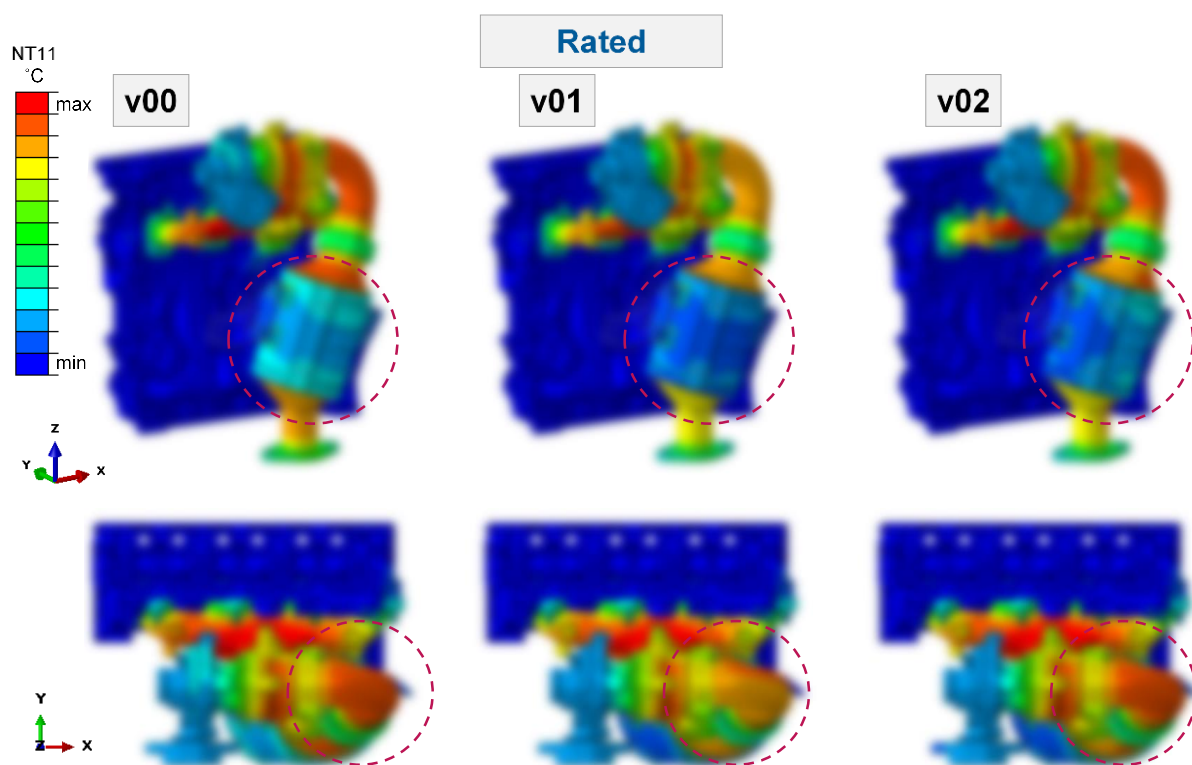
Slika 5. Utjecaj varijacije termalnih rubnih uvjeta na temperature čitavih proračunskih modela
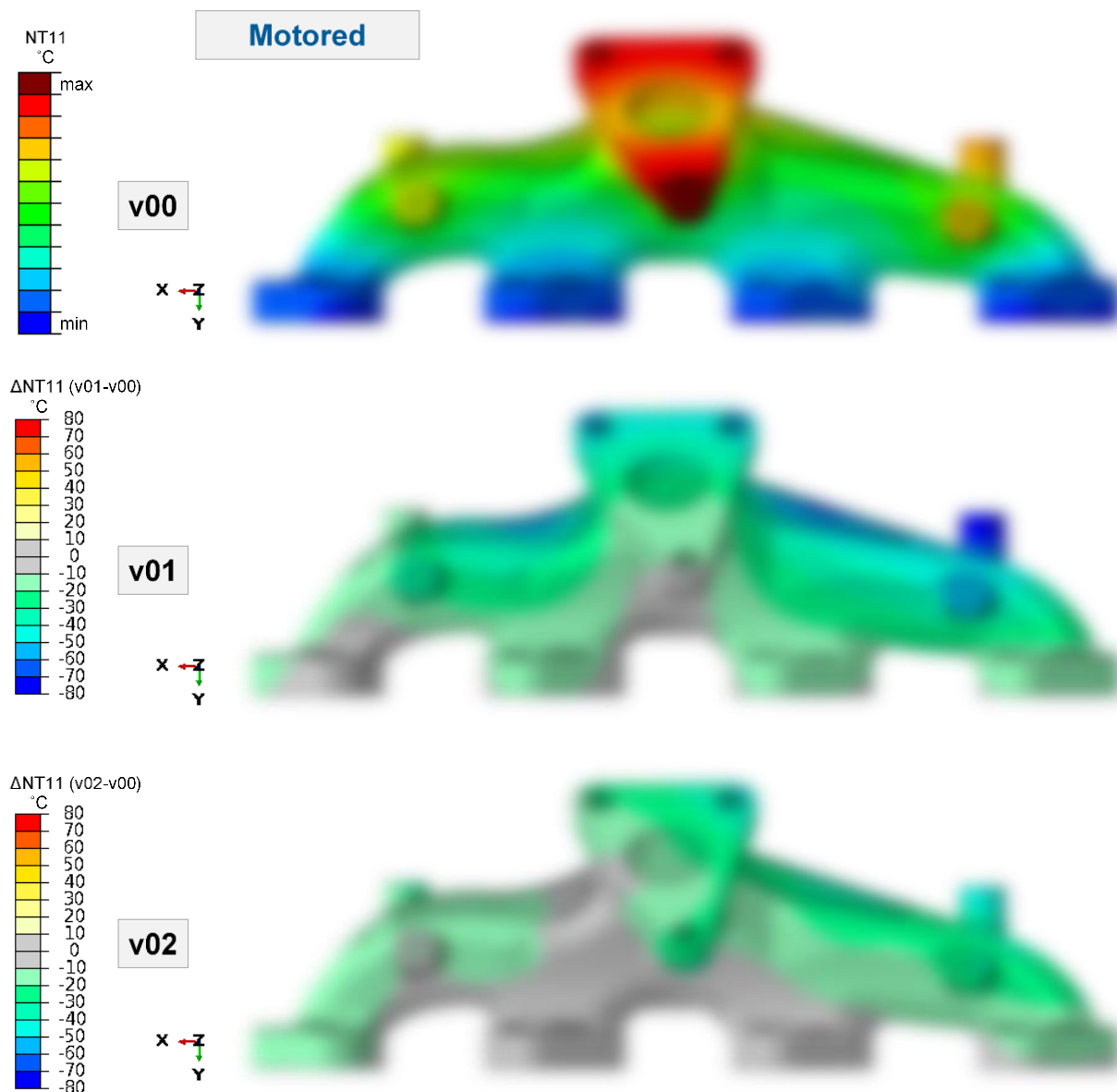
Slika 6. **Temperaturne razlike između simuliranih varijanti na kraju** *motored* **opterećenja**

Na Slikama 5. i 6. vidljiv je utjecaj varijacije termalnih rubnih uvjeta na postignute temperature i temperaturno polje, kako na čitavom proračunskom modelu tako i na samoj ispušnoj grani motora.

Vidljivo je da tamo gdje su razlike između nametnutih termalnih rubnih uvjeta značajne to rezultira i većim temperaturnim razlikama (npr. razlike na cijevi prema DPF-u ili na toplinskom štitu DPF-a, prikazano na Slici 5.).

S druge strane, gdje su rubni uvjeti slični i temperaturne razlike su manje (npr. područje ispod prirubnice prema turbopunjaču za v01 te područje lijevo i ispod te prirubnice za v02, oboje prikazano na Slici 6.)

Rezultati nelinearne analize čvrstoće

Nelinearnom analizom čvrstoće, provedenom nakon tranzijentne termalne analize i s izračunatim tranzijentnim temperaturama kao ulaznim podacima, određuju su veličine koje definiraju korišteni model oštećenja za procjenu životnog vijeka ispušne grane motora.

Te veličine su raspon naprezanja, akumulirana viskoplastična deformacija, maksimalna temperatura i srednja temperatura, izračunati u zadnjem (stabiliziranom) ciklusu.

Analiziranjem tih izračunatih veličina na ispušnoj grani motora i njihovom međusobnom usporedbom između pojedinih simuliranih varijanti može se zaključiti sljedeće:

- raspodjela raspona naprezanja na ispušnoj grani jednaka je za sve tri varijante, a razlike su vidljive samo u blagoj razlici veličine najvećih raspona naprezanja,
- raspodjela akumuliranih viskoplastičnih deformacija također je slična između varijanti, ali su sada razlike u veličinama tih raspona značajne,
- raspodjela temperatura i razlike između varijanti su već opisane u rezultatima tranzijentne termalne analize, ali može se reći da ovise o nametnutim termalnim rubnim uvjetima.

Rezultati proračuna životnog vijeka ispušne grane

Proračunom životnog vijeka ispušne grane utvrđeno je da je za svaku simuliranu varijantu, na ispušnoj grani proračunato 6 područja za koja je predviđeni broj ciklusa do iniciranja pukotine manji od dopuštenog. Minimalni dopušteni broj ciklusa do iniciranja pukotine je u ovom slučaju postavljen na 3000 ciklusa.

Lokacije svih 6 kritičnih područja se međusobno podudaraju između simuliranih varijanti što znači da je mehanizam oštećenja ostao nepromijenjen.

Sve kritične lokacije prikazane su na Slici 7. i to samo na referentnoj varijanti v00. Kritične lokacije za preostale dvije simulirane varijante nisu prikazane grafički jer se te lokacije, kako je već rečeno, podudaraju za sve tri varijante.
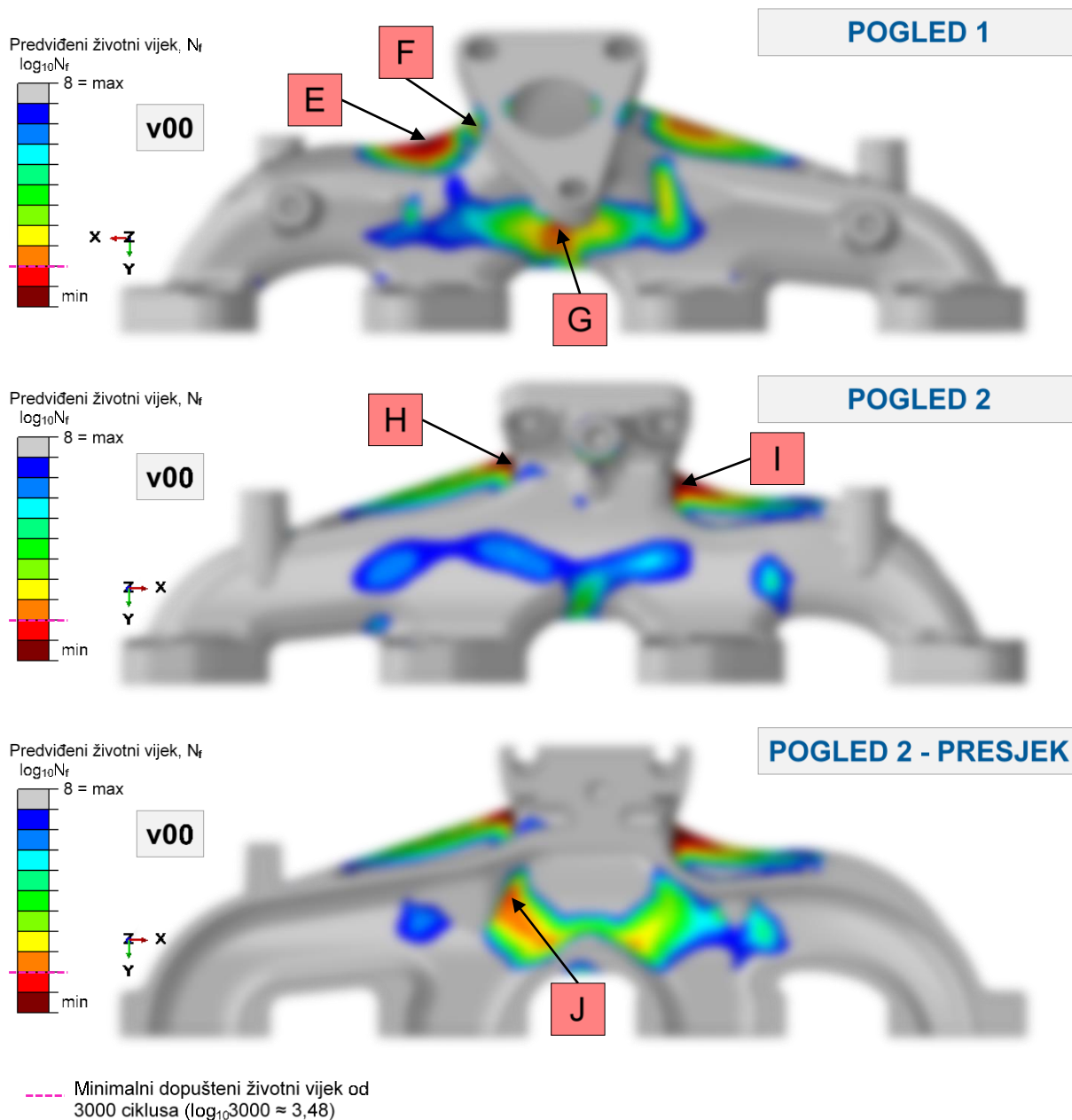
Slika 7. Životni vijek i kritične lokacije određene za referentnu varijantu v00

U nastavku su za sve simulirane varijante prikazane i uspoređene veličine izračunate na tim kritičnim lokacijama koje se odnose na procjenu životnog vijeka.

Treba još jednom napomenuti da je varijanta v00 referentna varijanta te da su sve relativne razlike izražene u odnosu na nju, u postocima.

Usporedba pojedinih rezultata prikazana je grafički na Slikama 8., 9., 10. i 11.
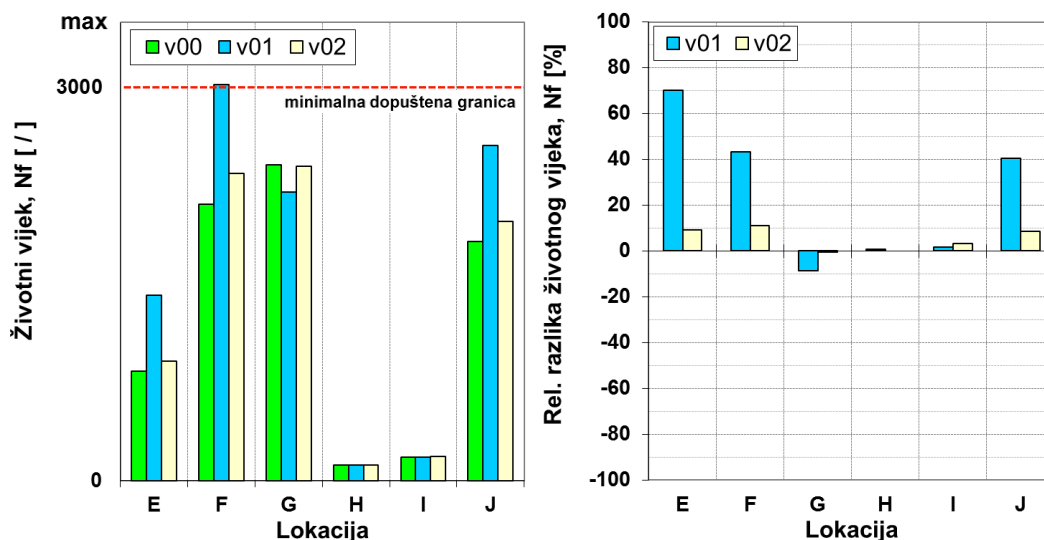
Slika 8. Usporedba procijenjenog životnog vijeka na svim kritičnim lokacijama

Općenito je na Slici 8., vidljivo da varijanta v01 (kao generalno najhladnija varijanta) predviđa najveći broj ciklusa do pojave pukotine (osim na lokaciji G), dok varijanta v00 (kao generalno najtoplija varijanta) predviđa najmanji broj ciklusa do pojave loma (osim na lokaciji G). Relativne razlike između varijanti variraju čak do 70% za lokaciju E, dok lokacije H i I gotovo ne pokazuju razliku u izračunatom broju ciklusa između varijanti.

Također, na lokacijama H i I izračunati broj ciklusa do pojave pukotine je daleko najmanji.
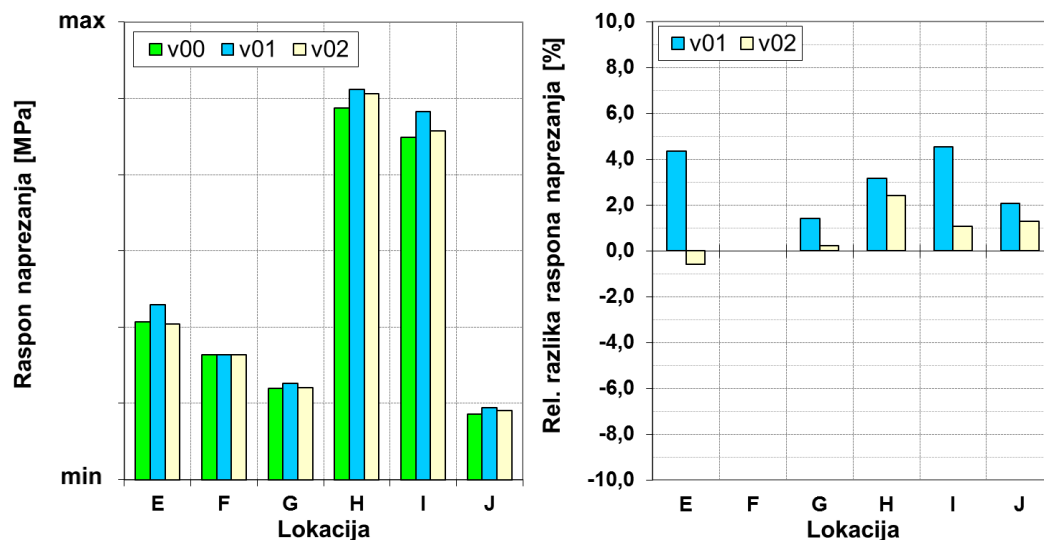
Slika 9. Usporedba izračunatog raspona naprezanja na svim kritičnim lokacijama

Razlike u rasponu naprezanja, prikazane na Slici 9., su vidljive između pojedinih varijanti, ali su manje od 5%.

Također je vidljivo da je raspon naprezanja za v01 najveći na svim lokacijama unatoč tome što je varijanta v01 generalno najhladnija. To vrijedi za sve lokacije osim na F, gdje je raspon naprezanja jednak za sve simulirane varijante. To se može objasniti time što su materijalna svojstva ispušne grane motora modelirana kao temperaturno ovisna. Smanjenjem temperature materijalu ispušne grane se povećava krutost, tj. ista deformacija pri nižim temperaturama uzrokuje veće naprezanje.

Raspon naprezanja je za lokacije H i I znatnije veći u odnosu na ostale kritične lokacije.
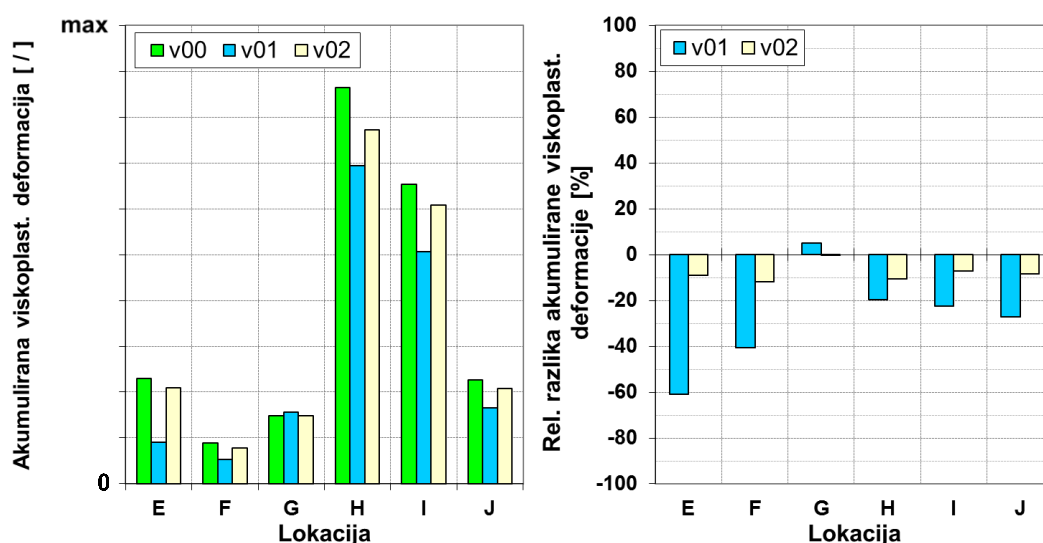
Slika 10. Usporedba izračunate akumulirane viskoplastične deformacije na svim kritičnim lokacijama

Može se primijetiti da su akumulirane viskoplastične deformacije generalno značajno niže za varijantu v01 (generalno najhladniju varijantu) na svim kritičnim lokacijama osim G, dok su vrijednosti akumulirane viskoplastične deformacije generalno najveće za varijantu v00 (generalno najtopliju varijantu) na svim lokacijama osim G.

Relativne razlike između akumulirane viskoplastične deformacije za posljednji simulirani ciklus su značajne i sežu do čak 61% između v00 i v01 za lokaciju E.

Akumulirane plastične deformacije na lokacijama H i I veće su čak i do 4 puta nego one na ostalim kritičnim lokacijama.
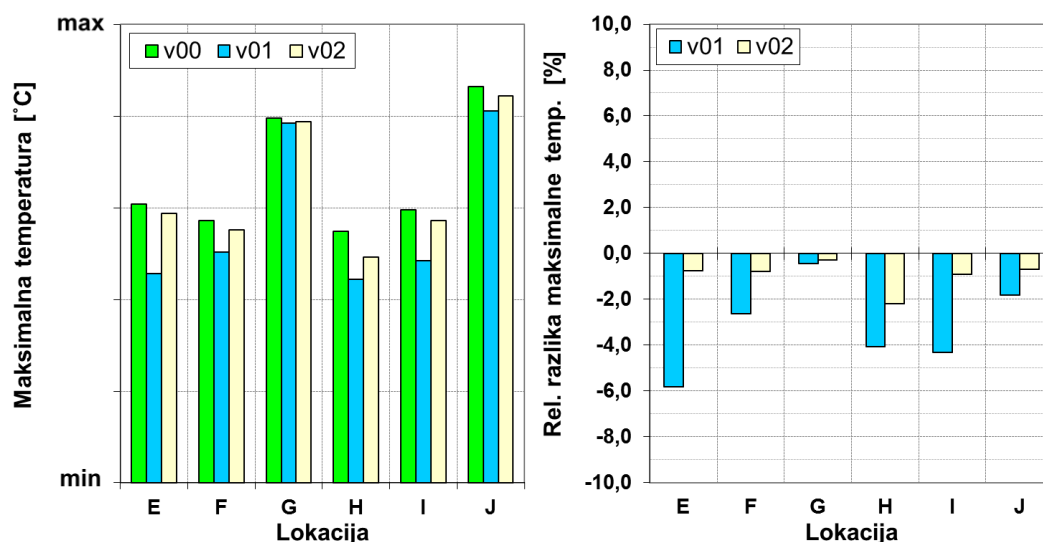
Slika 11. Usporedba izračunate maksimalne temperature na svim kritičnim lokacijama

Sa Slike 11. je vidljivo da su relativne razlike u maksimalnim temperaturama na kritičnim lokacijama vidljive. Između varijanti v00 i v01 one sežu do 6%, a između v00 i v02 do 2%. Najmanje vrijednosti maksimalnih temperatura su izračunate za varijantu v01 na svim kritičnim lokacijama što je i u skladu s zaključkom donesenim na temelju rezultata tranzijentne termalne analize da je varijanta v01 generalno najhladnija.

Kako je vidljivo u Tablici 4., nakon evaluacije podataka sa svih kritičnih lokacija, još uvijek nije moguće donijeti jedinstven zaključak o utjecaju ambijentalnih termalnih rubnih uvjeta na izračunati broj ciklusa do pojave pukotine.

Općenito može se zaključiti da sniživanje temperature pozitivno utječe na izračunati broj ciklusa do loma, ali taj utjecaj drastično varira od jedne do druge kritične lokacije.

Značajan utjecaj sniživanja temperature na poboljšanje životnog vijeka je vidljiv na lokaciji E (i u manjoj mjeri na F i J), gdje relativna negativna temperaturna razlike od 6% uzrokuje povećanje izračunatog broja ciklusa za čak 70%.

Nasuprot tome, relativna negativna temperaturna razlika od 4% na lokacijama H i I uzrokuje zanemarivo poboljšanje u pogledu broja ciklusa od samo 1% za H, odnosno 2% za I.

Lokacija G se ne slaže s ovom pretpostavkom. Ona se naime, ponaša suprotno od očekivanog gdje smanjenje temperature (iako blago) rezultira i smanjenjem izračunatog broja ciklusa do pojave pukotine.

Tablica 4. Usporedba rezultata provedenog termomehaničkog proračuna za sve kritične lokacije

Termomehanički zamor i vrijednosti parametara koji utječu na njega								
Lok.	Var.	Ž. vijek N_f [ciklusa]	Rel. raz.	Raspon naprezanja [MPa]	Rel. raz.	Raspon viskoplast. def.	Rel. raz.	Max. temp. [°C]	Rel. raz.
E	v00	800*		**		**		**	
	v01	1400*	70,1%	**	4,3%	**	-60,8%	**	-5,8%
	v02	900*	9,2%	**	-0,6%	**	-9,1%	**	-0,8%
F	v00	2100*		**		**		**	
	v01	3000*	43,1%	**	0,0%	**	-40,7%	**	-2,6%
	v02	2300*	11,1%	**	0,0%	**	-11,9%	**	-0,8%
G	v00	2400*		**		**		**	
	v01	2200*	-8,7%	**	1,4%	**	4,9%	**	-0,4%
	v02	2400*	-0,5%	**	0,2%	**	0,0%	**	-0,3%
H	v00	100*		**		**		**	
	v01	100*	0,8%	**	3,2%	**	-19,7%	**	-4,1%
	v02	100*	0,0%	**	2,4%	**	-10,6%	**	-2,2%
I	v00	200*		**		**		**	
	v01	200*	1,7%	**	4,5%	**	-22,4%	**	-4,3%
	v02	200*	3,4%	**	1,1%	**	-7,1%	**	-0,9%
J	v00	1800*		**		**		**	
	v01	2600*	40,3%	**	2,1%	**	-27,1%	**	-1,8%
	v02	2000*	8,6%	**	1,3%	**	-8,4%	**	-0,7%
*zaokruženo na najbliži višekratnik broja 100, **povjerljivi podaci								

Konačno se može zaključiti slijedeće:

- Broj ciklusa do iniciranja pukotine na kritičnim lokacijama nije određen samo temperaturom. Također na njega značajno utječu efekti lokalne krutosti te globalnog ponašanja ispušne grane motora i komponenata s kojima je u interakciji.

- Generalno gledajući, bolje hlađenje ispušne grane motora (kao što je bio slučaj s varijantom v01) pozitivno utječe na predviđeni životni vijek (osim na kritičnim lokacijama kod kojih je utjecaje lokalne krutosti velik).

Referentna varijanta, koja je simulirana prema postojećoj AVL-ovoj proceduri za evaluaciju životnog vijeka ispušne grane, pokazala se kao najkonzervativnija. Time se inženjere dovodi u nešto povoljniji položaj što se tiče sigurnosti.

1. Introduction

This Master's thesis is written in collaboration with AVL-AST d.o.o. from Zagreb and AVL List GmbH from Graz.

AVL is an automotive consulting company and independent research institute. It is the world's largest privately owned company for the development of powertrain systems with internal combustion engines as well as instrumentation and test systems.

1.1.   Engine Development Process and Demands [1]

Demands on all cutting edge products and services are stronger than ever. Trend changes are fast and competition is fierce in all fields of industry. The automotive industry is no exception when it comes to this so the respective product development has to be superb in order to stay competitive.

It can be said that the automotive industry's motto is "faster – better – lighter – safer – cheaper". In order to live up to it, any successful automotive company has to

- be able to make correct decisions early in the design cycle,
- reduce or possibly eliminate trial and error procedure in the development process,
- reduce the cost of materials by using them to their full potential,
- increase product reliability through improvements of manufacturing processes and
- reduce design and manufacturing costs [2].

In order to comply with stringent vehicle emissions standards and regulations, the engine displacement downsizing trend is still viable and widely used option. Downsizing also implies upgrading the performance of smaller displacement engines which results in a respective increase of mechanical and thermal loads. On the other hand, the demand for increased engine lifetime is constantly becoming higher, which makes durability requirements even harder to meet.

Engine and exhaust system components must withstand severe cyclic mechanical and thermal loads throughout their life time. In the past, no reliable methods have been available for calculating the lifetime of a component under these complex loading conditions. Therefore,

numerous expensive and very time-consuming bench and field tests were necessary for the development of a component or an engine [3].

Bench tests are very effective at simulating real world conditions and they surely won't become entirely obsolete in the foreseeable future. One of their main disadvantages is that they require a physical prototype for testing which means that they cannot be implemented early enough into the design process. In today's fast-evolving automotive industry, this is a considerable drawback.

A test bed setup during engine testing, with glowing high temperature exhaust system components, is shown in Figure 1.1.
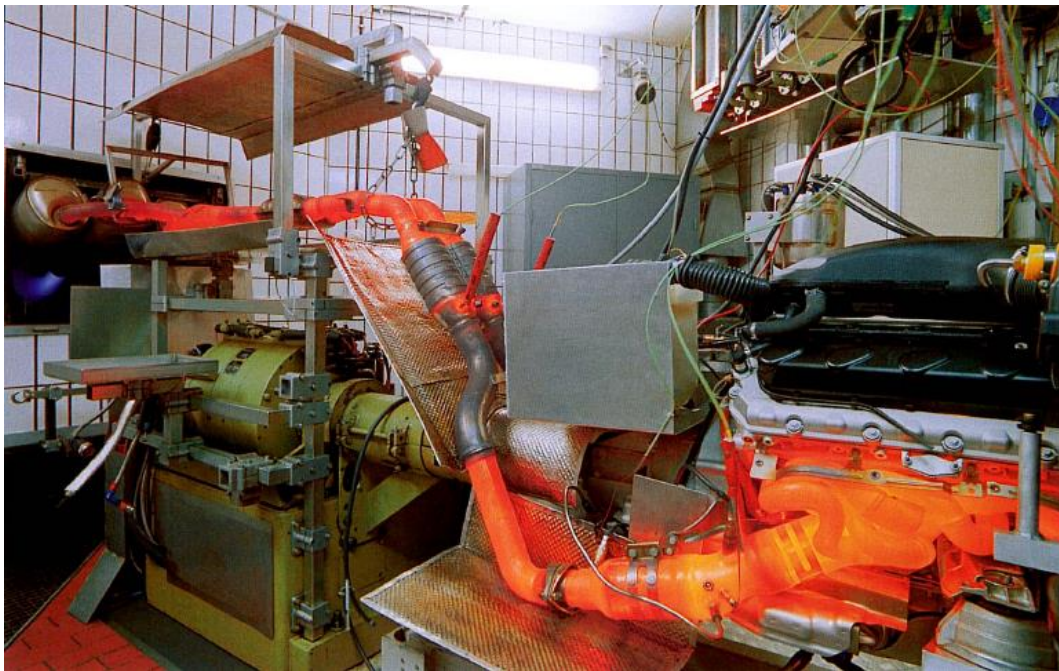
Figure 1.1. Test bed setup [3]

It has been realized that in order to speed up the engine development process advanced simulation technologies can be a very powerful tool, especially if they are introduced and efficiently used from the very beginning of engine development process.

Numerical computer simulations of engine operation and its associated durability tests are generally less time consuming than test bed engine testing, especially with the high processing and computing power available today. Another key advantage is that simulations don't rely on availability of costly prototypes or any other hardware parts. This allows investigation and

validation of design variants from various points of view. The fact that simulation is based on models rather than real parts, removes the major obstacles for making early, result based, design changes which are otherwise generally highly time consuming and costly. For that purpose, the "virtual engine" concept has been defined in the automotive industry. Its aim is to predict the engine behaviour solely by virtual means.

Durability simulation of the engine under real or well-defined test load operating conditions is also an area which can be performed using the virtual engine concept. Fatigue durability problems can be distinguished as either high cycle fatigue (HCF) or low cycle fatigue (LCF) problems. Cyclic loading of engine components by alternating gas pressure forces can be categorised as an example of high cycle fatigue problem. Low cycle fatigue problems are often related to complex thermo-mechanical load cycling. Fast and large amplitude thermo-mechanical cycles are most likely to occur during engine start-stop or during the sudden changes in engine load conditions. Cylinder heads and exhaust manifolds are two examples in which LCF failure usually occurs due to cyclic thermo-mechanical loading.

Thermo-mechanical fatigue (TMF) lifetime simulation process combines fields of thermodynamics (combustion and heat transfer), fluid dynamics, nonlinear deformable body mechanics and material science. Complete TMF simulation process is a combination of successive or iterative analysis steps of multiple physics problems.

Even though, the virtual engine concept is today widely used in the automotive industry, it can be said that it is still a work in progress. A lot of time, money and knowledge will have to be poured into its development before it will be able to achieve the same or better level of accuracy and credibility associated with real-life product or prototype testing.

1.2. Thesis Outline

Engine installation orientation and exhaust manifold (EM) mounting position greatly influences and alters the airflow in the engine compartment induced by vehicle motion. This is more noticeable at higher vehicle speeds which result in increased underhood airflow mass.

The heat transfer (HT) process between engine components and their ambient (surrounding), in this case the engine compartment and the underhood airflow, is defined with the following parameters:

- Convective part of HT: geometry (surface), component surface temperature, surrounding media (airflow) temperature and convective heat transfer coefficient.
- Radiative part of HT: geometry (surface), component surface temperature, surrounding surfaces temperatures and emissivity coefficient between them.

These parameters fully define heat transfer boundary conditions (HTBC's).

The structural temperature distribution of any internal combustion engine component is defined by material properties and imposed thermal loads, as well as heat transfer boundary conditions.

The fluctuation of structural temperatures in time and the gradient of this fluctuation is a key element in definition of any thermo-mechanical load cycle.

Having that in mind, it can now be said that the main goal of this thesis is to answer the question of whether, and if yes, to which extent the ambient HTBC's variation influences the exhaust manifold TMF life.

In order to answer this question, three standard engine installation configurations will be simulated by varying only the ambient HTBC's applied to surfaces exposed directly to the underhood airflow stream (induced by vehicle motion and radiator fans).

Thermal loads from the inner (gas, water and oil) side and also the mechanical loads and constraints will remain the same for all investigated configurations. This ensures that analyses results are directly comparable.

Ambient HTBC's which will be applied to the model variants will vary based on the results of multiple 3D CFD underhood simulations provided by AVL.

Finite element method (FEM) TMF life prediction simulations will be carried out in accordance with the existing, thoroughly validated and tested, AVL's TMF simulation procedure.

1.3. Thesis overview

A TMF analysis requires good knowledge and understanding of all physical phenomena which occur during engine operation on both macro and micro level.

For that reason, Chapter 2 and Chapter 3 cover the basic concepts from areas of thermodynamics, nonlinear deformable body mechanics, fatigue life prediction and the finite element method. In Chapter 3, two simple heat transfer problems are solved both analytically and using FEM for verification purposes. Chapter 4 outlines the TMF analysis process and it shows numerical models used for TMF simulation in more detail. In the final two chapters, Chapter 5 and Chapter 6, the analyses results along with conclusions and recommendations for possible further actions are given.

2. Theoretical Framework

Thermo-mechanical fatigue (TMF) is caused by combined thermal and mechanical loading where both the stresses and temperatures vary with time. In order to fully understand it, the basic concepts of thermodynamics and also the basic concepts of mechanics of deformable bodies have to be laid out.

2.1. Thermodynamics

Heat is energy that is spontaneously transferred between a system and its surrounding or other systems through the boundaries of those systems. The rate of heat transfer (HT) is dependent on the temperatures of the interacting systems and the properties of the intervening medium through which the heat is transferred.

Heat problems are solved to obtain the temperature field, heat fluxes, heat losses, etc. HT problems can be analysed as steady state or transient, linear or nonlinear problems.

In steady state HT problems boundary conditions (BC's) and material properties are not time dependent. On the contrary, in transient HT problems, BC's or material properties are time dependent and also the time dependent change of internal energy is included into energy balance equation [4].

2.1.1. Heat Transfer Modes [5], [6]

There are three fundamental modes of heat transfer:

1. Conduction or diffusion
2. Convection
3. Radiation

2.1.1.1.   Conduction or diffusion

It happens on a microscopic scale when hot, rapidly moving or vibrating atoms and molecules interact with neighbouring atoms and molecules, transferring some of their energy (heat) to these neighbouring particles. Heat is transferred by conduction when adjacent atoms vibrate against one another, or as electrons move from one atom to another. Conduction is the most significant means of HT within a solid object or between solid objects in direct thermal contact.

Conduction is defined with geometrical and material properties of a system and temperature difference between the points of interest.

2.1.1.2.   Convection

The transfer of heat from one place to another by the movement of fluids, a process that is essentially the transfer of heat via mass transfer. Since movement of particles constitutes convection, it is the macro form of HT. Also convection is only possible in fluids where the particles can move easily. Convection can be of two types: (*i*) natural convection where the movement of particles which constitutes convection occurs by the variation in densities of the fluids and (*ii*) forced convection when the streams and currents in the fluid are induced by external means which create an artificially induced convection current.

Convection is defined with geometrical properties of a system, temperature of the solid object surface, temperature of the fluid and the convective heat transfer coefficient between them.

Convective heat transfer coefficients depend on multiple physical properties of a system. Those properties are:

> solid object surface geometry and temperature, flow properties (determined by the solid object surface geometry and flow velocity) and flowing media properties (pressure, density, viscosity, temperature, specific heat capacity, conductance).

The convective heat transfer coefficient is usually determined using empirical correlations derived from the measurements taken for different geometries and flow conditions.

2.1.1.3.   Radiation

This mode of heat transfer HT doesn't require any medium to occur. Every matter having a temperature above absolute zero will emit energy in the form of electromagnetic waves.

It is defined with geometrical properties of a system and temperatures and emissivity coefficients of interacting objects surfaces.

2.1.2. Basic Heat Transfer Analyses Equations [7]

Temperature field in transient HT analysis is a function of both spatial coordinates (*x, y, z*) and time *t* and can be written as

$$T = f\left(x, y, z, t\right). \tag{2.1}$$

By inserting the Fourier law of heat conduction

$$q_{\mathrm{S}} = -\lambda \frac{\delta T}{\delta n}, \tag{2.2}$$

with λ being thermal conductivity and $\dfrac{\delta T}{\delta n}$ being temperature gradient, into the transient HT equation without heat source for control volume *V* bounded by an arbitrary surface *S* we get

$$\frac{\partial}{\partial x}\left(\lambda_x \frac{\partial T}{\partial x}\right) + \frac{\partial}{\partial y}\left(\lambda_y \frac{\partial T}{\partial y}\right) + \frac{\partial}{\partial z}\left(\lambda_z \frac{\partial T}{\partial z}\right) = \rho c \frac{\partial T}{\partial t}, \tag{2.3}$$

where ρ is material density and *c* specific heat capacity.

Since all components of interest in this thesis can be considered as homogenous, material conductivity is not a function of spatial coordinates, therefore Equation (2.3) can be written as

$$\lambda\left[\frac{\partial^2 T}{\partial x^2} + \frac{\partial^2 T}{\partial y^2} + \frac{\partial^2 T}{\partial z^2}\right] = \rho c \frac{\partial T}{\partial t}. \tag{2.4}$$

2.1.3. Initial and Boundary Conditions [4]

In order to solve the differential equation, initial and boundary conditions have to be defined. Initial conditions represent temperature distribution throughout a solid body at time $t = 0$ as a function of spatial coordinates

$$T_{\mathrm{i}} = T_{\mathrm{i}}\left(x, y, z, t = 0\right). \tag{2.5}$$

Boundary conditions describe the interaction between bounding surface of a solid body S (system) and its surrounding.

There are three types of boundary conditions:

1. Dirichlet boundary conditions (fixed boundary conditions) – temperatures are defined in each moment on bounding surface S_T as $T_S = T_S(x, y, z, t)$.

2. Neumann (Cauchy) boundary conditions – heat fluxes are defined in each moment on the bounding surface S_q as $q_S = q_S(x, y, z, t), \quad \left(q_S = -\lambda \dfrac{\partial T}{\partial n} \right).$

3. Newton mixed boundary conditions – solid body exchanges heat with the surrounding fluid what can be written as $q_S = \alpha_{\mathrm{comb}}(T_S - T_\infty),$

   where α_{comb} is combined heat transfer coefficient, implying both the convection and radiation effects, T_S is the solid body surface temperature, T_∞ is fluid temperature away from the solid body surface.
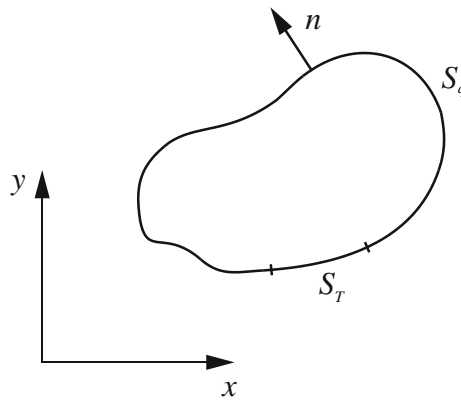
Figure 2.1. Solid body bounding surface

2.2. Mechanics of Deformable Bodies [4], [8], [9], [10], [11], [12]

2.2.1. Stress-Strain Curve

Stress-strain relation can be obtained by simple tensile or compressive experiments. If force F is divided by initial cross-sectional area A_0 the result is engineering (technical) stress σ_0. True stress σ is the ratio of force F and real cross-sectional area A at the narrowest region of the neck. In tensile experiments, real cross-sectional area A gets smaller compared to initial cross-sectional area A_0 due to the Poisson effect which means that real stress will be larger than engineering stress. If the stress–strain curve is plotted in terms of true stress and true strain the stress will continue to rise until failure. True stress - true strain curve is shown in the Figure 2.2.
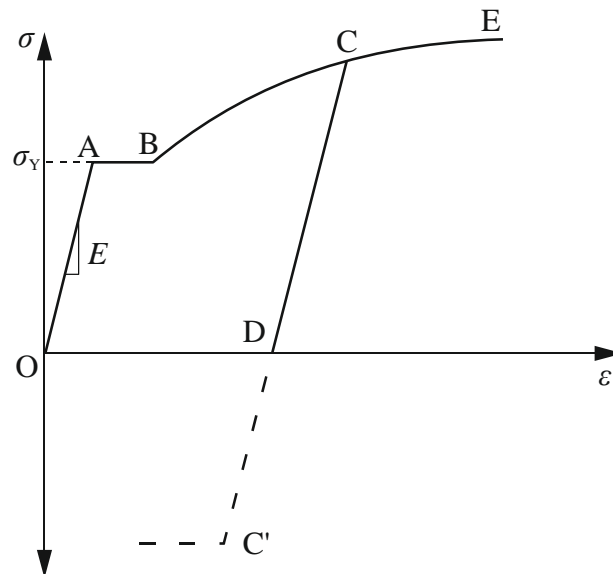
Figure 2.2. True stress – true strain curve

Curve starts as a straight line describing linear elastic part where stress is directly proportional to strain (Hooke's law). Point A represents the yield strength (and in this case also the proportionality limit) and beyond that point permanent (plastic) deformation will occur. Segment AB represents the flow region in which strain increases without stress increase. Beyond the flow limit B stress increase occurs due to strain hardening until fracture point E is reached.

If the specimen is relaxed in point C, elastic contraction CD will occur with the slope closely matching E (Young's modulus) resulting in permanent plastic deformation OD. By stretching

the specimen again from the point D material will behave similarly to the curve DCE. Clearly, the elastic strain part is now bigger and $\sigma_Y^C > \sigma_Y^A$ meaning that the yield strength has increased. If the specimen is compressed from the point D material will undergo elastic deformation up until the point C'. New yield strength will be much smaller than the one in the point C, $\sigma_Y^C > \sigma_Y^{C'}$. This phenomenon is called the Bauschinger effect.

2.2.2. Total Strain

The total strain tensor for thermo-mechanical fatigue can be written as

$$d\varepsilon_{ij} = d\varepsilon_{ij}^e + d\varepsilon_{ij}^p + d\varepsilon_{ij}^{\text{therm}} = d\varepsilon_{ij}^{\text{mech}} + d\varepsilon_{ij}^{\text{therm}} \ , \tag{2.6}$$

where upper indices "e", "p", "therm" and "mech" denote elastic strain, plastic strain, thermal strain and mechanical strain, respectively.

2.2.2.1.   Elastic Strain

Stress strain constitutive equation for linear elastic deformation can be written as

$$\sigma_{ij} = D_{ijkl}\varepsilon_{kl}^e , \tag{2.7}$$

where D_{ijkl} is elasticity tensor of fourth order while stress and strain tensors are of second order.

In general case (anisotropic materials), D_{ijkl} consists of 36 coefficients which can be described with 21 independent material constant. For isotropic materials number of independent material constants is reduced to only two: Young's modulus E and shear modulus G which are connected with the following relation

$$\frac{E}{G} = 2(1+\nu), \tag{2.8}$$

where ν is the Poisson's ratio.

Elasticity tensor for isotropic material can be written as

$$D_{ijkl} = \lambda \delta_{ij}\delta_{kl} + \mu\left(\delta_{ik}\delta_{jl} + \delta_{il}\delta_{jk}\right), \tag{2.9}$$

with λ and μ being Lamé parameters

$$\lambda = \frac{\nu E}{\left(1+\nu\right)\left(1-2\nu\right)}, \quad \mu = G = \frac{E}{2\left(1+\nu\right)} \tag{2.10}$$

and δ_{ij} being Kronecker symbol.

Kronecker symbol takes values according to the following agreement:

$$\delta_{ij} = \begin{cases} 1, & i = j \\ 0, & i \neq j \end{cases}. \tag{2.11}$$

2.2.2.2. Plastic Strain and Yield Criteria

In case there are no initial strains, total strains can be written as

$$d\varepsilon_{ij} = d\varepsilon_{ij}^{\mathrm{e}} + d\varepsilon_{ij}^{\mathrm{p}}, \tag{2.12}$$

while constitutive Equation (2.7) can now be written as

$$d\sigma_{ij} = D_{ijkl}\left(d\varepsilon_{kl} - d\varepsilon_{kl}^{\mathrm{p}}\right). \tag{2.13}$$

Term σ_{ij} in the Equation (2.13) represents Cauchy stress tensor and term ε_{ij} represents Lagrange strain tensor which can be expressed as

$$\varepsilon_{ij} = \frac{1}{2}\left(\frac{\partial u_i}{\partial u_j} + \frac{\partial u_j}{\partial u_i} + \frac{\partial u_k}{\partial u_i}\frac{\partial u_k}{\partial u_j}\right). \tag{2.14}$$

Stress tensor σ_{ij} can be expressed as the sum of two other stress tensors. First one is mean hydrostatic stress tensor or volumetric stress tensor σ_{kk} which tends to change the volume of a stressed body and the second one is deviatoric component called the stress deviator tensor s_{ij} which tends to distort it. This can be written as

$$\sigma_{ij} = \frac{1}{3}\sigma_{kk}\delta_{ij} + s_{ij}. \tag{2.15}$$

For the materials included in the scope of this thesis there is no volume change during plastic deformation, thus only deviatoric component s_{ij} is relevant for plastic deformation.

Critical loading condition for uniaxial loading after which plastic deforming begins is determined by the yield strength. Under multiaxial loading condition this is determined by the yield function

$$f = f\left(\sigma_{ij}, \varepsilon_{ij}^{\mathrm{p}}, \kappa\right), \tag{2.16}$$

expressed as a function of stress σ_{ij}, plastic strain $\varepsilon_{ij}^{\mathrm{p}}$ and strain hardening parameter κ which depends on the change of plastic strain.

Yield function expressed as

$$f\left(\sigma_{ij}, \varepsilon_{ij}^{\mathrm{p}}, \kappa\right) = 0, \tag{2.17}$$

represents an implicit equation of a closed hyperbola called yield surface.

Every stress state at some point within a solid body is characterised by a single point in the principal stress space. If that point is inside the yield surface, $f < 0$, then the material is in an elastic stress state and plastic strains are not increasing. Plastic strains occur only if $f = 0$, while $f > 0$ has no physical meaning.

For isotropic elastic - perfectly plastic, i.e. non-strain hardening material, yield function is only function of stresses

$$f\left(\sigma_{ij}\right) = 0\,. \tag{2.18}$$

Yielding in isotropic materials depends only on the values of the principal stresses $\sigma_1, \sigma_2, \sigma_3$ and not on their directions because all directions are equally valued.

$$f\left(\sigma_1, \sigma_2, \sigma_3\right) = 0\,. \tag{2.19}$$

Equation (2.19) can be also written as

$$f\left(I_1, J_2, J_3\right) = 0\,, \tag{2.20}$$

where I_1 is first stress invariant and J_2, J_3 are second and third deviatoric stress invariants respectively.

Stress invariants are:

$$
\begin{aligned}
I_1 &= \sigma_{ii}, \\
I_2 &= \frac{1}{2}\sigma_{ij}\sigma_{ij}, \\
I_3 &= \frac{1}{3}\sigma_{ij}\sigma_{jk}\sigma_{ki}.
\end{aligned}
\tag{2.21}
$$

Invariants of deviatoric deviator tensor are:

$$
\begin{aligned}
J_1 &= s_{ii}, \\
J_2 &= \frac{1}{2}s_{ij}s_{ij}, \\
J_3 &= \frac{1}{3}s_{ij}s_{jk}s_{ki}.
\end{aligned}
\tag{2.22}
$$

The experimental facts show that yielding is unaffected by uniform hydrostatic tension or compression. This means that yield surface is only function of second and third invariant of the stress deviator tensor

$$f\left(J_2, J_3\right) = 0. \tag{2.23}$$

Geometrical representation of von Mises and Tresca yield criteria is shown in Figure 2.3. Von Mises yield surface is corresponding to a circular cylinder while Tresca yield surface corresponds to six-sided prism. The axis equally inclined to all three principal stress axes is called hydrostatic axis. In all the points of this axis all three principal stresses are equal. The plane perpendicular to the hydrostatic axis is called π-plane and it can be expressed as

$$\sigma_1 + \sigma_2 + \sigma_3 = 0. \tag{2.24}$$

All planes parallel to the π-plane, including the π-plane, are deviatoric planes. Yield surface and π-plane intersect in a curve called yield curve or yield locus. The yield surface represents the yielding criterion.

Any stress state vector in principal stress space can be divided into two components. First one is hydrostatic stress component which is coincident with hydrostatic axis and the second one is deviatoric stress component which lies in the π-plane. As stated above, the hydrostatic stress has no effect on yielding. So, yielding can depend only on the characteristics of the deviatoric stress component. Any stress state in which the stress point lies on the yield surface corresponds to the state of yielding. Any stress point that lies inside of this surface corresponds to the elastic stress state.
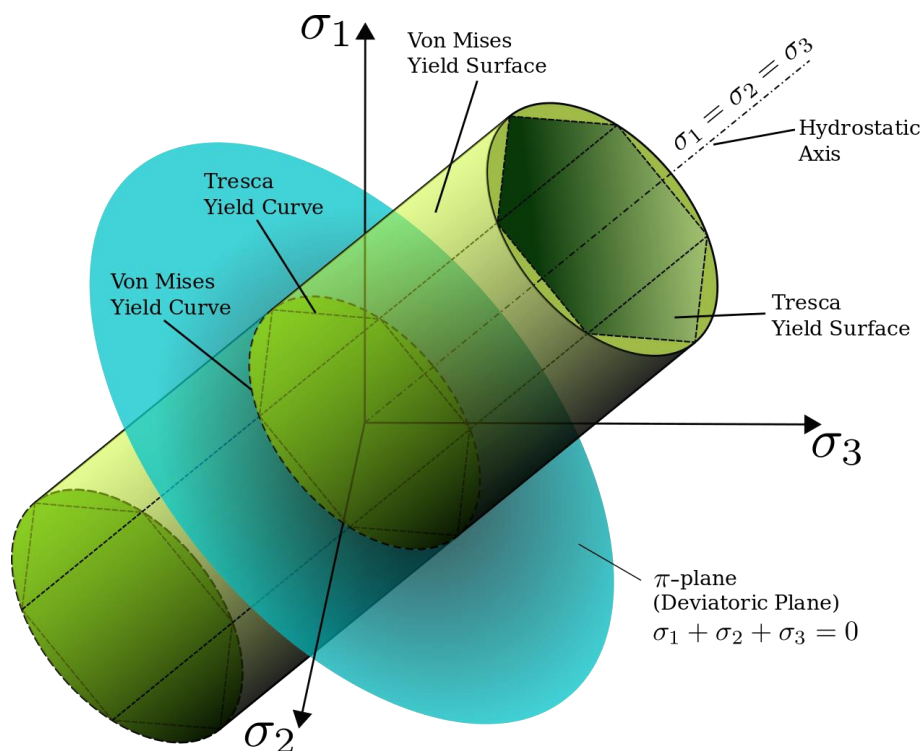
Figure 2.3. Visual representation of yielding criteria in the principal stress space [13]

2.2.2.3.   Thermal strain [14], [15]

If a solid body is subjected to a temperature change, the body will (almost) always expand because of thermal expansion. If the body is unconstrained no stresses will be caused by the temperature change and once the temperature is returned to its initial value the body will take its initial shape and size.

If the solid body is constrained, meaning that it's not allowed to expand in all or some directions, constraint reaction forces due to temperature change will induce stresses and strains into the body.

Another way to induce stresses into a solid body, even if it's unconstrained, is to heat or cool different parts of the body so fast in order to generate noticeable temperature gradients inside the body, i.e. time dependent non-uniform temperature field. This can be imagined as a body constraining its own hotter parts, which expanded more, with the cooler parts which expanded less (or even shrank) generating stresses within itself. This is more likely to happen in large solid bodies exposed to sudden and large temperature changes.

In linear thermoelasticity, thermal strain can be written as

$$\varepsilon_{ij}^{\text{therm}} = \alpha_{\text{T}} \Delta T \, , \tag{2.25}$$

where α_{T} is thermal expansion coefficient and ΔT is temperature difference.

By including thermal strain into constitutive equation (2.13) we get

$$d\sigma_{ij} = D_{ijkl} \left(d\varepsilon_{kl} - d\varepsilon_{kl}^{\text{p}} - d\varepsilon_{kl}^{\text{therm}} \right). \tag{2.26}$$

2.2.3. Strain Hardening

For non-hardening material yield curve preserves its shape and size during the deformation process. On the other hand, for a strain-hardening material, size and shape of the yield locus depend on the total history of deformation.

Two approaches used to simplify and describe strain hardening are:

- isotropic hardening,
- kinematic hardening.

Isotropic hardening theory is based on these assumptions: the material is isotropic and the Bauschinger effect is neglected. Later on, it is assumed that the yield surface expands without the change of shape.

Kinematic hardening theory takes the Bauschinger effect into account and considers the material as a non-isotropic continuum. The yield surface is assumed to undergo translation in the stress space. In reality, the hardening process involves simultaneous translation and expansion (contraction) of the yield surface, combining both described approaches.

Both approaches are shown graphically in Figure 2.4.
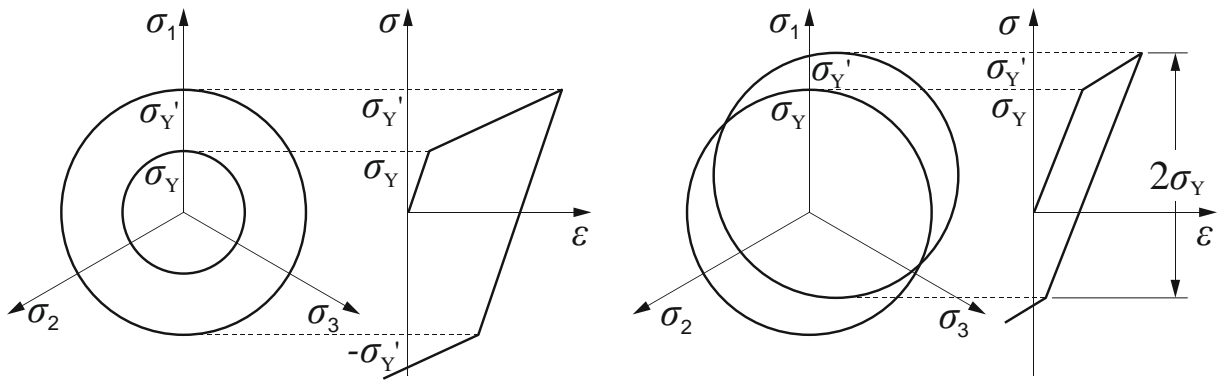
Figure 2.4. Graphical representation of isotropic (left) and kinematic (right) hardening

For isotropic hardening material model, von Mises yielding criterion can be expressed as a function of second invariant of stress deviator tensor J_2 as follows

$$f\left(\sigma_{ij},\varepsilon_{ij}^{\mathrm{p}}\right)=J_2-\frac{1}{3}\sigma_{\mathrm{Y}}^2=0,\tag{2.27}$$

where σ_{Y} is uniaxial yield strength in case of linear isotropic hardening material.

Yield strength σ_{Y} is linearly changing as is written in Equation (2.28),

$$\sigma_{\mathrm{Y}}=\sigma_{\mathrm{Y}_0}+K\varepsilon_{\mathrm{ekv}}^{\mathrm{p}},\tag{2.28}$$

where σ_{Y_0} is initial yield strength, $\varepsilon_{\mathrm{ekv}}^{\mathrm{p}}$ is equivalent plastic strain and parameter K is the hardening modulus describing the incline of the hardening curve shown in Figure 2.5.
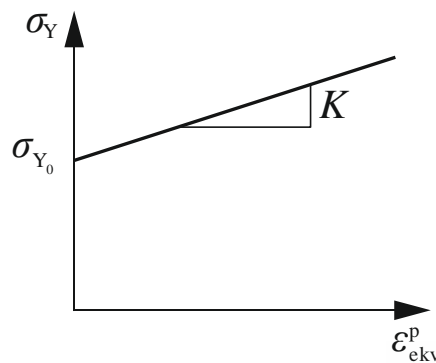
Figure 2.5. Linear isotropic hardening

Figure 2.6. shows stress-strain curve for elastic - linear isotropic hardening material.
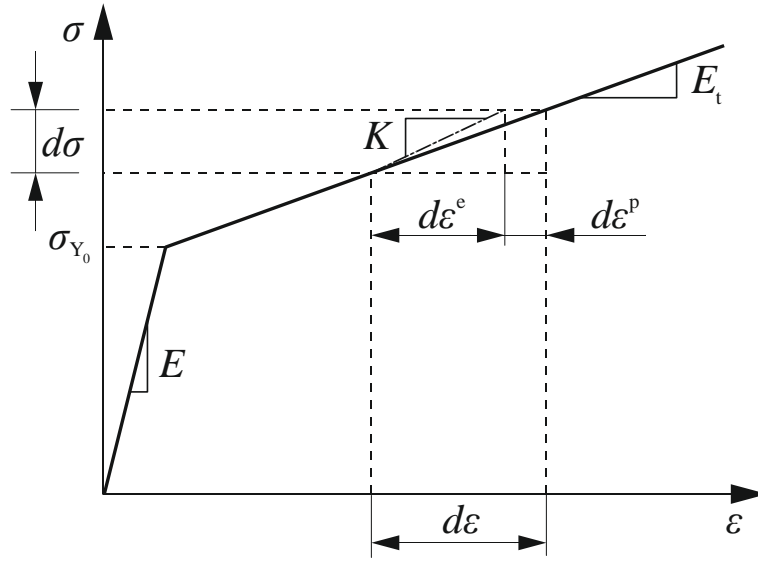
Figure 2.6. Stress-strain curve for elastic – linear isotropic hardening material

In Figure 2.6., E is Young's modulus, E_t is tangent modulus and K is hardening modulus. The connection between those three parameters is given as

$$K = \frac{E_t E}{E - E_t} \,.$$

(2.29)

Plastic strain increment depicted in Figure 2.6. can be expressed with non-associated flow rule as

$$d\varepsilon_{ij}^{p} = d\lambda \frac{\partial g}{\partial \sigma_{ij}} \,,$$

(2.30)

where $g = g\left(\sigma_{ij}, \varepsilon_{ij}^{p}, \kappa\right)$ is plastic potential and $d\lambda$ is plastic multiplier.

If plastic potential is equal to the yield function $f = f\left(\sigma_{ij}, \varepsilon_{ij}^{p}, \kappa\right)$ then we get associated flow rule

$$d\varepsilon_{ij}^{p} = d\lambda \frac{\partial f}{\partial \sigma_{ij}} \,.$$

(2.31)

If stress is expressed as a function of total strain in plasticity area, then constitutive equation can be written in the following form

$$d\sigma_{ij} = D_{ijkl}^{\mathrm{ep}}\, d\varepsilon_{kl}\,, \tag{2.32}$$

where is elasto-plastic stiffness tensor.

Elasto-plastic material stiffness tensor is the sum of elastic stiffness tensor and plastic material stiffness tensor .

2.3. Fatigue [16], [17], [18], [19]

Fatigue is defined as a process of the cycle-by-cycle accumulation of damage in a material undergoing fluctuating stresses and strains which may result in crack initiation or even a complete structure failure after a sufficient number of fluctuations. A significant feature of fatigue is that the load is not large enough to cause immediate failure. For crack initiation analysis, high cycle fatigue (HCF) and low cycle fatigue (LCF) are treated separately:

- HCF – low amplitude high frequency elastic strains, failure may occur after $N_{\mathrm{f}} > 10^{5}$ cycles,
- LCF – high amplitude low frequency plastic strains, failure occurs after $N_{\mathrm{f}} = 10^{2} - 10^{5}$ cycles.
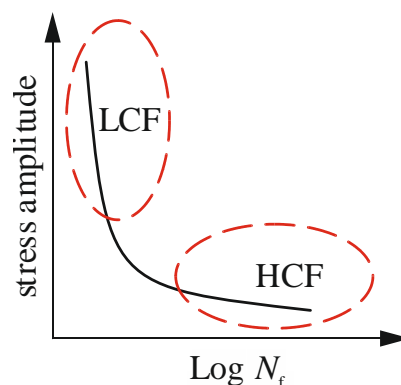
Figure 2.7. HCF and LCF comparison

HCF will not be further discussed since it is not included in the scope of this thesis.

2.3.1. Cyclic Stress-Strain Material Behaviour

Stress-strain responses for monotonic and cyclic loading differ. This was first observed by Bauschinger. His experiments indicated that the yield strength in tension or compression was reduced after applying a load of the opposite sign that caused plastic deformation.

This means that material can exhibit cyclic strain hardening or softening while under cyclic loading what can be observed as a change of the characteristic stress-strain relation.

Effect of cyclic strain hardening for uniaxial, symmetrical, strain controlled, stress-strain test is shown in Figure 2.8.
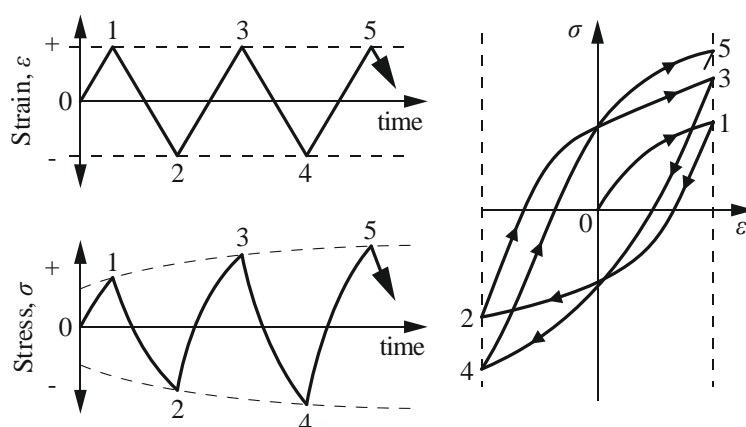
Figure 2.8. Cyclic strain hardening

Cyclic strain hardening indicates increased resistance to deformation.

Effect of cyclic strain softening for uniaxial, symmetrical, strain controlled, stress-strain test is shown in Figure 2.9.
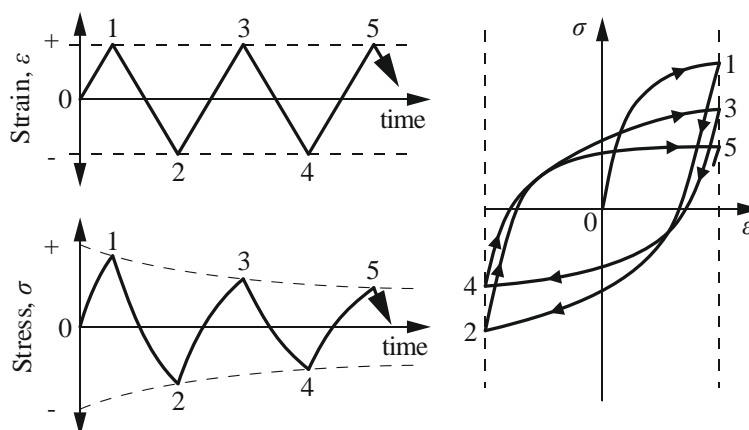
Figure 2.9. Cyclic strain softening

Cyclic strain softening indicates decreased resistance to deformation.

After a specific number of cycles, stress strain hysteresis loops become stabilised which means that process of cyclic strain hardening/softening process is also stabilised.

A curve drawn through the tips of stabilised stress-strain hysteresis loops defines cyclic stress-strain curve, as shown in Figure 2.10.
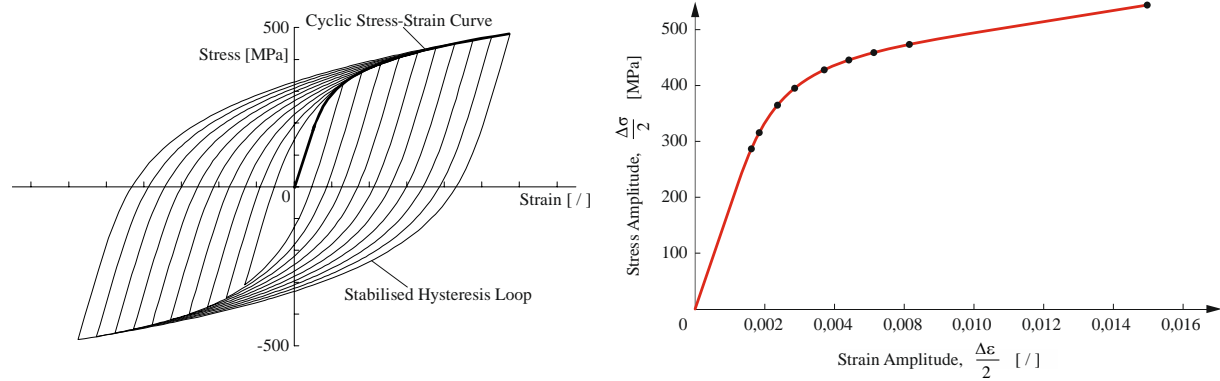
Figure 2.10. Stabilised hysteresis loops and cyclic stress-strain curve

Nonlinear stress-strain relationship for cyclic stress-strain curve can be represented by Ramberg-Osgood equation

$$\frac{\Delta \varepsilon}{2} = \frac{\Delta \sigma}{2E^*} + \left(\frac{\Delta \sigma}{2K'} \right)^{\left(\frac{1}{n'} \right)},$$ (2.33)

where $\dfrac{\Delta \varepsilon}{2}$ is total strain amplitude,

E^* is cyclic modulus of elasticity (with $E^* \approx E$) ,

K' is cyclic strength coefficient and

n' is cyclic strain hardening exponent.

Material parameters E^* , K' and n' are determined experimentally.

2.3.2. Low Cycle Fatigue

Total number of cycles before failure N_f for LCF approach can be written as

$$N_\text{f} = N_\text{i} + N_\text{p}, \tag{2.34}$$

where N_i is number of cycles before crack initiation and N_p is number of cycles required for the crack to propagate to its critical size.

Since crack initiation time is usually much longer than the time required for a crack to propagate to its critical size $\left(N_\text{i} \gg N_\text{p} \right)$, the following approximation can be written:

$$N_\text{f} \approx N_\text{i}. \tag{2.35}$$

2.3.2.1.   Strain Life Approach

Strain life $\left(\varepsilon - N \right)$ method is usually used to describe LCF. Strain life method is based on the premise that material behaviour in critical locations is strain dependent. Another key feature of strain life method is that plastic strains are accounted for, whereas in stress life method suitable for HCF analysis this is not the case.

The strain life equation, also known as Coffin-Manson relation, for uniaxial stress state can be written as

$$\frac{\Delta \varepsilon}{2} = \frac{\Delta \varepsilon^\text{e}}{2} + \frac{\Delta \varepsilon^\text{p}}{2} = \frac{\sigma_\text{f}'}{E} \left(2N_\text{f} \right)^b + \varepsilon_\text{f}' \left(2N_\text{f} \right)^c, \tag{2.36}$$

Where $\dfrac{\Delta \varepsilon}{2}$ is total applied strain amplitude,

$\dfrac{\Delta \varepsilon^\text{e}}{2}$ is elastic strain amplitude,

$\dfrac{\Delta \varepsilon^\text{p}}{2}$ is plastic strain amplitude,

$2N_\text{f}$ is the endurance in reversals,

σ'_{f} is fatigue strength coefficient,

b is fatigue strength exponent (Basquin's exponent),

$\varepsilon'_{\mathrm{f}}$ is fatigue ductility coefficient and

c is fatigue ductility exponent (Coffin-Manson exponent).

Material parameters σ'_{f}, b, $\varepsilon'_{\mathrm{f}}$ and c are determined experimentally.

For more complex, multiaxial loads, one of the developed multiaxial fatigue criteria, such as the critical plane method, has to be applied.

The low cycle fatigue is usually graphically presented as the strain $\Delta\varepsilon$ in log scale against cycles to failure N_{f} also in log scale as shown in Figure 2.11.
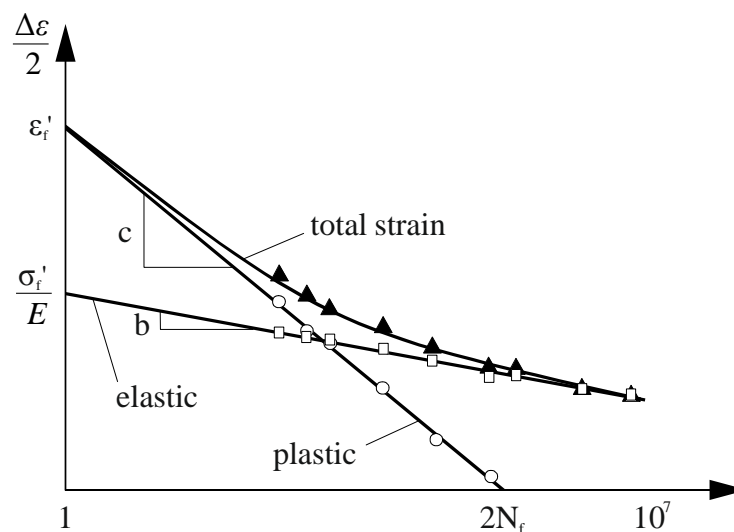
Figure 2.11. Low cycle fatigue relationship between total strain and endurance

2.3.2.2. Strain Energy Density Approach [20]

This approach to predicting fatigue life is based on the premise that the energy required to cause fracture is gradually accumulated during the course of the cyclic loading and it is observable in terms of strain hysteresis. Plastic strain energy per cycle Δw is predominant cause of energy dissipation in metals and it is nearly constant during cyclic loading under strain-controlled conditions. Plastic strain energy per cycle can be represented as the area of the stabilised hysteresis loop as shown in Figure 2.12.

Variation of maximal stress with number of cycle for the LCF test
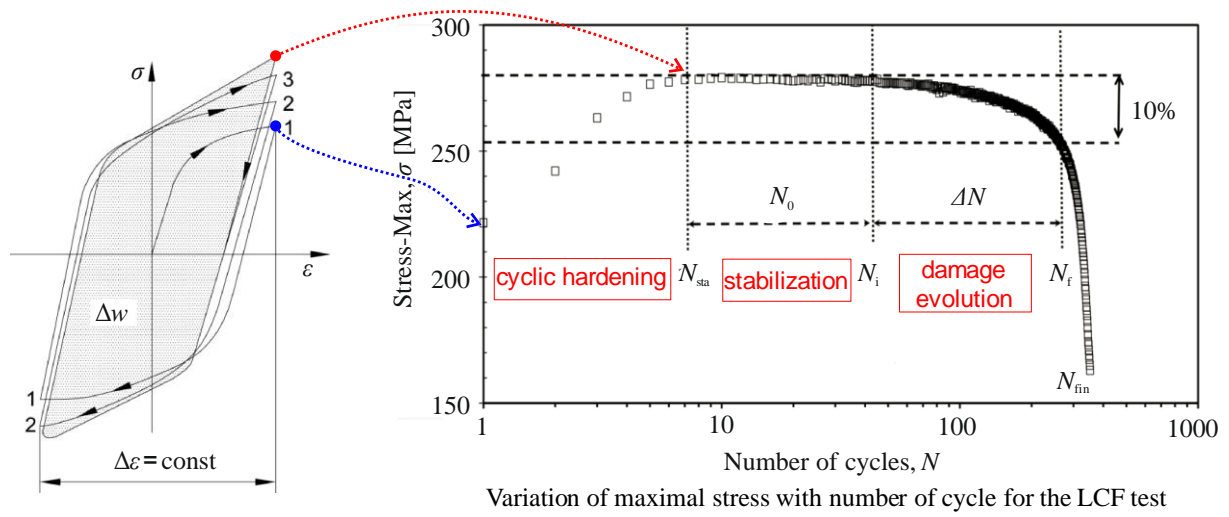
Figure 2.12. Damage initiation and evolution [20]

Plastic strain energy per cycle Δw can be calculated as [21]

$$\Delta w = \frac{1-n'}{1+n'} \Delta\sigma\Delta\varepsilon^{\mathrm{p}} . \tag{2.37}$$

Number of cycles for damage to initiate N_0 can be calculated as

$$N_0 = c_1 \Delta w_{\mathrm{sta}}^{\ c_2} , \tag{2.38}$$

where c_1, c_2 are material parameters and

Δw_{sta} is accumulated plastic strain energy for the stabilized state.

Number of cycles for damage to initiate N_0 can be also expressed as

$$N_0 = N_{\mathrm{i}} - N_{\mathrm{sta}} , \tag{2.39}$$

where N_{sta} is number of cycles at which the material is stabilised.

N_{i} is determined as the number of cycles at which Δw_{sta} drops by 0.5% from its peak value.

Typically, energy based criteria are very suitable to be used as damage parameter for TMF analysis of exhaust manifolds or cylinder heads [1].

Silicon molybdenum spheroidal graphite cast iron, tested in [22], showed that typically less than 20 cycles were necessary for material to stabilise. For comparison, stabilised phase lasted for several hundred cycles.

According to AVL's TMF method, fatigue limit of exhaust manifold is reached when damage is initiated. This means that damage evaluation process is not analysed and for that reason it will not be further discussed in the scope of this thesis.

2.3.3. Other Fatigue Life Factors

Other than being directly determined by material properties of a component and influenced by cyclic hardening/softening effect, fatigue life is also highly affected by

- load history (type, frequency, mean stress effect),
- stress concentrators (geometrical, manufacturing, damage in service),
- component size,
- surface conditions and
- environmental effects (temperature, humidity, corrosivity).

In order to keep this thesis as concise as possible, only the effect of temperature on fatigue life will be discussed in more detail.

2.3.4. Temperature Effects on Fatigue Life

Temperature effects on fatigue life vary significantly with material type. There is no single rule which is applicable to all materials. To determine the temperature effects on fatigue life, experiments have to be carried out for each material type independently. To demonstrate this, few generalised statements are given in the next paragraph.

In general, material stiffness is decreased with increase in temperature, especially if temperature exceeds approximately half of the melting point temperature T_m. Such high temperatures can lead to creep failure. On the other hand, material stiffness is increased with decrease in

temperature. For that reason ductile materials become more brittle when cooled and the cracks in brittle materials propagate more rapidly than in ductile materials which decreases fatigue life.

One specific material type of interest for this thesis is Si-Mo ductile cast iron, widely used for exhaust manifolds of internal combustion engines.

Si-Mo ductile cast irons usually contain 4-6% Si and 0,5-2% Mo. High Si content both increases the high temperature corrosion resistance, by forming a Si-rich surface oxide layer, and stabilizes the ferritic matrix, primarily by increasing the A1 transformation temperature. Addition of Mo increases the high temperature strength and improves the creep behaviour by forming alloy carbides in the ferritic matrix. In the application the maximum temperature at points at full engine load may be higher than 750 °C. The main damage mechanisms in service are high-temperature oxidation and thermo-mechanical fatigue [23].

For temperatures above 500 °C, elastic modulus E, yield strength σ_Y and ultimate tensile strength σ_m reduced significantly [23].

Symmetrical cyclic test were carried out at different temperatures. From chart shown in Figure 2.13. it can be concluded that for low number of cycles (up to 10^5) there is no noticeable decrease in fatigue strength between room temperature (22 °C) and 400 °C, but for 700 °C the drop is significant.

It should be noted that data presented in Figure 2.13. are obtained for load ratio $R = -1$ and that non broken specimens are represented by empty symbols.
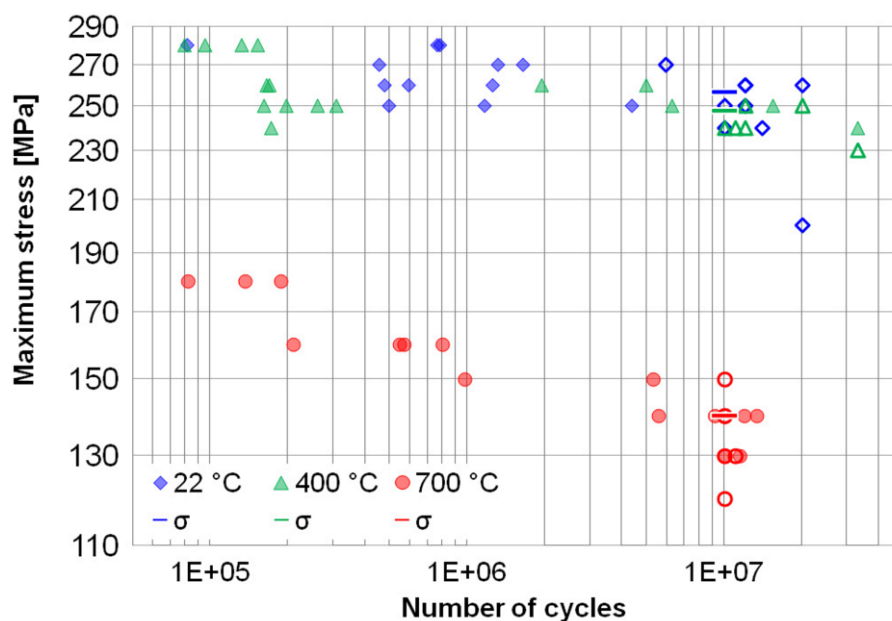
Figure 2.13. Fatigue stress-life tests for various temperatures [23]

2.4. Thermo-mechanical Fatigue [24]

Combined thermal and mechanical loads where both stresses and temperatures vary with time cause thermo-mechanical fatigue (TMF). This type of loading can be more damaging by more than an order of magnitude compared to isothermal fatigue at the maximum operating temperature. TMF is the primary life-limiting factor for engineering components in many high-temperature applications. Material properties, mechanical strain range, strain rate, temperature and the phasing between thermal and mechanical strain all play a significant role in the type of damage formed in the material.

Depending on the phase between thermal and mechanical strain, TMF loading can be described to be in-phase (IP) or out-of-phase (OP). In case of IP loading, the maximum temperature and strain occur at the same time. In case of OP loading, the material experiences compression at highest temperature and tension at lower temperatures. OP loading is more likely to cause oxidation damage because an oxide film can form in compression at the higher temperature and then rupture during the subsequent low temperature tensile portion of the loading cycle where the oxide film is more brittle. Schematic illustration of the stress-strain response under these two loading types is given in Figure 2.14.
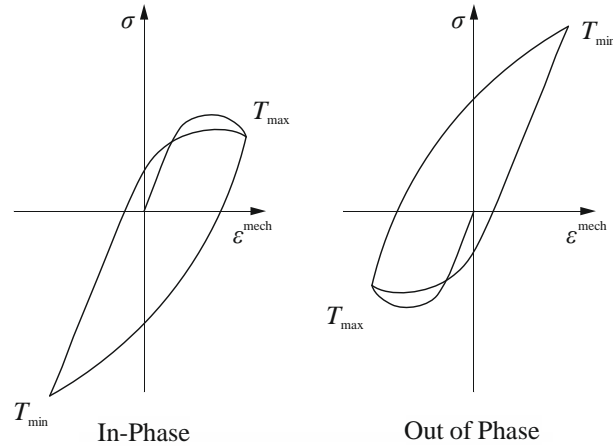
Figure 2.14. Load and temperature phasing

Many TMF lifetime prediction approaches have been developed over the years. Those approaches could be classified as strain based, energy based, damage parameters, fracture mechanics, cumulative and micro-structural approaches. Independent on the theory used, the life prediction is based on functions of the induced strains and stresses due to thermo-mechanical loading and the material parameters [25].

Although there are many active mechanisms in the TMF process, the damage can be considered from three primary sources: fatigue, oxidation and creep.

Damage from each process can be summed to obtain an estimate of the total fatigue life N_f as

$$\frac{1}{N_f} = \frac{1}{N_f^{\text{fatigue}}} + \frac{1}{N_f^{\text{oxidation}}} + \frac{1}{N_f^{\text{creep}}} \, , \tag{2.40}$$

or

$$D_f = D_f^{\text{fatigue}} + D_f^{\text{oxidation}} + D_f^{\text{creep}} \, , \tag{2.41}$$

where upper indices "fatigue", "oxidation" and "creep" stand for fatigue damage, oxidation damage and creep damage respectively.

Usually, one of the damage mechanisms is dominant. From an engineering modelling perspective, this suggests that the individual damage models and their associated material properties should be accurate only for those conditions where the failure mechanism in question is dominant.

2.4.1. Damage Mechanisms

2.4.1.1.   Fatigue Mechanisms

"Fatigue damage in the life regime of interest in TMF is in the form of nucleation and growth of microcracks. The process is driven by cyclic plastic strains where oxidation and creep effects are negligible. Fatigue damage will dominate at high strain ranges, strain rates and low temperatures" [24].

2.4.1.2.   Oxidation Mechanisms

"Oxidation damage can occur in the form of an oxide intrusion. In OP loading, an oxide layer can form on the surface when the material is hot and in compression. At the lower temperature the oxide layer becomes brittle. During mechanical straining it then cracks to expose new clean metal surfaces. This clean metal will rapidly oxidize and the process repeats during the next mechanical strain cycle. Ultimately, this will form a crack which can then grow during the mechanical strain cycle. Oxide cracks can also form during IP loading. In this case, the oxide forms during the hot portion of the loading cycle while the material is in tension. Then upon cooling the oxide film undergoes a buckling delamination which fractures the oxide and exposes clean metal surfaces. Oxide formation and rupture during isothermal loading is not the dominant failure mechanism and is not reflected in isothermal test or materials data. Oxide formation will occur easier and faster at higher temperatures. The tendency of the oxide to develop microcracks will depend on the cyclic strain range; stress does not play a role in the development of oxide induced microcracks" [24].

2.4.1.3.   Creep Mechanisms

"Creep is essentially a diffusion process. At high stresses diffusion allows dislocations to climb over barriers. At lower stresses diffusion occurs along the grain boundaries. These microcracks form as a result of grain boundary sliding to accommodate the change in shape of elongated grains. Diffusion is highly temperature and time dependent. Maximum stress rather than strain range has a dominant role in the formation of these microcracks. The interaction of the strain rate and temperature has a strong influence of the stresses that are observed during cyclic loading" [24].

3. Numerical Modelling of TMF Problems

Finite element method (FE method, FEM) is a numerical method based on discretization of a continuum into a finite number of smaller parts called finite elements. In reality, continuum possesses an infinite number of degrees of freedom. By discretizing it, a finite number of degrees of freedom is necessary to approximately describe its behaviour. The reason why the solution is approximate lies in the fact that by discretizing differential equations, which exactly describe the behaviour of a continuum, they transform into algebraic equations. Deep knowledge of FEM principles and physics of a problem at hand is necessary to define the numerical model correctly in order to simulate the behaviour of a real system as best as possible. FEM is quite versatile and can be used to solve many different problems. Some of the applications for FEM are: strength analysis, dynamic analysis, heat transfer analysis, electrical analysis, stead-state transfer analysis, acoustic analysis and mass diffusion analysis. In order to overcome the drawbacks of highly specialized tools and software and to describe mutual dependencies between various engineering problems which interact in reality, coupled analyses are carried out. In other words, when the input of one physics analysis depends on the results from another analysis, the analyses are coupled.

Different types of analyses will be carried out in the scope of this thesis, namely steady state HT analysis, transient HT analysis, strength analysis and thermo-mechanical fatigue analysis.

3.1. Numerical Heat Transfer Analysis [4]

Objective of a HT analysis is to obtain temperature field for the given geometry, initial temperature field and boundary conditions.

Classical variational principles cannot be used to solve transient HT problems so the Galerkin method of weighted residual is used. The basic idea is not to make the residual disappear in each point because this would be impossible to achieve, but rather to make the residual disappear in every nodal point of a mesh what can be achieved by equating the integral of the product of residual R and weight function w to zero.

This can be written as

$$\int_V R(x)w(x)\mathrm{d}V = 0.$$ (3.1)

A function in a form of $N_i(x)$ is used as a weight function $w_i(x)$ in Galerkin method what can be written as

$$\int_V R(x)N_i(x)\mathrm{d}V = 0.$$ (3.2)

Approximation of temperature field over a finite element can be written as

$$\overline{T} = \mathbf{NT},$$ (3.3)

where $\mathbf{N}$ is shape function matrix and $\mathbf{T}$ is nodal temperature matrix.

By introducing the above approximation into the Equation (2.3), a non-zero residual is created as

$$R(x) = -\rho c \frac{\partial T}{\partial t} + \frac{\partial}{\partial x}\left(\lambda_x \frac{\partial T}{\partial x}\right) + \frac{\partial}{\partial y}\left(\lambda_y \frac{\partial T}{\partial y}\right) + \frac{\partial}{\partial z}\left(\lambda_z \frac{\partial T}{\partial z}\right).$$ (3.4)

Equations (3.4) and (3.2) form residual equations. From residual equations, finite element transient HT equation for a single element can be derived as

$$\mathbf{c}\dot{\mathbf{T}}(t) + \mathbf{k}_{\mathrm{T}}\mathbf{T}(t) = \mathbf{f}_{\mathrm{g}}(t),$$ (3.5)

where $\mathbf{c}$ is consistent heat capacity matrix, $\mathbf{k}_{\mathrm{T}}$ is heat conductance matrix and $\mathbf{f}_{\mathrm{g}}$ is Neumann boundary condition vector.

Following equations show how matrices in Equation (3.5) are calculated:

$$\mathbf{c} = \int_V \rho c \mathbf{N}^{\mathrm{T}} \mathbf{N} dV,$$

$$\mathbf{k}_{\mathrm{T}} = \int_V \mathbf{B}^{\mathrm{T}} \mathbf{K} \mathbf{B} dV, \tag{3.6}$$

$$\mathbf{f}_{\mathrm{g}} = \int_A \mathbf{q}_S \mathbf{N} dS,$$

where $\mathbf{B}$ is strain-displacement matrix used to interpolate element strains using nodal displacements.

Global finite element equation for transient HT without heat source can be written as

$$\mathbf{C}\dot{\mathbf{T}}(t) + \mathbf{K}_{\mathrm{T}}\mathbf{T}(t) = \mathbf{F}_{\mathrm{g}}(t), \tag{3.7}$$

where $\mathbf{C}$ is global consistent heat capacity matrix, $\mathbf{K}_{\mathrm{T}}$ is global heat conductance matrix and $\mathbf{F}_{\mathrm{g}}$ is global Neumann boundary condition vector.

3.2. Time Integration Methods [4], [26]

Since FEM can be used to solve unsteady (time dependent, transient) problems, in order to solve such problems additional time integration methods have to be defined. Methods used for solving time-domain systems of differential equations usually involve finite difference methods. Finite difference methods (FDM) are numerical methods for solving differential equations by approximating them with difference equations, in which finite differences approximate the derivatives. Time is also discretized in this context and solutions are calculated only in discrete time points, spaced by finite time intervals Δt.

There are three distinct types of finite difference method:
   1. explicit method,
   2. implicit method,
   3. implicit Crank-Nicolson method.

Those three types can be explained on an example of transient HT problem represented by the Equation (2.4), where term $\dfrac{\partial T}{\partial t}$ can be approximated by a finite difference.

3.2.1. Explicit Method

Explicit method using forward difference at time t gives

$$\frac{\partial T}{\partial t}(t) \approx \frac{T(t+\Delta t)-T(t)}{\Delta t}.$$
(3.8)

This means that by knowing the values at time t, we can obtain the corresponding values at time $t + \Delta t$. This method is conditionally stable meaning that time step always has to remain small enough which can be a limiting factor for long simulation times. The errors are linear over the time step and quadratic over the space step. The analysis cost rises only linearly with problem size. Therefore, explicit method is suitable for very large, extremely discontinuous short-term events, e.g. crash or drop test simulation.

3.2.2. Implicit Method

Implicit method using backward difference at time $t + \Delta t$ gives

$$\frac{\partial T}{\partial t}(t+\Delta t) \approx \frac{T(t+\Delta t)-T(t)}{\Delta t}.$$
(3.9)

Implicit methods find a solution by solving an equation involving both the current state of the system at time t and the later one at time $t + \Delta t$. This means that implicit method requires some extra computation (iteration) in each time step. This method is unconditionally stable. The errors are linear over the time step and quadratic over the space step.

Abaqus/Standard solver, a part of SIMULIA Abaqus® software, solves the non-linear system of equations in each time step iteratively using Newton's method. Those iteration steps resemble a time-like process but they usually do not correspond to a realistic time-dependent behaviour. It is this aspect of an implicit method that makes it attractive for steady-state computations, because the number of iterations required for a solution is often much smaller than the number of time steps needed for an accurate transient that asymptotically approaches steady conditions.

Iterative procedure can have quadratic convergence if analysis doesn't involve contacts. If analysis involves contacts, convergence of iterative process might be poor or sometimes it cannot be even achieved. Abaqus/Standard uses automatic time incrementation method. The time step is adjusted depending on the behaviour of the Newton iteration and the accuracy of the time integration.

3.2.3. Implicit Crank-Nicolson Method

Implicit Crank-Nicolson method using central difference at time $t + \dfrac{\Delta t}{2}$ gives

$$\frac{\partial T}{\partial t}\left(t + \frac{\Delta t}{2}\right) \approx \frac{T\left(t + \Delta t\right) - T\left(t\right)}{\Delta t} . \tag{3.10}$$

Solution is approximated at the middle of a time step with averaged values of all variables (arithmetic mean). This method is unconditionally stable. The errors are quadratic over both the time step and the space step.

3.3. Numerical Strength Analysis [8], [11], [27], [28]

Analyses of strength problems can be linear or nonlinear, same as HT problem analyses.

Linear strength analyses are carried out with the following assumptions:
- only small displacements occur, force balance is analysed in undeformed state and load direction does not change (conservative load),
- material model is linear elastic,
- non-homogeneities and anisotropy are not load dependent,
- there is a linear dependence between stress and strain.

If only one of the above conditions is not met, nonlinear problem should be analysed. There are several sources of nonlinearity:
- geometric nonlinearity (large displacements, large strain, buckling – snap-through or bifurcation, non-conservative load),
- material nonlinearities (plasticity, creep, viscoelasticity, viscoplasticity),
- nonlinear boundary conditions (contacts).

Single problem can include multiple sources of nonlinearity. Displacements are no longer directly proportional to loading like they are in a case of linear problems. This also means that superposition principle can no longer be applied.

Global finite element equation for nonlinear problems now looks like

$$\mathbf{K}\left(\mathbf{V},\mathbf{R}\right)\mathbf{V}=\mathbf{R}\,,\qquad\qquad(3.11)$$

where $\mathbf{K}$ is global stiffness matrix, $\mathbf{V}$ global nodal displacement vector and $\mathbf{R}$ is global nodal force vector.

Equation (3.11) clearly shows that global stiffness matrix depends on current displacement and load. Due to this nonlinear response, it is not possible to solve the problem in a single step. Solving process is now based on incremental-iterative methods. Those methods work by linearizing the Equation (3.11). From the initial (reference) state new neighbouring equilibrium state is determined by an increment of the load or displacement. An equilibrium is iteratively achieved for the new state by various iterative methods.

Linearized Equation (3.11) takes form

$$\mathbf{K}_{t}\left(\overline{\mathbf{V}}\right)\Delta\mathbf{V}=\mathbf{R}^{\text{ext}}-\mathbf{R}^{\text{int}}\left(\overline{\mathbf{V}}\right),\qquad\qquad(3.12)$$

where $\mathbf{K}_{t}$ is tangent stiffness matrix, $\overline{\mathbf{V}}$ is initial (reference) displacement vector, $\Delta\mathbf{V}$ is incremental displacement vector, $\mathbf{R}^{\text{ext}}$ is external force vector and $\mathbf{R}^{\text{int}}$ is internal force vector.

Equilibrium is achieved when the right side of the Equation (3.12) becomes zero, meaning that external and internal forces are equal, or in the case that incremental displacement vector $\Delta\mathbf{V}$ is zero vector.

Nonlinear relation between load and displacement is shown in the Figure 3.1.
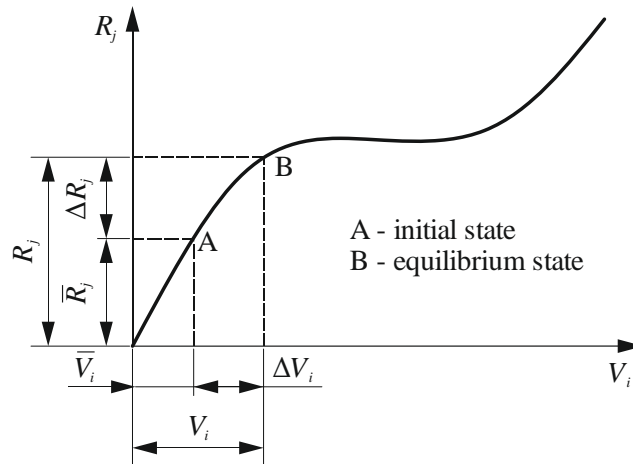
Figure 3.1. Nonlinear relationship between load and displacement

Nonlinear FEM strength analysis algorithm is shown in Figure 3.2.
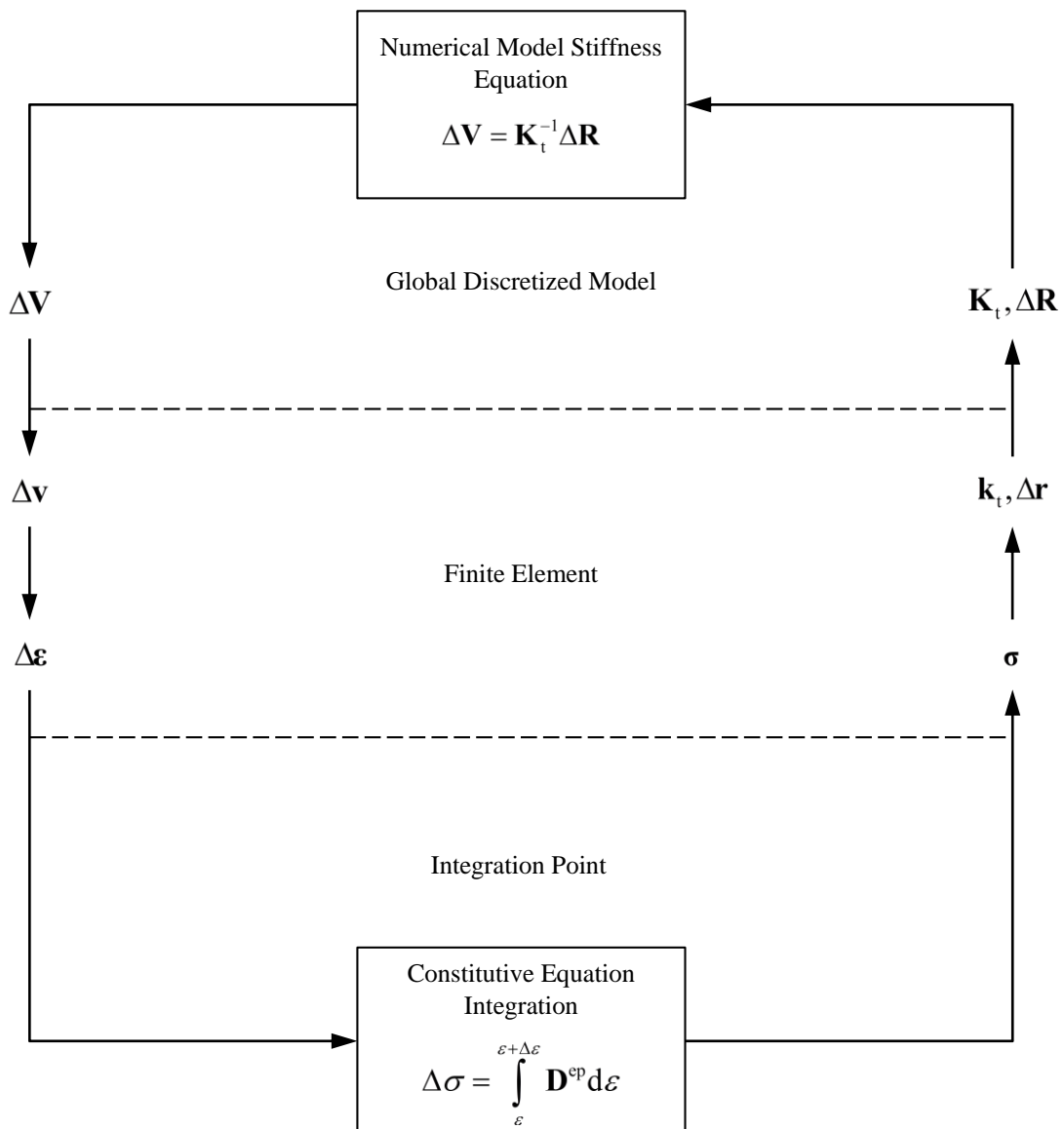
Figure 3.2. Nonlinear FEM strength analysis algorithm

Analysis starts by solving the Equation (3.12) and from there global displacement increments can be extracted. In the next step those displacements are transformed into local coordinate systems of finite elements from which strain increments are calculated.

In every integration point of nonlinear numerical model constitutive Equation (2.32) is integrated in order to obtain the stress increment as follows

$$\Delta\sigma = \int\limits_{\varepsilon}^{\varepsilon+\mathrm{d}\varepsilon} \mathbf{D}^{\mathrm{ep}}\mathrm{d}\varepsilon \ . \tag{3.13}$$

Constitutive equation integration is carried out by backward Euler method which is based on return mapping algorithm. First step of return mapping algorithm is solving the elastic equations to obtain the elastic predictor. If this σ^{trial} (plastic predictor) falls outside the yield surface, meaning that it isn't elastic, assumption of elasticity has been wrong and the updated stress is obtained by the projection of σ^{trial} back onto the updated yield surface (plastic corrector). Return mapping of the trial stress back to the yield surface is iterative process. Once the iterative process is completed, stress increment can be calculated and used to update elasto-plastic stiffness tensor $\mathbf{D}^{\mathrm{ep}}$. With that, Equation (3.12) can now also be updated.

Tangent stiffness matrix for elastic, geometrically nonlinear analysis can be written as

$$\mathbf{k}_{\mathrm{t}} = \underbrace{\mathbf{k}_{\mathrm{e}} + \mathbf{k}_{\mathrm{uL}} + \mathbf{k}_{\mathrm{uN}}}_{\mathbf{k}_{\mathrm{eu}}} + \underbrace{\mathbf{k}_{\sigma\mathrm{L}} + \mathbf{k}_{\sigma\mathrm{N}}}_{\mathbf{k}_{\sigma}} \ , \tag{3.14}$$

where

$$\mathbf{k}_{\mathrm{e}} = \int\limits_{V} \mathbf{B}_{\mathrm{L}}^{\mathrm{T}}\mathbf{D}\mathbf{B}_{\mathrm{L}}\mathrm{d}V \ \text{ is elastic stiffness matrix}, \tag{3.15}$$

$$\mathbf{k}_{\mathrm{uL}} = \int\limits_{V} \left(\mathbf{B}_{\mathrm{L}}^{\mathrm{T}}\mathbf{D}\mathbf{B}_{\mathrm{N}}\left(\overline{\mathbf{v}}\right)+\mathbf{B}_{\mathrm{N}}^{\mathrm{T}}\left(\overline{\mathbf{v}}\right)\mathbf{D}\mathbf{B}_{\mathrm{L}}\right)\mathrm{d}V \ \text{ is linear initial displacement matrix}, \tag{3.16}$$

$$\mathbf{k}_{\mathrm{uN}} = \int\limits_{V} \mathbf{B}_{\mathrm{N}}^{\mathrm{T}}\left(\overline{\mathbf{v}}\right)\mathbf{D}\mathbf{B}_{\mathrm{N}}\left(\overline{\mathbf{v}}\right)\mathrm{d}V \ \text{ is nonlinear initial displacement matrix}, \tag{3.17}$$

$\mathbf{k}_{\sigma\mathrm{L}}$ is linear initial stress matrix,

$\mathbf{k}_{\sigma\mathrm{N}}$ is nonlinear initial stress matrix,

$\mathbf{k}_{\mathrm{eu}}$ is elastic stiffness matrix and

$\mathbf{k}_{\sigma}$ is initial stress matrix (geometric stiffness matrix).

In the equations above, $\mathbf{D}$ stands for elasticity matrix while $\mathbf{B}_L = \mathbf{D}_{kL}\mathbf{N}$ and $\mathbf{B}_N = \mathbf{D}_{kN}\mathbf{N}$ stand respectively for linear and nonlinear strain-displacement matrices where $\mathbf{D}_{kL}$ is linear kinematic differential operator and $\mathbf{D}_{kN}$ is nonlinear kinematic differential operator.

Initial stress matrix $\mathbf{k}_\sigma$ cannot be expressed in explicit form. Instead it can be expressed as

$$\mathbf{k}_\sigma \Delta\mathbf{v} = \int_V \mathbf{B}_N^T (\Delta\mathbf{v}) \mathbf{D} \left(\mathbf{B}_L + \frac{1}{2}\mathbf{B}_N (\overline{\mathbf{v}}) \right) dV\,\overline{\mathbf{v}}. \tag{3.18}$$

From Equation (3.18) linear and nonlinear initial stress matrices can be expressed as

$$\mathbf{k}_{\sigma L} \Delta\mathbf{v} = \int_V \mathbf{B}_N^T (\Delta\mathbf{v}) \mathbf{D}\mathbf{B}_L dV\,\overline{\mathbf{v}},$$

$$\mathbf{k}_{\sigma N} \Delta\mathbf{v} = \frac{1}{2}\int_V \mathbf{B}_N^T (\Delta\mathbf{v}) \mathbf{D}\mathbf{B}_N (\overline{\mathbf{v}}) dV\,\overline{\mathbf{v}}. \tag{3.19}$$

At finite element level, along with tangent stiffness matrix $\mathbf{k}_t$, both external forces $\mathbf{R}^{ext}$ and internal forces $\mathbf{R}^{int}$ are calculated as

$$\mathbf{R}^{ext} = \int_V \mathbf{N}^T (\overline{\mathbf{q}} + \Delta\mathbf{q}) dV + \int_{S_q} \mathbf{N}_S^T (\overline{\mathbf{q}}_b + \Delta\mathbf{q}_b) dS \tag{3.20}$$

and

$$\mathbf{R}^{int} = \int_V \left(\mathbf{B}_L + \mathbf{B}_N (\overline{\mathbf{v}}) \right)^T \mathbf{D} \left(\mathbf{B}_L + \frac{1}{2}\mathbf{B}_N (\overline{\mathbf{v}}) \right) dV\,\overline{\mathbf{v}}, \tag{3.21}$$

where $\mathbf{q}$ is volume load vector, $\mathbf{q}_b$ is surface load vector and $\mathbf{N}_S$ is edge shape function matrix.

If thermal strains $\boldsymbol{\varepsilon}^{therm}$ exist, temperature change can then be considered as a part of external forces. Therefore, Equation (3.20) can then be written as

$$\mathbf{R}^{ext} = \int_V \mathbf{N}^T (\overline{\mathbf{q}} + \Delta\mathbf{q}) dV + \int_{S_q} \mathbf{N}_S^T (\overline{\mathbf{q}}_b + \Delta\mathbf{q}_b) dS + \mathbf{R}^{therm}, \tag{3.22}$$

where $\mathbf{R}^{\text{therm}}$ is thermal load vector calculated as

$$\mathbf{R}^{\text{therm}} = \int_V \mathbf{B}^{\text{T}} \mathbf{D} \boldsymbol{\varepsilon}^{\text{therm}} \mathrm{d}V \,. \tag{3.23}$$

3.4.   Coupled Thermo-mechanical Analysis [9]

As said in the introduction part of Chapter 3, to consider dependencies between various interacting engineering problems, coupled analyses are carried out. TMF analysis is a coupled analysis which combines HT analysis with strength analysis. There are two distinct approaches to solving TMF problems based on degree of mutual dependency between stress/displacement solution and temperature field solution:

1.   Sequentially coupled thermo-mechanical analysis
2.   Fully coupled thermo-mechanical analysis

Sequentially coupled thermo-mechanical analysis can be conducted if the stress/displacement solution is dependent on a temperature field but there is no inverse dependency. Sequentially coupled thermo-mechanical analysis is performed by first solving the pure HT problem, followed by reading the temperature solution into a stress analysis as a predefined field. This kind of analysis was involved in the models used in this thesis.

In a fully coupled thermo-mechanical analysis coupled temperature-displacement procedure is used to solve simultaneously for the stress/displacement and the temperature fields. A coupled analysis is used when the thermal and mechanical solutions affect each other strongly. For example, in rapid metal forming problems where the inelastic deformation of the material causes significant increase in temperature.

3.5. Numerical Fatigue Analysis

Numerical fatigue analysis is the final step in numerical fatigue life prediction analysis. It relies on the results of thermal and strength analyses but basic principles presented in Chapter 2.3 still apply.

Numerical fatigue life analysis accuracy heavily depends on several factors:

1. accuracy of heat and stress analyses,
2. correct definition of a material model and
3. correct definition of a life prediction model.

Material models must correctly represent (*i*) the yield domain, since many areas in the component will remain elastic, (*ii*) cyclic loading (Bauschinger effect) and the viscous effect, (*iii*) aging effects, depending on the thermo-mechanical history. The material parameters are a priori temperature and aging dependent. To fully define such material models for a single material, a large number of extensive (expensive) tests has to be performed. For that reason, fully defined material models are rare and they exist only for small number of materials which have specific applications [29].

Life prediction model must take into account microstructural evolution, together with creep, fatigue, and creep-fatigue interaction. It is implemented in a post-processor which directly highlights the critical areas of the component, by integrating a damage variable on each Gauss point (integration point) or node of the mesh [29].

Schematic representation of a general algorithm for a numerical fatigue analysis is shown in Figure 3.3.
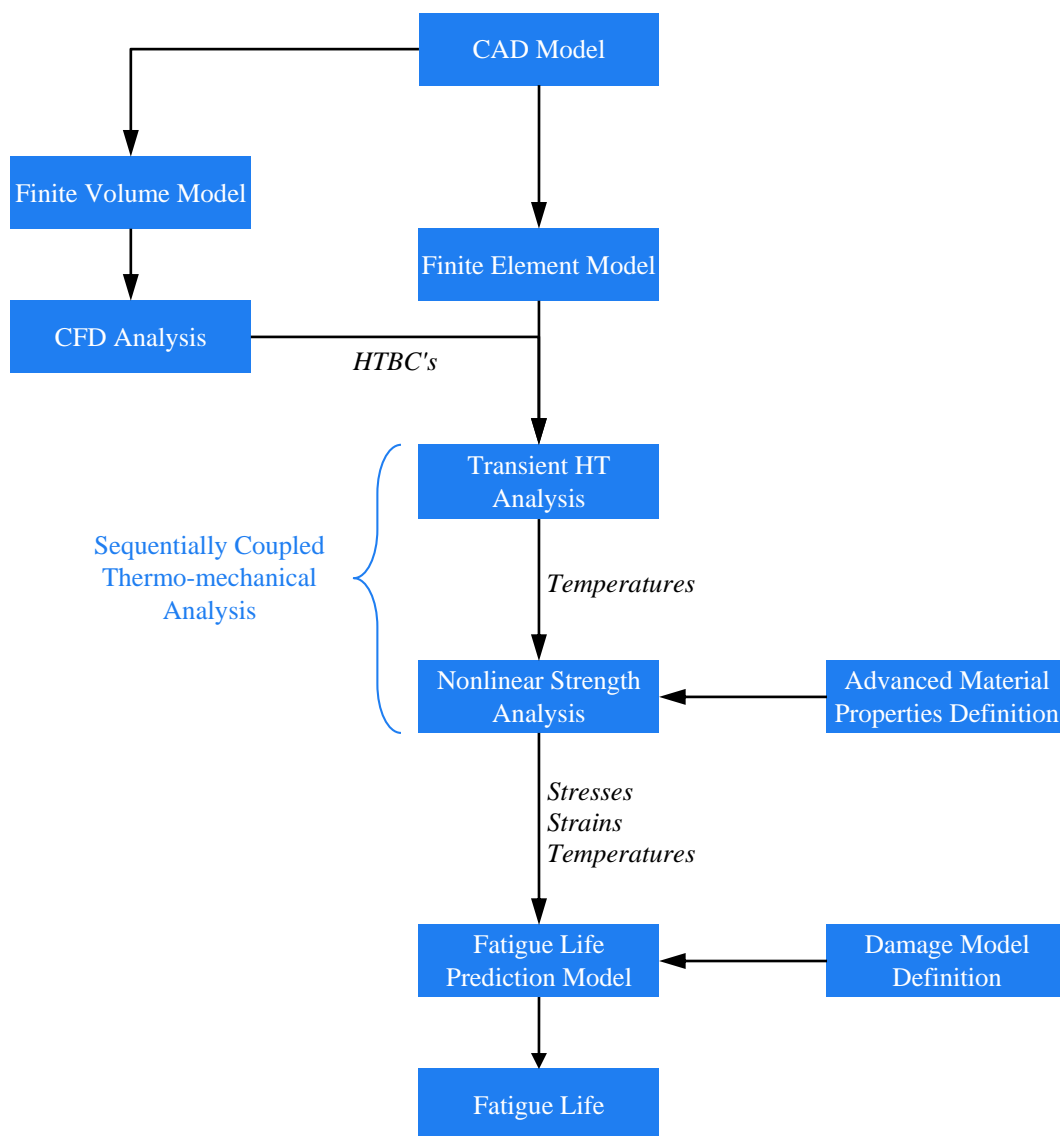
Figure 3.3. Schematic representation of a generic numerical fatigue analysis algorithm

3.5.1. AVL's TMF Lifetime Prediction Approach [30]

AVL has developed and improved its own methods for calculating fatigue life based on the years of experience gained as a result of numerous numerical calculations which were also validated and compared with experimental data. Current method (workflow) for calculating fatigue life is based on the results obtained from the last (stabilised) cycle of previously calculated sequentially coupled thermo-mechanical analysis.

Even though the exact damage model expression will not be given due to confidentiality reasons, some of the input parameters for fatigue analysis will be disclosed.

Equations (3.24), and (3.25) represent search algorithms used to calculate two input parameters for fatigue life prediction analysis.

These two parameters and their search algorithms are defined as follows:

Stress Range

$$\Delta S = \underset{t_0}{Max}\left(\underset{t}{Max}\left(\sigma^{\text{ekv}}\left(\mathbf{\sigma}(t) - \mathbf{\sigma}(t) \right) \right) \right), \tag{3.24}$$

Acumulated Viscoplastic Strain Range

$$\Delta \varepsilon^{\text{vp}} = \underset{t_0}{Max}\left(\underset{t}{Max}\left(\varepsilon^{\text{ekv}}\left(\mathbf{\varepsilon}^{\text{vp}}(t) - \mathbf{\varepsilon}^{\text{vp}}(t_0) \right) \right) \right), \tag{3.25}$$

Variables used to obtain parameters defined in equations (3.24) and (3.25) can be expressed as:

- von Mises equivalent stress $\qquad\qquad \sigma^{\text{ekv}}(\mathbf{\sigma}) = \left(3J_2 \right)^{1/2},$

- deviatoric stress second invariant $\qquad J_2 = \dfrac{1}{2} s_{ij} s_{ij},$

- deviatoric stress $\qquad\qquad\qquad\qquad s_{ij} = \sigma_{ij} - \dfrac{1}{3} \sigma_{kk} \delta_{ij},$

- von Mises equivalent strain $\qquad\quad \varepsilon^{\text{ekv}}\left(\mathbf{\varepsilon}^{\text{vp}} \right) = \left(\dfrac{4}{3} J_2^{\text{vp strain}} \right)^{1/2},$

- deviatoric viscoplastic strain second invariant $\qquad J_2^{\text{vp strain}} = \dfrac{1}{2} e_{ij}^{\text{vp}} e_{ij}^{\text{vp}},$

- deviatoric viscoplastic strain $\qquad\quad e_{ij}^{\text{vp}} = \varepsilon_{ij}^{\text{vp}} - \dfrac{1}{3} \varepsilon_{kk}^{\text{vp}} \delta_{ij}.$

Other parameters which also highly influence damage model behaviour and predicted TMF life are structural temperature levels and their range.

A simplified approach also exists, it uses only total accumulated viscoplastic strain and viscoplastic strain accumulated during the last (stabilised) cycle as damage parameters. Viscoplastic strain accumulated during any time period is determined as [31]

$$\varepsilon_{\text{cum}}^{\text{vp}} = \int_{t_1}^{t_2} \sqrt{\frac{2}{3} \dot{\mathbf{\varepsilon}}^{\text{vp}}(t) : \dot{\mathbf{\varepsilon}}^{\text{vp}}(t)} \; dt, \tag{3.26}$$

where t_1 and t_2 define the time period for which the accumulated viscoplastic strain is calculated.

3.6. Finite Elements used for TMF Analysis [31], [32], [33]

3.6.1. Linear Hexahedron Element

For stress analyses carried out in the scope of this thesis, 3D continuum hexahedron (8-node linear brick) elements with full integration (8 integration points) were used. These elements are named C3D8 in SIMULIA Abaqus® software. Single C3D8 element is shown in Figure 3.4.
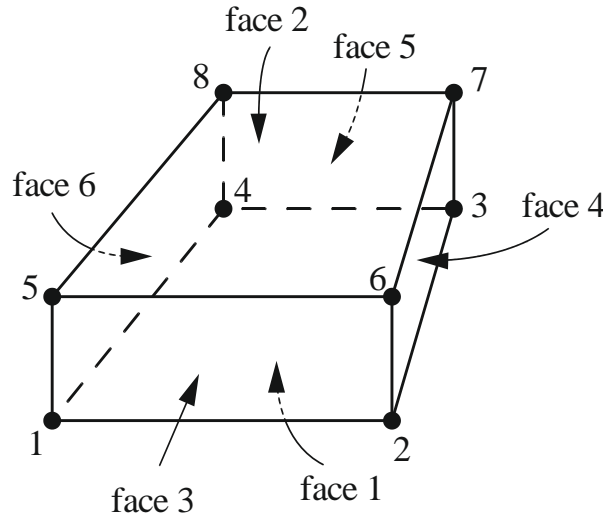
Figure 3.4. Linear brick element

In strength analysis procedure this type of element possesses 3 degrees of freedom in every node. Those 3 degrees of freedom are displacements in all three directions of Cartesian coordinate system. Element nodal displacement vector is

$$\mathbf{v}^{\mathrm{T}} = \begin{bmatrix} \mathbf{v}_1 & \mathbf{v}_2 & \mathbf{v}_3 & \mathbf{v}_4 & \mathbf{v}_5 & \mathbf{v}_6 & \mathbf{v}_7 & \mathbf{v}_8 \end{bmatrix},$$
$$\mathbf{v}_i^{\mathrm{T}} = \begin{bmatrix} u_i & v_i & w_i \end{bmatrix}, \quad i = 1, 2, 3, \ldots, 8. \tag{3.27}$$

Displacement field is represented by an incomplete third degree polynomial

$$u = a_1 + a_2 x + a_3 y + a_4 z + a_5 xy + a_6 yz + a_7 zx + a_8 xyz,$$
$$v = a_9 + a_{10} x + a_{11} y + a_{12} z + a_{13} xy + a_{14} yz + a_{15} zx + a_{16} xyz, \tag{3.28}$$
$$w = a_{17} + a_{18} x + a_{19} y + a_{20} z + a_{21} xy + a_{22} yz + a_{23} zx + a_{24} xyz.$$

This type of finite elements is mostly used to mesh structures or structure areas where relatively uniform stress distribution is expected. Hexahedral elements formulated as an isoparametric

elements can be of an arbitrary shape (although with some distortion limitations). However, they are still not suitable for meshing the highly complex or curved geometry.

Fully integrated elements in Abaqus® do not hourglass but may suffer from "locking" behaviour: both shear and volumetric locking. Shear locking occurs in first-order, fully integrated elements (CPS4, CPE4, C3D8, etc.) that are subjected to bending. The numerical formulation of the elements gives rise to shear strains that do not really exist - the so-called parasitic shear. Therefore, these elements are too stiff in bending, in particular if the element length is of the same order of magnitude as or greater than the wall thickness [32].

Volumetric locking occurs in fully integrated elements when the material behaviour is (almost) incompressible. Spurious pressure stresses develop at the integration points, causing an element to behave too stiffly for deformations that should cause no volume changes. If materials are almost incompressible (elastic-plastic materials for which the plastic strains are incompressible), second-order, fully integrated elements start to develop volumetric locking when the plastic strains are on the order of the elastic strains. However, the first-order, fully integrated quadrilaterals and hexahedra use selectively reduced integration (reduced integration on the volumetric terms). Therefore, these elements do not lock with almost incompressible materials. Reduced-integration, second-order elements develop volumetric locking for almost incompressible materials only after significant straining occurs. In this case, volumetric locking is often accompanied by a mode that looks like hour glassing. Frequently, this problem can be avoided by refining the mesh in regions of large plastic strain [32].

In case of HT analysis, this type of element in Abaqus® is named DC3D8. Every node of DC3D8 element has only one degree of freedom, that one being temperature. Element degrees of freedom vector is then

$$\mathbf{T}^{\mathrm{T}} = \begin{bmatrix} T_1 & T_2 & T_3 & T_4 & T_5 & T_6 & T_7 & T_8 \end{bmatrix}. \tag{3.29}$$

Temperature field is represented by an incomplete third degree polynomial

$$T = a_1 + a_2 x + a_3 y + a_4 z + a_5 xy + a_6 yz + a_7 zx + a_8 xyz. \tag{3.30}$$

3.6.2. Quadratic Tetrahedron Element

Another type of 3D continuum finite elements for stress analyses carried out in the scope of this thesis is quadratic (second-order) tetrahedron finite element named C3D10 in SIMULIA Abaqus® software. C3D10 element is shown in Figure 3.5.
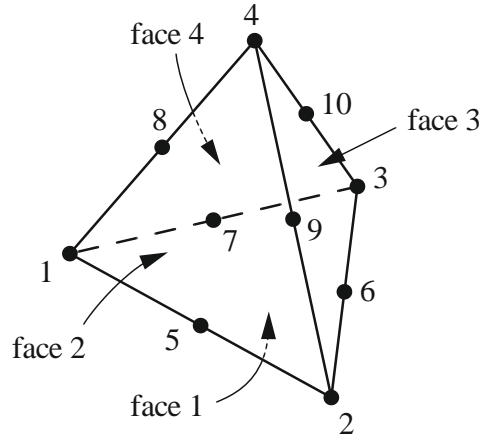
Figure 3.5. Quadratic tetrahedron element

This element has 10 nodes with 3 degrees of freedom in each of the nodes, totalling 30 degrees of freedom per element. Those 3 degrees of freedom are displacements in all three directions of Cartesian coordinate system. Element nodal displacement vector is

$$\mathbf{v}^{\mathrm{T}} = \begin{bmatrix} \mathbf{v}_1 & \mathbf{v}_2 & \mathbf{v}_3 & \mathbf{v}_4 & \mathbf{v}_5 & \mathbf{v}_6 & \mathbf{v}_7 & \mathbf{v}_8 & \mathbf{v}_9 & \mathbf{v}_{10} \end{bmatrix},$$
$$\mathbf{v}_i^{\mathrm{T}} = \begin{bmatrix} u_i & v_i & w_i \end{bmatrix}, \quad i = 1, 2, 3, \dots, 10. \tag{3.31}$$

Displacement field is represented by a complete second degree polynomial

$$u = a_1 + a_2 x + a_3 y + a_4 z + a_5 x^2 + a_6 y^2 + a_7 z^2 + a_8 xy + a_9 yz + a_{10} zx,$$
$$v = a_{11} + a_{12} x + a_{13} y + a_{14} z + a_{15} x^2 + a_{16} y^2 + a_{17} z^2 + a_{18} xy + a_{19} yz + a_{20} zx, \tag{3.32}$$
$$w = a_{21} + a_{22} x + a_{23} y + a_{24} z + a_{25} x^2 + a_{26} y^2 + a_{27} z^2 + a_{28} xy + a_{29} yz + a_{30} zx.$$

This element has a strain field that is linear in coordinates. The element can therefore represent fields of pure bending exactly.

One key advantage of tetrahedral elements is that they provide geometrical versatility and most automatic meshing algorithms utilize these types of elements.

"Upon applying a uniform pressure load to a face of C3D10 elements, these elements generate zero nodal forces at corner node rendering them not suitable for contact simulations. This drawback could be negated with the usage of finite sliding surface to surface formulation for contact. ABAQUS recommends using this combination for any contact analysis with C3D10 tetrahedral elements. Here enforcement method also plays a crucial role. C3D10 elements are recommended for any contact involving finite sliding with node to surface or surface to surface formulation when used with penalty enforcement method which is the default method in ABAQUS/Standard for contact enforcement" [34].

"C3D10 elements do not yield desirable results when used with finite sliding, node to surface formulation and direct enforcement method. With C3D10M elements, a significant improvement in contact results can be noted with above combination. Ideal usages include modelling edge to surface or point to surface contact with direct enforcement. However ABAQUS no longer recommends C3D10M elements for this type of contact as well. C3D10 elements with node to surface formulation and penalty enforcement method are ideally recommended. C3D10M elements come with certain disadvantages. They are "modified" formulation elements using bilinear interpolation and hence, they are not a true second-order element. Basically, this means that C3D10M will be unable to capture curvature as smoothly as C3D10 elements. Hence, should not be used for master regions in a contact pair. They also do not capture bending well due to their formulation" [34].

"C3D10I are "improved" formulation elements. They behave in much the same way as C3D10 elements. However, their integration points are at the element nodes. Hence, results based on integration points (such as stresses and strains) do not suffer from extrapolation errors, as with C3D10 or C3D10M. It is for this reason that these elements are said to have "improved surface stress visualization". In this sense, C3D10I is a good choice for fatigue problems where surface stresses are critical. Further, C3D10I automatically invokes internal constraints to handle incompressible (or nearly incompressible) materials, such as hyperelasticity or plasticity. As for contact, the guidelines are exactly the same as for C3D10. Even though C3D10I elements are computationally more costly, they do not provide any additional advantage over C3D10 for contact analysis" [34].

In case of HT analysis, this type of element in Abaqus® is named DC3D10. Now every one of 10 nodes of this element has only one degree of freedom, that one being temperature. Element degrees of freedom vector is then

$$\mathbf{T}^{\mathrm{T}} = \begin{bmatrix} T_1 & T_2 & T_3 & T_4 & T_5 & T_6 & T_7 & T_8 & T_9 & T_{10} \end{bmatrix}. \tag{3.33}$$

Temperature field is represented by a complete second degree polynomial

$$T = a_1 + a_2 x + a_3 y + a_4 z + a_5 x^2 + a_6 y^2 + a_7 z^2 + a_8 xy + a_9 yz + a_{10} zx. \tag{3.34}$$

3.6.3. Quadratic Triangular Prism (Wedge) Element

Last type of 3D continuum finite elements for heat transfer analysis used in the scope of this thesis is quadratic (second-order) triangular prism (wedge) finite element named DC3D15 in SIMULIA Abaqus® software. DC3D15 element is shown in Figure 3.6.
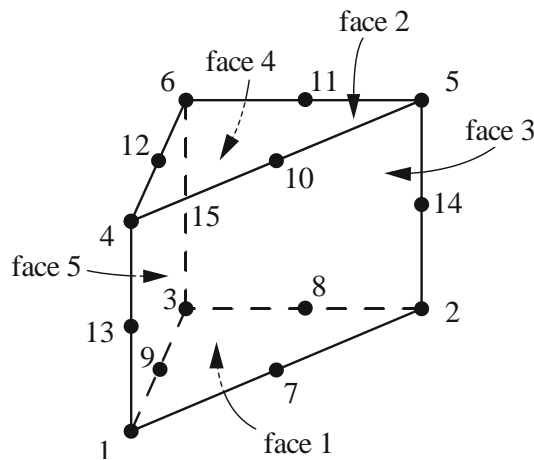

Figure 3.6. Quadratic triangular prism element

Every one of 15 nodes of this element has only one degree of freedom, that one being temperature. Element degrees of freedom vector then looks like

$$\mathbf{T}^{\mathrm{T}} = \begin{bmatrix} T_1 & T_2 & T_3 & T_4 & T_5 & T_6 & T_7 & T_8 & T_9 & T_{10} & T_{11} & T_{12} & T_{13} & T_{14} & T_{15} \end{bmatrix}. \tag{3.35}$$

Temperature field is represented by an incomplete third degree polynomial

$$T = a_1 + a_2 x + a_3 y + a_4 z + a_5 x^2 + a_6 y^2 + a_7 z^2 + a_8 xy + a_9 yz + a_{10} xz +$$
$$+ a_{11} xyz + a_{12} x^2 z + a_{13} y^2 z + a_{14} xz^2 + a_{15} yz^2 .$$

(3.36)

Using triangular prism elements can be useful when modelling complex-shaped domains. In those situations hexahedral elements may pose some difficulties, especially when it comes to discretising curved geometry. In order to avoid using large number of hexahedral (brick-shaped) elements, triangular prism elements can be used along hexahedral elements to alleviate that problem and ensure better geometry representation.

In strength analysis procedure this type of element in Abaqus® is named C3D15 and it possesses 3 degrees of freedom in every node. Those 3 degrees of freedom are displacements in all three directions of Cartesian coordinate system. This type of finite elements is not used in the scope of this thesis.

3.7. FEM Verification Examples

It is always useful to verify the FEM analysis results because, as it is already said, FEM is a numerical method which only provides approximate solutions. For that reason, two simple examples are solved analytically and numerically. Obtained numerical results are compared against analytical solutions for different finite element types (tetrahedral C3D10 and hexahedral C3D8) and different number of finite elements used to discretize the geometry. Both examples are one-dimensional (1D) HT problems but numerical solutions are obtained for 3D numerical models which are reduced to 1D HT problems with correct thermal load and boundary condition application.

3.7.1. Steady State Heat Transfer

This problem is 1D simplification of steady state HT analysis between exhaust manifold (EM) and its surrounding through a heat shield (HS). Simplification implies constant (not temperature dependent) material properties, constant (not spatially dependent) boundary conditions and simplified geometry (two plates).
Steady state HT problem is defined as shown in Figure 3.7.
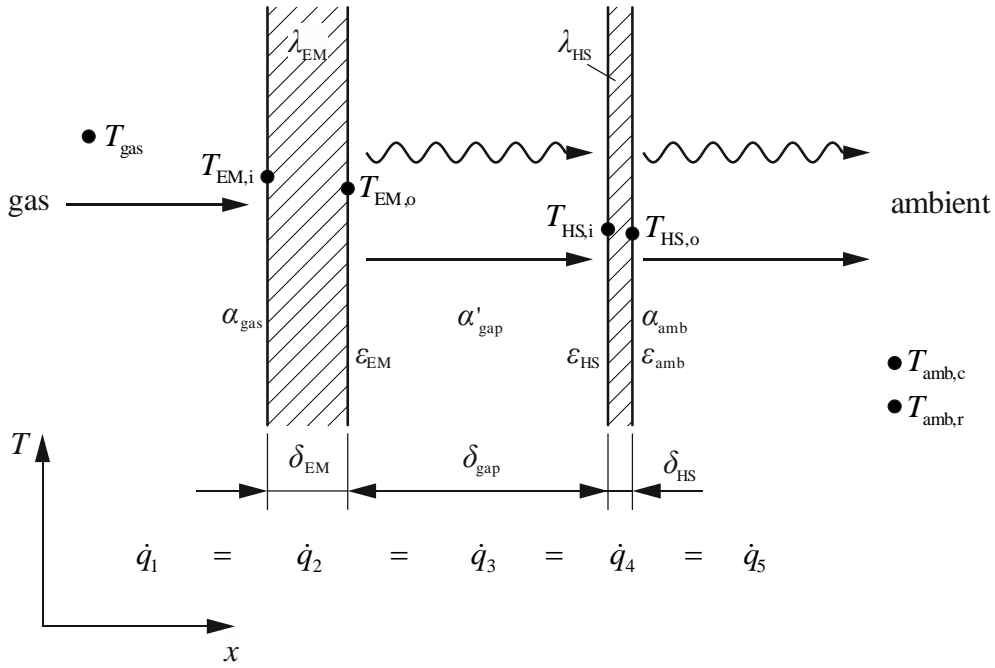
Figure 3.7. Steady state HT problem definition

Parameters used to define this problem have the following values:

- gas temperature, $T_{gas} = 700\ °C$,

- gas side convective heat transfer coefficient, $\alpha_{gas} = 1000\ \text{W}/\left(\text{m}^2\text{K}\right)$,

- exhaust manifold thickness, $\delta_{EM} = 4\ \text{mm}$,

- exhaust manifold thermal conductivity, $\lambda_{EM} = 32\ \text{W}/\left(\text{mK}\right)$,

- gap width, $\delta_{gap} = 10\ \text{mm}$,

- gap thermal conductance, $\alpha'_{gap} = \dfrac{\lambda_{air}}{\delta_{gap}} = 6.114 \cdot 10^{-6}\ \text{W}/\left(\text{m}^2\text{K}\right)$,

- heat shield thickness, $\delta_{HS} = 1.2\ \text{mm}$,

- heat shield thermal conductivity, $\lambda_{HS} = 40\ \text{W}/\left(\text{mK}\right)$,

- emissivity coefficient between exhaust manifold and heat shield (both surfaces), $\varepsilon_{EM} = \varepsilon_{HS} = 0.8$,

- surface ratio, $\omega = \dfrac{A_{HS}}{A_{EM}} = 1$,

- ambient temperature for convection, $T_{amb,c} = 75\ °C$,

- convective heat transfer coefficient to ambient, $\alpha_{amb} = 15\ \text{W}/\left(\text{m}^2\text{K}\right)$,

- ambient temperature for radiation, $T_{amb,r} = 30\ ^\circ\mathrm{C}$,

- emissivity coefficient to ambient, $\varepsilon_{amb} = 0.2$ and

- Stefan-Boltzmann constant, $\sigma = 5.6704 \cdot 10^{-8}\ \mathrm{W}/\left(\mathrm{m}^2\mathrm{K}^4\right)$.

3.7.1.1. Analytical Solution of the Steady State Heat Transfer Problem

Solution of this problem are surface temperatures of EM (inside and outside) and HS (inside and outside). This problem can be easily solved by splitting it into several logical sections and applying the condition that specific heat fluxes through each of them are equal and constant because this is steady state HT problem. This means that overall specific heat flux from the gas to the ambient is equal to specific heat flux between any other two points of that system. These logical sections can be seen and distinguished in Figure 3.7.

Condition of equal and constant heat fluxes can be written as

$$\dot{q}_1 = \dot{q}_2 = \dot{q}_3 = \dot{q}_4 = \dot{q}_5 = \text{const}. \tag{3.37}$$

Required surface temperatures can be obtained from Equation (3.37) and specific heat fluxes can be calculated as:

$$\dot{q}_1 = \alpha_{amb}\left(T_{HS,o} - T_{amb,c}\right) + \varepsilon_{amb}\sigma\left(T_{HS,o}^4 - T_{amb,r}^4\right), \tag{3.38}$$

$$\dot{q}_2 = \frac{\lambda_{HS}}{\delta_{HS}}\left(T_{HS,i} - T_{HS,o}\right), \tag{3.39}$$

$$\dot{q}_3 = \alpha'_{gap}\left(T_{EM,o} - T_{HS,i}\right) + \frac{\sigma}{\dfrac{1}{\varepsilon_{EM}} + \omega\left(\dfrac{1}{\varepsilon_{HS}} - 1\right)}\left(T_{EM,o}^4 - T_{HS,i}^4\right), \tag{3.40}$$

$$\dot{q}_4 = \frac{\lambda_{EM}}{\delta_{EM}}\left(T_{EM,i} - T_{EM,o}\right), \tag{3.41}$$

$$\dot{q}_5 = \alpha_{gas}\left(T'_{gas} - T_{EM,i}\right). \tag{3.42}$$

This system of equations can be solved iteratively by presuming value for $T_{HS,o}$ until

$$\frac{T'_{gas} - T_{gas}}{T_{gas}} < \text{maximum defined relative error} ,\tag{3.43}$$

where T'_{gas} is calculated gas temperature for presumed $T_{HS,o}$ in any iteration step.

To obtain the value of the unknown temperature $T_{EM,o}$ from Equation (3.40) an iterative approach is also required.

3.7.1.2. Numerical Solution of the Steady State Heat Transfer Problem

Numerical model is shown in Figure 3.8. Thermal load and boundary conditions are applied according to Figure 3.7.

Enlarged detail of structured hexahedral mesh model with two DC3D8 elements through thickness of both the exhaust manifold and the heat shield.

DC3D8

DC3D10

DC3D15

X
Z   Y

Enlarged details of tetrahedral (DC3D10) and triangular prism (DC3D15) mesh models with two layers of elements through thickness of both the exhaust manifold and the heat shield.

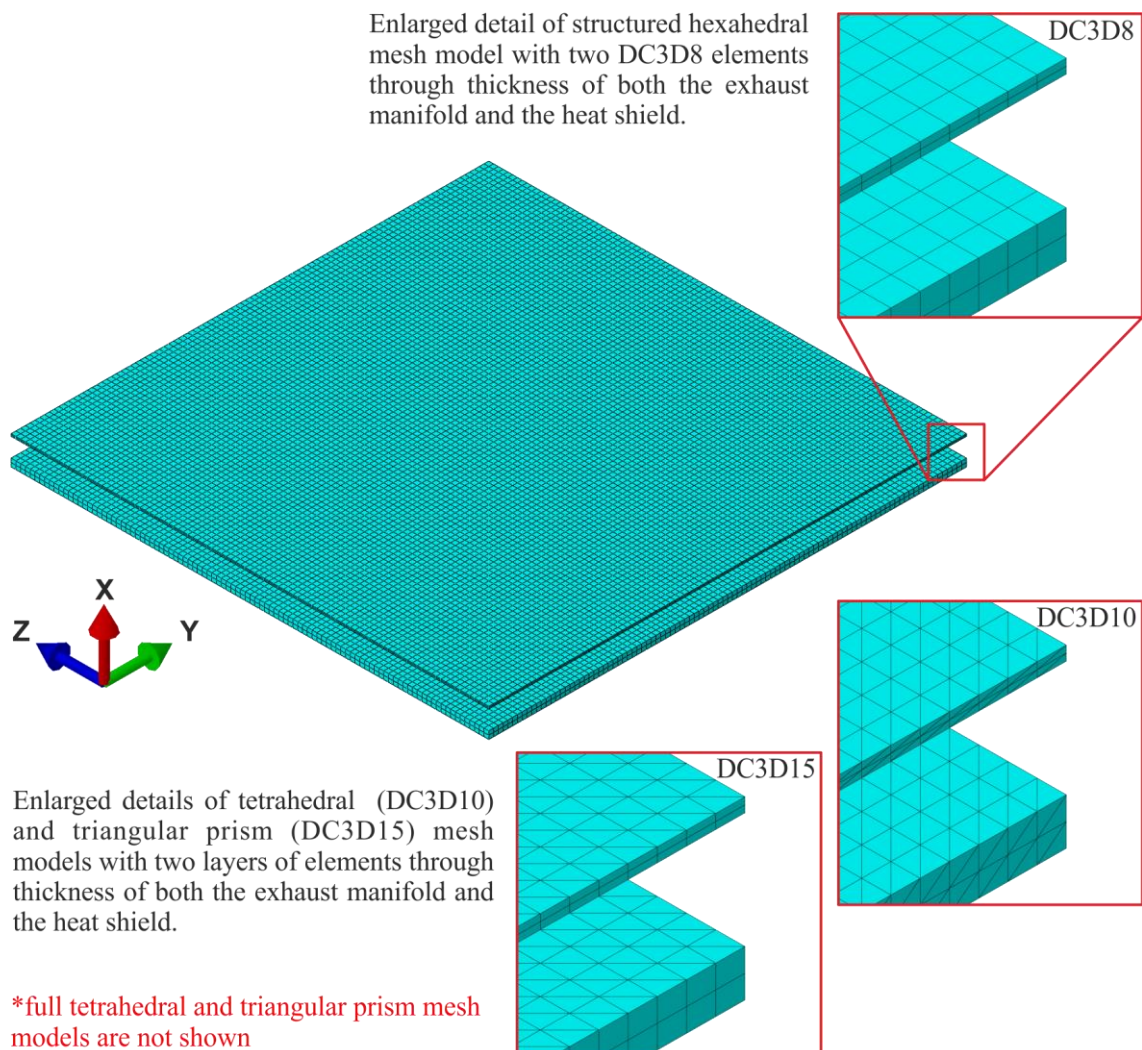*full tetrahedral and triangular prism mesh models are not shown

Figure 3.8. Steady state HT problem numerical model

Each surface temperature is read for several surface element nodes to ensure that they are consistent, ensuring uniform surface temperatures and also that this is indeed 1D HT problem. For each surface temperature 6 different solutions were obtained. Problem was solved for three element types (DC3D8, DC3D10 and DC3D15) and with each element type for two mesh densities. Solutions obtained from all numerical models showed negligible difference or no difference at all between different element types. Maximum absolute difference of solutions obtained for different element types is 0.004°C.

Relative difference to calculated analytical solution will be shown only for numerical solution obtained for the denser tetrahedral mesh (two layers of C3D10 elements through thickness of both EM and HS) as shown in Table 3.1. The reason is that this solution also represents relative difference for the other two denser mesh models as well.

Table 3.1. Steady state HT problem results comparison

Steady state HT problem analytical and numerical solutions					
Surface temperature		$T_{EM,i}$	$T_{EM,o}$	$T_{HS,i}$	$T_{HS,o}$
Analytical solution [°C]		**686.823**	**685.176**	**573.149**	**572.754**
Tetrahedral mesh	Numerical solution [°C]	686.824	685.177	573.137	572.742
Relative difference to analytical solution		0.00%	0.00%	-0.00%	-0.00%
Hexahedral mesh	Numerical solution [°C]	686.824	685.178	573.141	572.745
Triangular prism mesh	Numerical solution [°C]	686.824	685.178	573.141	572.745

Coarser mesh numerical models gave very accurate results and doubling the number of elements through EM and HS thickness resulted in nearly identical results. Solutions showed excellent agreement with analytical solution and for that reason convergence will not be shown or further discussed.

For that same reason, only the temperature field distribution of the denser tetrahedral mesh model will be shown graphically in Figure 3.9.
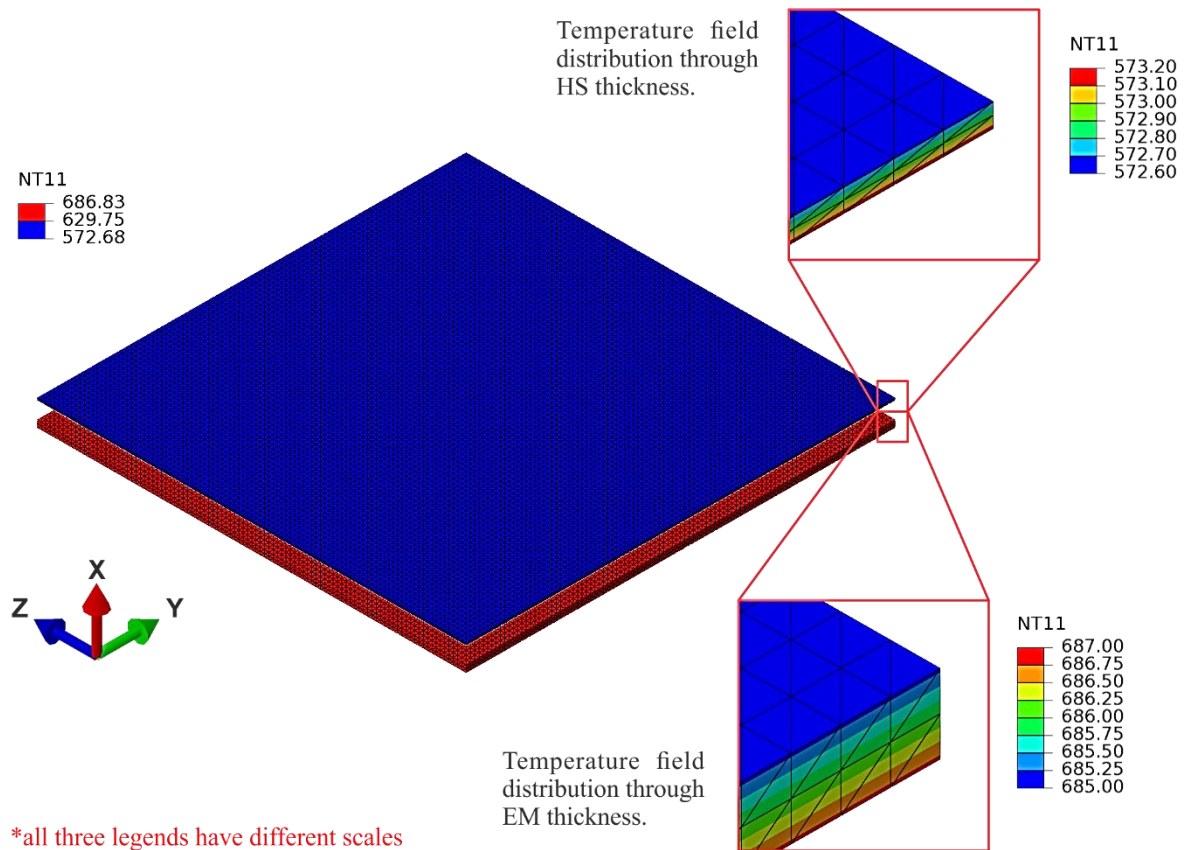
Figure 3.9. Steady state HT problem numerical solution

Temperature field distribution cannot be adequately visualised for the entire model which shows both the EM and HS. This is because temperature differences between inside and outside surfaces of both components are negligible ($\approx 1\ ^{\circ}\mathrm{C}$) when compared to large temperature difference between the both components average temperature ($\approx 100\ ^{\circ}\mathrm{C}$).

This is the result of very low thermal conductivity of the air gap when compared to thermal conductivity of both EM and HS.

For that reason legends of enlarged details of EM and HS in Figure 3.9. have different colour scales.

3.7.2. Transient Heat Transfer

Analysed 1D transient (time dependent) HT problem is very similar to Example 2.1.3, found in [35]. This example should demonstrate the influence of time component on heat transfer process (thermal inertia) through thicker parts of ICE exhaust system, e.g. flanges. Temperature of each point through wall thickness is both time and space dependent (but only in the direction of the heat flux). The problem is defined by wall properties and isothermal boundary conditions (Dirichlet boundary conditions).

Wall properties and boundary conditions are defined as shown in Figure 3.10.
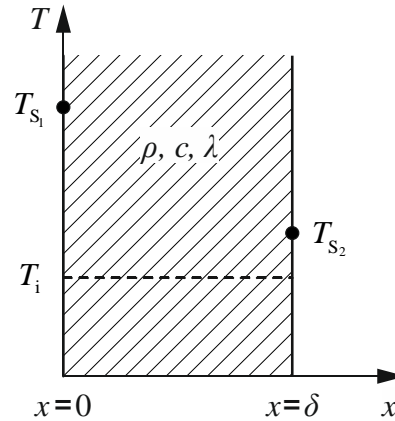
Figure 3.10. Transient HT problem definition

Parameters have the following values:

- thickness, $\delta = 50\,\text{mm}$,

- thermal conductivity, $\lambda = 32\,\text{W}/(\text{mK})$,

- specific heat capacity, $c = 540\,\text{J}/(\text{kgK})$,

- material density, $\rho = 7800\,\text{kg}/\text{m}^3$,

- initial temperature, $T_i = 20\,°\text{C}$,

- left surface boundary condition (higher) temperature, $T_{S_1} = 50\,°\text{C}$,

- right surface boundary condition (lower) temperature, $T_{S_2} = 30\,°\text{C}$.

3.7.2.1. Analytical Solution of the Transient Heat Transfer Problem

Analytical solution can be expressed as [35]

$$T(x,t) = T_{S_1} - \left(T_{S_1} - T_{S_2}\right)\frac{x}{\delta} + \frac{2}{\pi}\sum_{n=1}^{\infty}\frac{1}{n}\left[\left(T_i - T_{S_1}\right) - (-1)^n\left(T_i - T_{S_2}\right)\right]e^{-(n\pi)^2 Fo}\sin\left(\frac{n\pi}{\delta}x\right), \tag{3.44}$$

where *Fo* is Fourier number which can be expressed as

$$Fo = \frac{at}{\delta^2}. \tag{3.45}$$

Symbol *a* in Equation (3.45) represents thermal diffusivity and it is calculated as

$$a = \frac{\lambda}{\rho c}.$$ (3.46)

Analytical solution obtained by solving the Equation (3.44), used for comparison with numerical solution, was calculated for $n = 1, 2$ and 3 and this was accurate enough to show excellent agreement between results for values of Fourier number larger than 0.015 ($Fo > 0.015$) what in this case corresponds to time points beyond 5 seconds ($t > 5\,\text{s}$). A single solution is defined with a pair of input variables, space coordinate *x* and time moment *t*.

3.7.2.2.   Numerical Solution of the Transient Heat Transfer Problem

Numerical models discretized with the densest meshes of quadratic tetrahedron DC3D10 elements, linear hexahedron DC3D8 elements and quadratic triangular prism DC3D15 elements are shown in Figure 3.11. All graphically shown models have the same number of nodes throughout the wall thickness, which is 17 nodes.
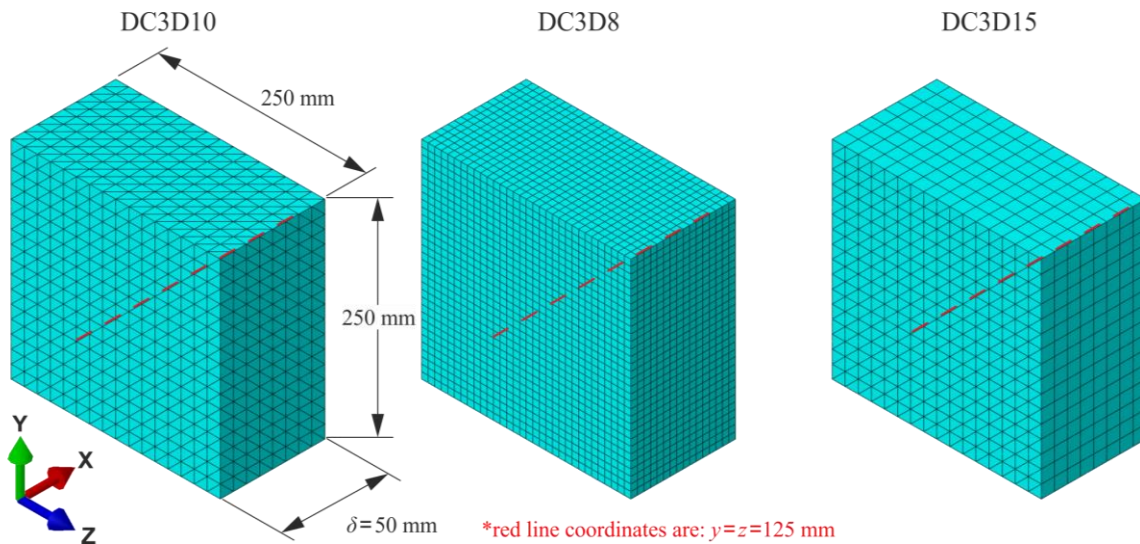

Figure 3.11. Transient HT problem numerical model geometry discretized with tetrahedral mesh (left), hexahedral mesh (middle) and triangular prism mesh (right)

Boundary conditions (uniform surface temperatures) are applied according to Figure 3.10. and total simulation time is set to $t = 100\,\text{s}$.

Solutions for all numerical models are read only from the element nodes located along the axis passing through the middle of numerical model marked with red dashed line in Figure 3.11.

Numerical solutions are calculated for different element types and different numbers of elements used to discretize the geometry. Since this is 1D heat transfer problem, only the number of elements (nodes) per thickness of the wall is relevant for convergence analysis. Calculated analytical and numerical solutions are compared below in Table 3.2.

All compared solutions are calculated for the following pair of input parameters:

$x = 25\,\text{mm}$ and
$t = 40\,\text{s}$.

Table 3.2. Transient HT problem results comparison

Transient HT problem analytical and numerical solutions for $x = 25\,\text{mm}$ and $t = 40\,\text{s}$						
Analytical solution [°C]		**32.3282**				
Number of nodes through wall thickness		**3**	**5**	**9**	**13**	**17**
Tetrahedral mesh	Solution [°C]	32.1909	32.1313	32.2482	32.2579	32.2591
Relative difference to analytical solution		-0.42%	-0.61%	-0.25%	-0.22%	-0.21%
Hexahedral mesh	Solution [°C]	32.2518	32.2182	32.2436	32.2522	32.2554
Relative difference to analytical solution		-0.34%	-0.29%	-0.26%	-0.24%	-0.23%
Triangular prism mesh	Solution [°C]	32.5193	32.2204	32.2574	32.26	32.2606
Relative difference to analytical solution		0.59%	-0.33%	-0.22%	-0.21%	-0.21%

Analytical solution and numerical solutions obtained by all element types show excellent agreement even for the coarsest meshes. Differences between different element types exist, but they are negligible. All numerical solutions can be considered accurate enough since their relative differences when compared to analytical solution are less than 1%.

Convergence of solution for $x = 25\,\text{mm}$ and $t = 40\,\text{s}$ and for all element types is graphically shown in Figure 3.12.

Figure 3.12. Transient HT problem FEM solution convergence

Analytical and numerical solutions for different time moments t and temperature distribution at $t = 40\,\text{s}$ calculated for the densest tetrahedral mesh model are shown in Figure 3.13.

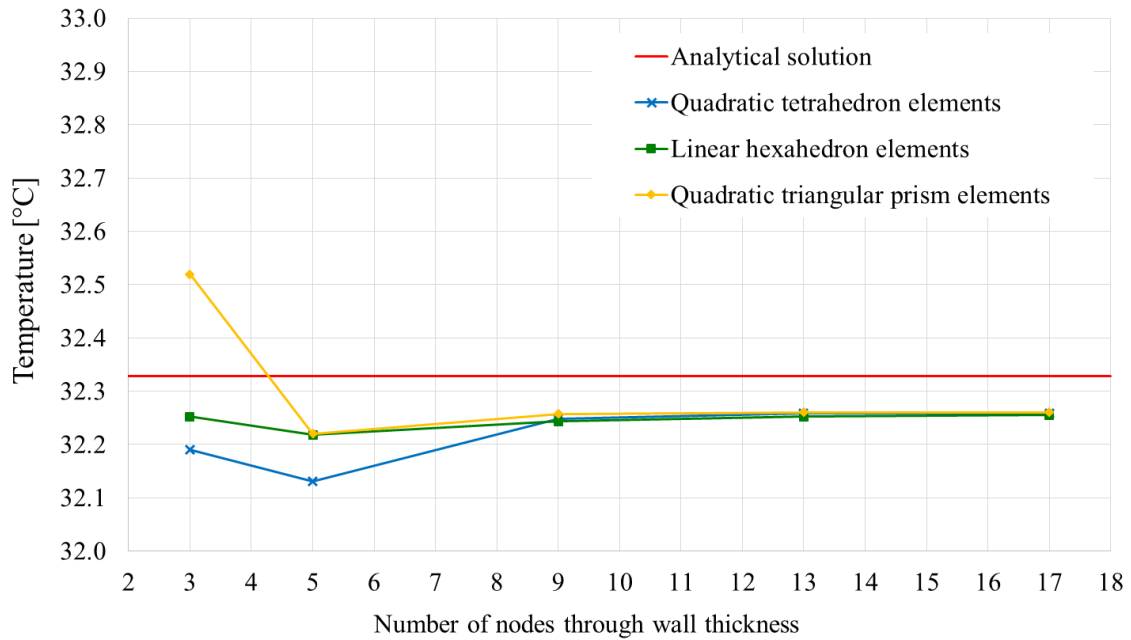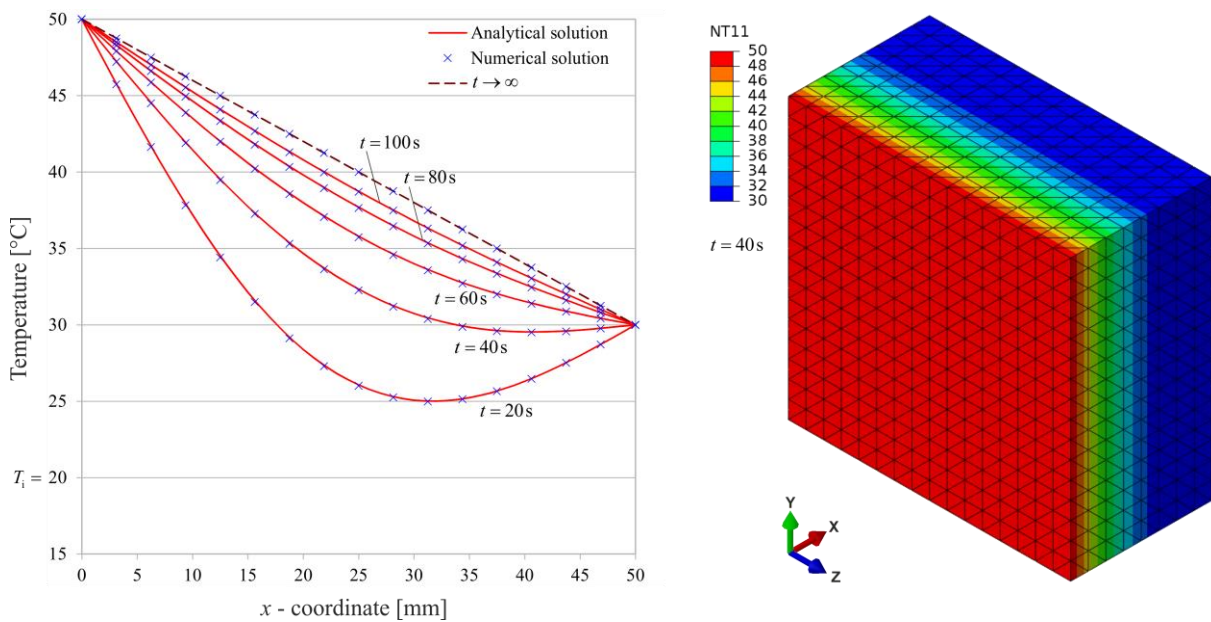**Figure 3.13. Transient HT problem analytical and numerical solutions for different time moments t and temperature field distribution at $t = 40\,\text{s}$**

4. Workflow and Analyses Description

AVL has a fully developed and well tested TMF life prediction procedure. Due to confidentiality reasons some of the details and steps of that TMF workflow will not be discussed in the scope of this thesis or they will be intentionally left out.

It should also be noted that due to confidentiality reasons, all figures showing model geometry or any part of it are intentionally blurred or distorted.

In addition to that, material properties of all components included in the simulation models will not be disclosed in much detail.

The internal combustion engine simulated in the scope of this thesis was chosen for a reason. The reason is that design of this engine and its exhaust system was already evaluated and tested by AVL using both numerical simulations and actual hardware testing on a test bed.

The initial design evaluation, which also included TMF life evaluation, confirmed that there were several locations on the exhaust manifold which began to crack well below the limit set for this component and this specific application. This problem was later resolved by minor design changes.

By choosing this exact engine, influence of engine orientation and exhaust manifold mounting position variation on predicted TMF life of both areas which are likely to fail and those which are not is enabled.

4.1. AVL TMF Workflow Overview

The AVL TMF simulation method algorithm is very similar to a generic numerical fatigue analysis algorithm shown in figure Figure 3.3. and it involves the following simulation steps:

1. transient heat transfer analysis (with control steady state HT analysis),
2. nonlinear structural stress-strain analysis under cyclic thermal load and
3. fatigue life prediction based on the AVL damage model.

As already said in Chapter 3.5.1, AVL's TMF damage model used for EM lifetime prediction is based on several output quantities calculated from the last simulated cycle of sequentially coupled thermo-mechanical analyses.

Damage model used in the scope of this thesis is a function of stress range, accumulated viscoplastic strain range, maximum temperature and average temperature calculated in the last simulated cycle.

Therefore, TMF life N_f, predicted by this damage model can be written as

$$N_f = N_f \left(\Delta S, \Delta \varepsilon^{vp}, T_{max}, T_{avg} \right). \tag{4.1}$$

Due to confidentiality reasons, the exact formulation of the damage model will not be disclosed.

Also, it should be noted that AVL's TMF simulation procedure is developed to be carried out with finite element software SIMULIA Abaqus® by Dassault Systèmes.

List of all the required analysis inputs and outputs are given in Table 4.1. and Table 4.2. respectively.

Table 4.1. AVL TMF simulation inputs

AVL TMF simulation inputs	
Geometry / Topology	
Main engine data	*Bore, stroke, power output, ...*
3D-CAD cylinder head assembly	*Cylinder head*
3D-CAD exhaust system assembly	*Exhaust manifold, turbocharger, bolts, ...*
Properties	
Gasket behaviour	*Gasket behaviour and properties*
Exhaust manifold material properties	*Temperature dependent data*
Material properties of all other parts	*Temperature dependent data*
Loads and Boundary Conditions	
Bolt forces	*Maximum forces*
Gas, coolant and oil (near wall) temperatures	*From CFD analyses*
Gas, coolant and oil heat transfer coefficients	*From CFD analyses*
Thermal cycle definition	

Table 4.2. AVL TMF simulation outputs

AVL TMF simulation outputs	
Output physical quantity	**Remark**
Temperature field	*Hot and cold engine condition*
Displacement field	*Hot and cold engine condition*
Stress field	*Hot and cold engine condition*
Elastic and inelastic strains	*Hot and cold engine condition*
EM peak temperature	
Temperature range (idle & full thermal load)	
Stress range (idle & full thermal load)	
Inelastic strain range (idle & full thermal load)	
Dissipative plastic energy per cycle	
$\log_{10}$ of cycles to failure	

4.2. Simulated Internal Combustion Engine

The engine simulated in the scope of this thesis is a 1.2-liter turbocharged three-cylinder diesel engine with more technical specifications provided in Table 4.3.

Table 4.3. Simulated internal combustion engine technical specifications

Simulated internal combustion engine technical specifications		
Property	**Unit**	**Value / Type**
Application	/	Passenger car
Number of cylinders	/	3
Configuration	/	In Line
Fuel injection system	/	Common rail
Turbocharged	/	Yes
Swept volume	l	1.2
Max. torque	Nm	200
Max. torque speed (min.)	rpm	2000
Fuel	/	Diesel

4.3. Finite Element Models and their Properties

FE models represent only the "hot" side of the simulated engine, i.e. the side to which the hottest components such as exhaust manifold, turbocharger and diesel particle filter (DPF) are mounted.

Heat transfer (or full) model contains:

- part ("half") of the cylinder block
- part ("half") of the cylinder head,
- complete exhaust manifold,
- complete turbocharger and compressor (with bearing housing),
- complete brackets, one for exhaust manifold and one for diesel particle filter (DPF),
- complete components of the exhaust system up to DPF (which is also included) and
- complete gaskets, studs, bolts and nuts which are connecting all parts included in the model.

For each sequentially coupled TMF analysis, two FE models were used.

The first FE model (larger) was used for heat transfer analyses and the second one (smaller) was used for stress-strain (strength) and fatigue life prediction analyses.

Details of finite element mesh for both FE models are given in Table 4.4.

Table 4.4. FE models - mesh size

FE models used for sequentially coupled TMF analyses			
FE model	**No. of finite elements**	**No. of nodes**	**Used element types**
Heat transfer	519744	1027159	DC3D10, DC3D15
Strength and fatigue	288939	550841	C3D10I, C3D10M

From Table 4.4. it can be seen that HT model is almost twice the size of strength model (in terms number of used finite elements).

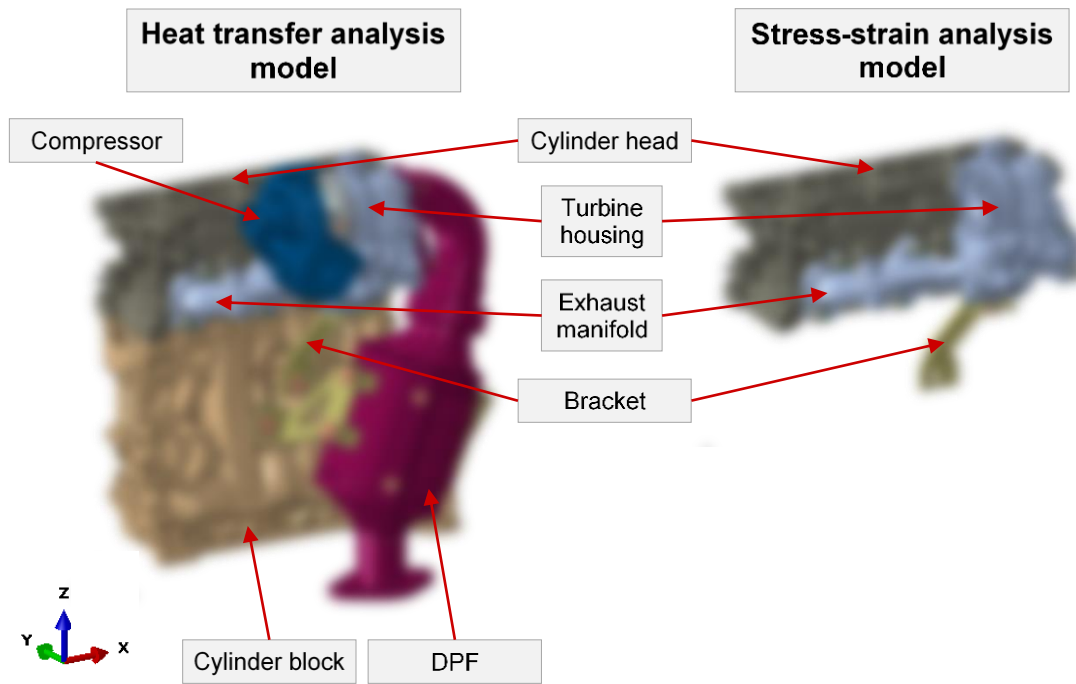Both FE models are shown in Figure 4.1.

Figure 4.1. Finite element models

The FE model used for strength and fatigue analyses is a reduced version of the heat transfer FE model which comprising only of the components which are necessary for the stress-strain and fatigue evaluation of the exhaust manifold.

To account for the exclusion of cylinder block from the strength FE model, mechanical constraints are applied to the cylinder head and EM bracket to areas which were in contact with the cylinder block in order to constrain global rigid body motion.

Also, in strength FE model, EM connection to the cylinder head is modelled with 8 bolts, and connection between EM and TC is modelled with 3 bolts. Bolt loads are calculated from the prescribed tightening torque for each bolt.

These mechanical constraints and connections act as stress and strain generators while the EM is exposed to cyclic thermal loading which causes thermal expansion (and contraction).

Exhaust manifold is made from nodular (ductile) cast iron, which is widely used for exhaust manifolds in automotive industry. All thermal and mechanical properties of EM are modelled as temperature dependent (nonlinear), as are those of most other employed materials in the FE models are also modelled as temperature dependent (nonlinear).

4.4. Load Cycle Definition

A simulation load cycle mimics typical load scenarios which many passenger car engines could experience during their operational life.

The TMF load cycle is defined in such a way that it simulates the worst possible conditions from the thermo-mechanical fatigue point of view. This means that thermal shock cycle imposes maximum thermo-mechanical shock on all engine components included in the model. This is achieved by rapid, but still physically possible, switching between characteristic engine operating points (full load, motored or idle). These operating points are defined by both thermal and mechanical loads and boundary conditions applied to the model (see Table 4.1.).

An example of AVL's generic TMF load cycle for passenger vehicles, is shown in Figure 4.2.
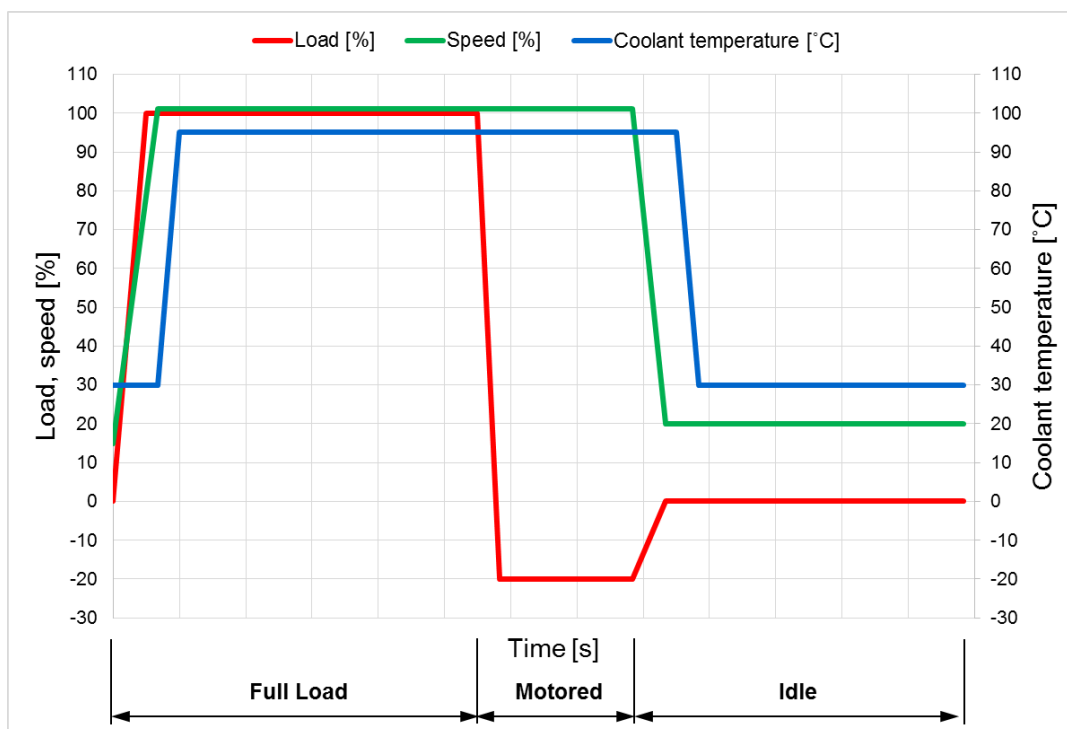
Figure 4.2. AVL TMF load cycle

This load cycle, shown in Figure 4.2., simulates the following vehicle driving conditions:

- **Full load (rated)** – uphill driving at full load (rated power) with hot coolant circulation,
- **Motored** – downhill driving (negative load) with the same number of RPM as in full power operating point with hot coolant circulation and
- **Idle** – idling (no load) at idle speed with cold coolant circulation.

Load cycle shown in Figure 4.2. is only an example. Exact parameters which define load cycle and its duration are adjusted for each simulated engine.

It should be noted that change between operating points is not instant (there is a linear ramp up and ramp down period), which makes the simulation more realistic by taking inertia of the vehicle and rotating masses into account.

Coolant temperature shown here is only the temperature of the coolant at coolant inlet. Coolant temperatures across the entire engine cooling system are not uniform or constant. Those temperatures are typically also predicted using a 3D CFD simulation.

New load cycle is defined for the investigation carried out in the scope of this thesis.

Individual load cases which this new load cycle are given in Table 4.5.

Table 4.5. Load cycle and individual load cases

TMF load cases defining the new load cycle		
Load name	**Speed**	**Description**
Rated	4000 rpm	Full load, 100 km/h highway uphill drive
Motored	4000 rpm	Negative load, 130 km/h highway downhill drive
Idle	800 rpm	Stationary vehicle, idling

Each of this load cases are defined in order to simulate the driving conditions which any passenger vehicle could undergo during its normal operational life.

4.5. General Analyses Setup and Model Variants

Three different model variants are simulated in order to investigate the influence of engine orientation and EM mounting position in the engine compartment on temperature distribution and estimated fatigue life.

Even though simulated model variants were different, used simulation procedure, explained in the remaining of this chapter, did not differ much between them.

4.5.1. General Analyses Setup

- All model variants have the exact same geometry (FE mesh) as ell as all applied mechanical loads and constraints.

- Thermal loads imposed by gas, oil and water are also identical across all variants in order to enable direct result comparison.

- Simulation model variants of three distinct installation configurations are defined by varying only the ambient heat transfer boundary conditions (HTBC's).

- Ambient HTBC's depend on installation configuration and TMF simulation load cases definition because simulation load cases also account for vehicle speed.

- All variants are simulated throughout the same load cycle comprised of the same load cases (rated, motored and idle).

Model variants are listed in Table 4.6. and visualised in Figure 4.3.

Table 4.6. Simulated model variants

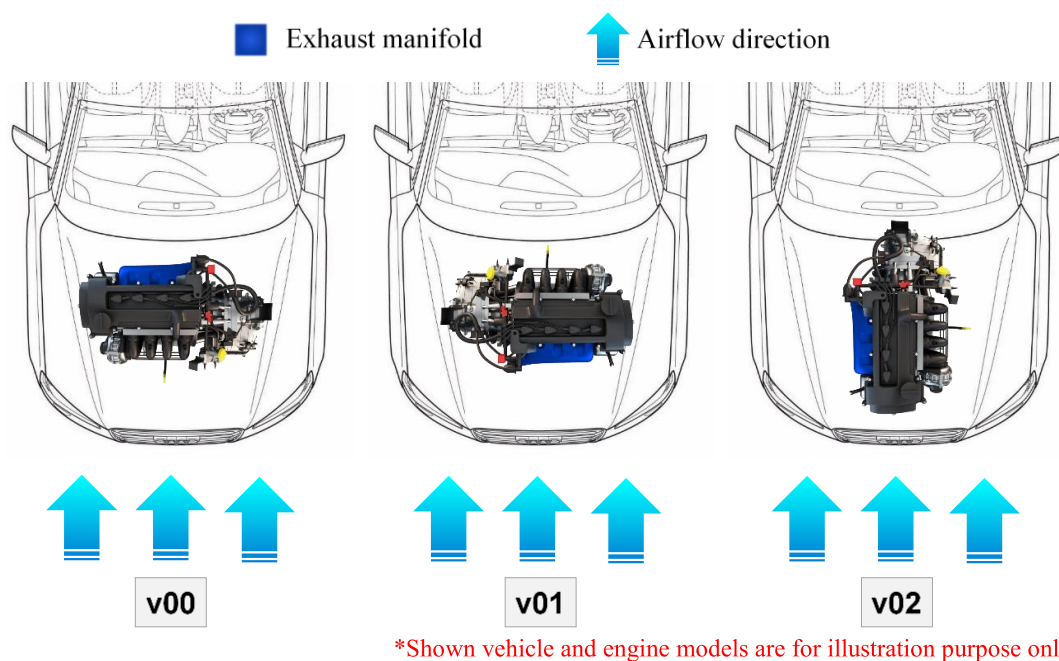| TMF simulation model variants		
Model variant	**Engine orientation**	**Exhaust manifold mounting position**
v00	transversal	EM mounted behind the engine (rear mounted)
v01	transversal	EM mounted in front of the engine (front mounted)
v02	longitudinal	EM mounted on the side of the engine (side mounted)

Figure 4.3. Illustration of all three simulated model variants [36], [37]

Relative position of the exhaust manifold, shown in Figure 4.3., implies that underhood airflow profile around it will change significantly between each simulated model variant.

Variation of the engine orientation and EM mounting position causes significant change in underhood airflow direction and magnitude relative to the components included in each model. This means that parameters which define heat transfer mechanism (cooling) between engine and its surrounding are also changed.

In other words, higher underhood airflow stream velocity near any component implies higher intensity of heat transfer process between the airflow stream and that component.

Another important thing to consider is that entire components or only some of their surfaces will be exposed to the direct (unobstructed) airflow stream, while others will be shielded by either the component itself or by some other component(s) obstructing the airflow stream.

In order to simulate this effect, new ambient thermal boundary conditions (HTBC's) are defined for all TMF load cases and for all three model variants.

These newly defined and applied ambient HTBC's are based on the results of multiple 3D CFD underhood airflow simulations provided by AVL.

4.5.1.1. Model Variant v00 – Rear Mounted Exhaust Manifold

Model variant v00 represents the transversely installed engine with EM mounted behind the engine (not exposed to direct airflow stream).

Because the EM and the back side of the engine in variant v00 are shielded from the direct airflow stream by the engine itself, it is presumed that vehicle speed doesn't have an influence on ambient HTBC's, i.e. ambient HTBC's are constant throughout the load cycle.
This is also confirmed by the data available from 3D CFD underhood simulation reports. From the 3D CFD simulation reports of all three vehicles it can be concluded that underhood airflow stream velocities behind the engine are uniform and very similar across all CFD load cases and are also much lower than in front or along either side of the engine.

Current (April 2017) AVL TMF workflow, which does not account for vehicle speed, is well suited to simulate these exact conditions.
Therefore v00 will be simulated in accordance with the current AVL TMF workflow and
For that reason, model variant v00 will serve as a reference point and all further analyses results will be compared against it.

In Figure 4.4., variant v00 installation configuration with underhood airflow stream direction is shown.
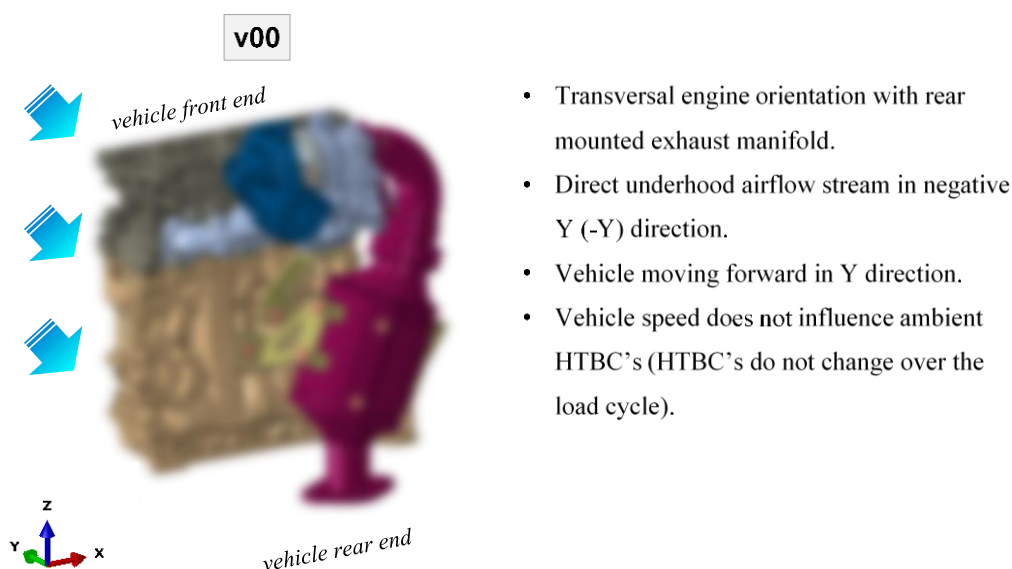

Figure 4.4. Model variant v00 installation configuration

Contrary to reference variant v00, exhaust manifold in variants v01 and v02 is at least partially exposed to the direct underhood airflow stream, which means that airflow stream velocity varies during the TMF load cycle thus influencing ambient HTBC's. This is also confirmed by the data available from 3D CFD underhood simulation reports where it is shown that underhood airflow stream velocities in front and along the sides of the engine vary significantly with each CFD load case.

4.5.1.2. Model Variant v01 – Front Mounted Exhaust Manifold

Model variant v01 represents the transversely installed engine with EM mounted in front of the engine (highly exposed to direct airflow stream), as shown in Figure 4.5.
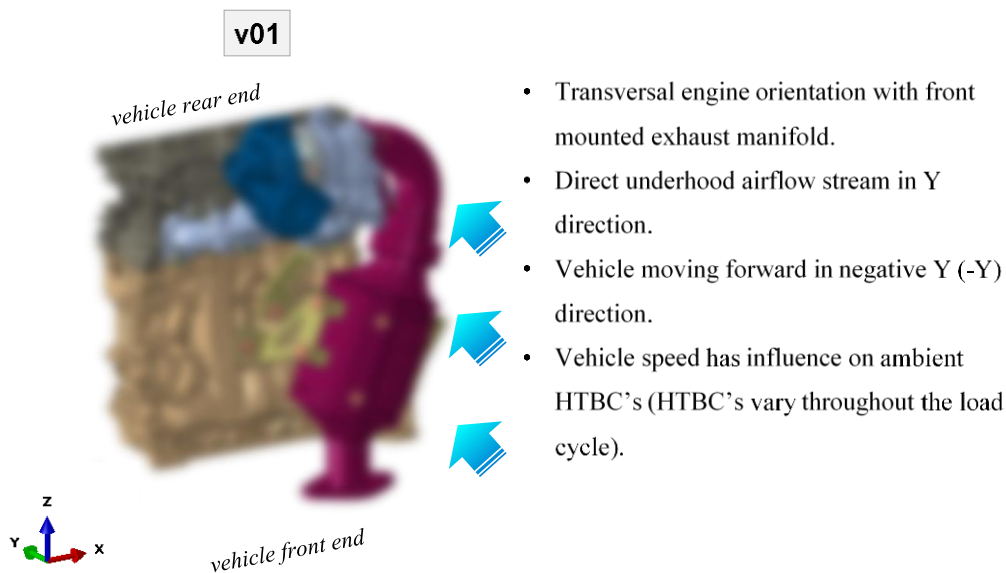

Figure 4.5. Model variant v01 installation configuration

It is clear from Figure 4.5., that the simulated "hot" (exhaust) side of the engine is highly exposed to the direct underhood airflow stream.

4.5.1.3.   Model Variant v02 – Side Mounted Exhaust Manifold

Model variant v02 represents the longitudinally installed engine with EM mounted on the side of the engine (with frontal areas highly exposed to direct airflow stream and rear areas less exposed to direct airflow stream), as shown in Figure 4.6.

- Longitudinal engine orientation with side mounted exhaust manifold.
- Direct underhood airflow stream in X direction.
- Vehicle moving forward in negative X (-X) direction.
- Vehicle speed has influence on ambient HTBC's (HTBC's vary throughout the load cycle).

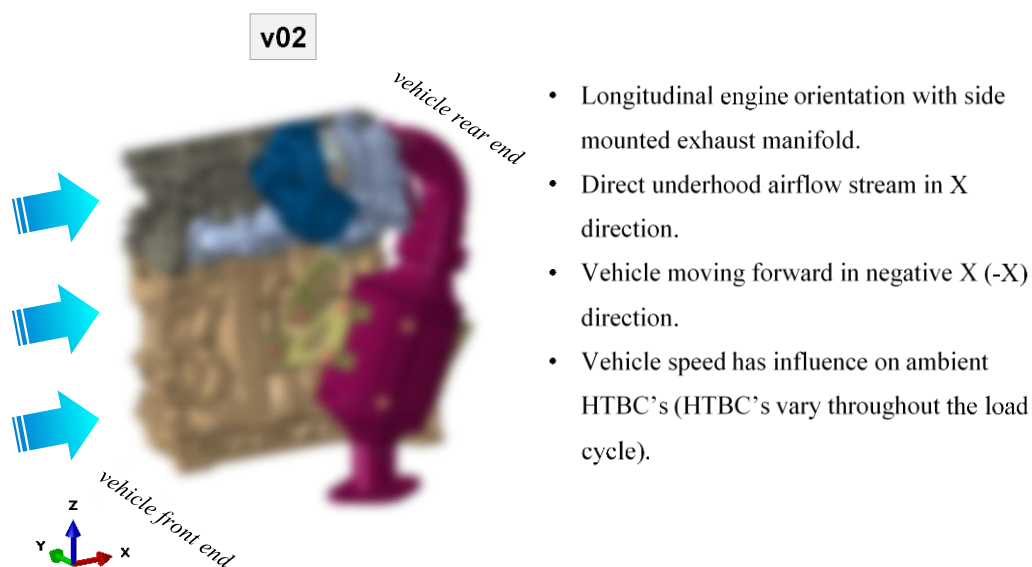**Figure 4.6. Model variant v02 installation configuration**

It can be seen from Figure 4.6. that the simulated "hot" (exhaust) side of the engine is not equally exposed to the direct underhood airflow stream. Areas located towards the front of the vehicle are more exposed to the direct underhood airflow stream, while areas towards the rear of the vehicle are less exposed to the direct underhood airflow stream.

4.6. New Ambient Thermal Boundary Conditions

As shown in Chapter 3.7.1, where steady state heat transfer problem is solved, ambient HTBC's are fully defined with only four parameters.

Two parameters for convection:

- convective heat transfer coefficient (HTC) and
- underhood airflow stream temperature for convective part of HT,

and two parameters for radiation:

- emissivity coefficient of all interacting surfaces in the engine compartment and
- temperature of the surrounding engine compartment surfaces

New ambient HTBC's, which have to simulate different model variants on the same FE model and account for different vehicle speeds throughout the TMF load cycle, are based on the 3D CFD underhood airflow simulation data provided by AVL.

3D CFD simulation data are available for three different vehicles and for various load cases. All available data is given in Table 4.7.

Table 4.7. Available 3D CFD underhood data

Available 3D CFD underhood analyses load cases and data				
Vehicle	**Engine orientation / EM mounting position**	**CFD load case / vehicle speed [km/h]**		
		Load case 1	**Load case 2**	**Load case 3**
1	Longitudinal / side mounted EM	0 (idle)	45 (8% uphill)	150
2	Transversal / rear mounted EM	40	200	/
3	Transversal / front mounted EM	40	195	/

Based on the airflow physical quantities which define the heat transfer process, provided by the reports given in Table 4.7., new ambient heat transfer boundary conditions are defined for each TMF load case and for each model variant.

The process of defining and applying new ambient HTBC's is carried out in following steps:

1. Range of convective heat transfer coefficient values on the engine ambient surface is determined from the available 3D CFD underhood simulation data for each vehicle and its simulated CFD load case.

2. Once those ranges are determined, mean value for each of range is calculated. Since the ranges were large, engine ambient surface was split into several distinct areas and average values were calculated for each of them. This ambient surface partitioning process is based on the available 3D CFD simulation data but also on the engineering common sense and the author's ability to visualize the underhood airflow.

3. Calculated values for each surface segment are adjusted for new TMF load cases and for each model variant based on the underhood airflow velocity.

4. Newly defined ambient HTBC's are applied to the corresponding ambient surface segments of the engine.

The exact values of parameters which define new ambient HTBC's are not provided because of their confidential nature.

It can only be disclosed that two out of four parameters which define ambient HTBC's are presumed to have both uniform and constant value throughout entire duration of the load cycle and for all model variants since they are not highly influenced by the engine installation configuration.

These parameters are:

1. underhood airflow stream temperature for convective part of HT,

2. emissivity coefficient of all interacting surfaces in the engine compartment.

On the contrary, temperature of the surrounding engine compartment surfaces for radiation part of HT and especially the ambient convective heat transfer coefficient (HTC) are parameters which are influenced by engine installation configuration.

Applied HTC's on all engine surfaces in thermal interaction with their surrounding (ambient surfaces) are visualised in Figure 4.7. with uniform colour scale for the whole figure.
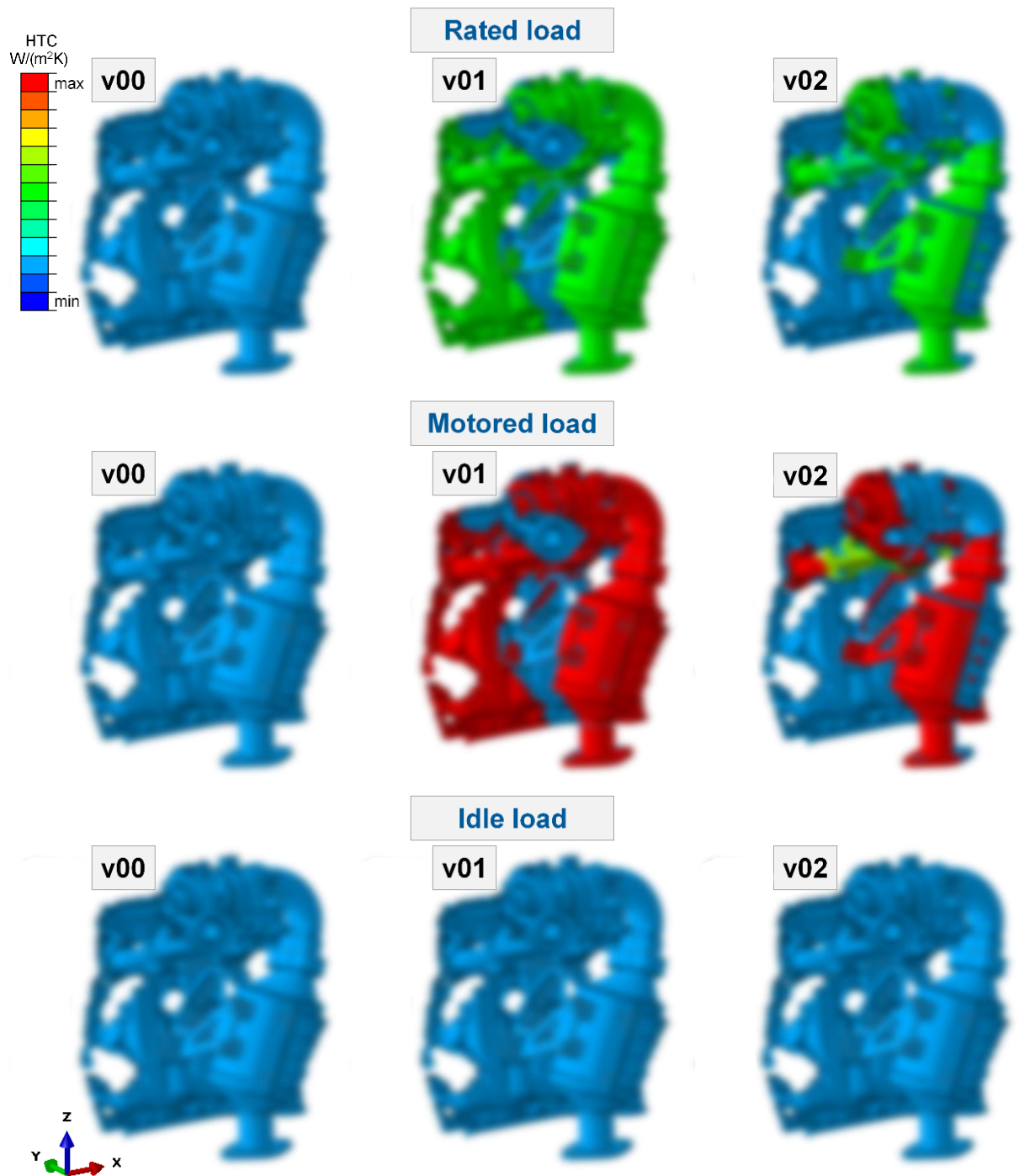
Figure 4.7. Newly defined and applied HTC's for all load cases and model variants

Figure 4.7. summary:

- variant v00 has the same intensity of convective HTBC's applied for all load cases,

- variant v01 has generally the highest intensity convective HTBC's applied,

- the most intense convective HTBC's are generally applied during the motored load,

- during the idle load, convective ambient HTBC's applied have the lowest and almost identical intensity across all variants (only minor differences exist).

5. Results

It should be noted that (almost) all results shown are only results of the last (stabilized) simulated cycle because only this cycle is relevant for the subsequent fatigue life evaluation analyses.

Also, most of the evaluated results concern the exhaust manifold only. The reason is that the final step of this thesis investigation, evaluation of the TMF life, is carried out only for this component.

As already said, model variant v00 was simulated in accordance with the current (April 2017) AVL TMF workflow so it serves as a reference point and all analyses results are compared against it.

Another important note to remember is that all figures showing the simulated models or any parts of them are property of AVL. They are blurred and distorted on purpose due to confidentiality reasons.

5.1. Heat Transfer Analyses

5.1.1. Steady State Heat Transfer Analyses

Steady state heat transfer analyses for all three model variants were performed.
Main purpose of those analyses was to determine whether the number of simulated load cycles and the duration of each load case were correctly defined.

Another advantage of running steady state HT analysis is to because it represents a relatively quick way (much quicker than running transient HT analysis) to verify if the analysis computational parameters (model definition, applied loads and boundary conditions, analysis input file, external files, etc.) are correctly set up.

Load cycle definition verification process can be divided into following steps:

1. The maximum steady state analysis temperature location at the end of rated load is found on the outer (ambient) gas surface of the exhaust manifold for each model variant.

2. The transient analysis temperature for this same location, also at the end of rated load, is compared against the steady state analysis temperature.

3. First criteria requires that maximum transient temperature in the last load cycle reaches at least 95% of the maximum ambient steady state temperature at the EM.

4. Second condition is that temperatures at the beginning and at the end of the last simulated load cycle for the previously determined location on the EM should be nearly identical, i.e. the last cycle should be stabilized.

5. Full metal temperature stabilization at the CH exhaust valve bridge and at the CH coolant (water) intake during each load cycle should be achieved which ensures that duration of each individual load case is correctly defined.

5.1.2. Transient Heat Transfer Analyses

Both the number of simulated load cycles and the duration of individual load cases turned out to be correctly defined based on all the criteria laid out in the (previous) Chapter 5.1.1.

Temperature history plot for variant v00, across all load cycles, is shown in Figure 5.1.
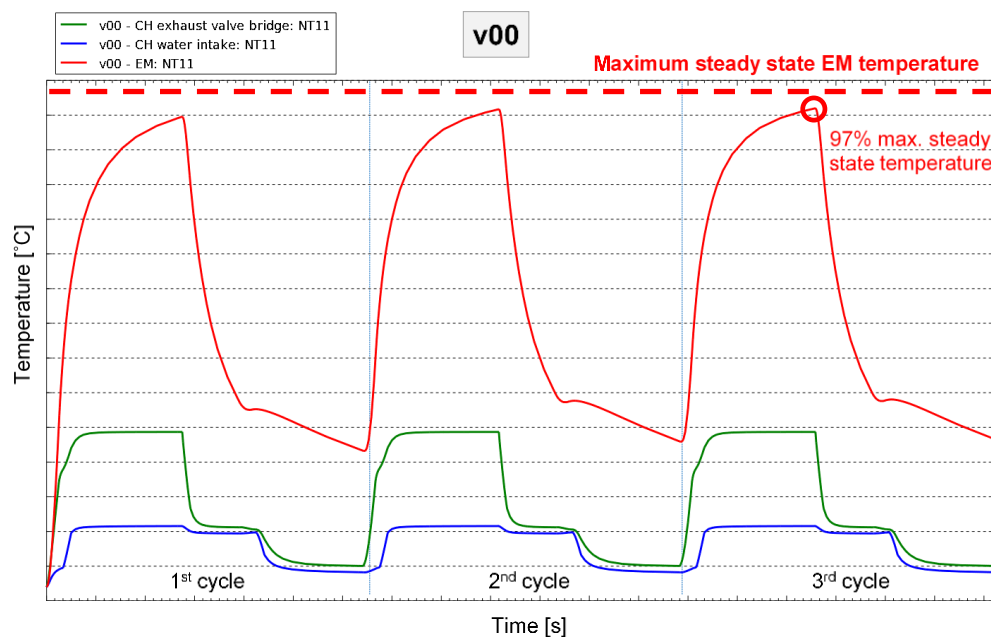

Figure 5.1. Temperature history plot for variant v00

Temperature history plots for other two variants will not be shown or discussed in much detail because they are qualitatively very similar.

Every statement written below applies to all three model variants.

Transient temperature reached 97% of the steady state maximum temperature found on the outer surface of EM at the end of rated load, which means that this criteria is satisfied (all variants reached 97%).

As can be seen in Figure 5.1., there is no noticeable difference between temperatures reached at the beginning and at the end of the last cycle meaning that this cycle is stabilized. It can also be seen that full metal temperature stabilization at the CH exhaust valve bridge is achieved.

This means that durations of individual load cases and total load cycle time duration for all three variants are correctly defined.

5.1.3. Structural Temperature Distribution

As already said, because temperature history plots are qualitatively very similar across all three variants, only the one for variant v00 was shown.
Nonetheless, temperature history plots for all simulated variants were carefully compared with each other and the following observations were made:

- variant v00 has the highest maximum temperature values found on the EM outer surface in both steady state and transient HT analyses,
- variant v01 has the lowest maximum temperature values found on the EM outer surface in both steady state and transient HT analyses,
- maximum temperatures found on the EM outer surface in both steady state and transient HT analyses in variant v02 sit somewhere between the those found in v00 and v01.

Based on the temperature evaluation at this single location on the EM, it can be presumed that reference variant v00 is the hottest variant and v01 is the coolest variant.

Transient HT transfer analyses results which will be presented in the remainder of this chapter will confirm this presumption.

Temperature distribution at the end of rated load on the whole simulated FE models is shown in Figure 5.2.

The influence of applied ambient HTBC's is clearly visible in this figure.

Ambient surface areas inside magenta dotted circles are highly affected by the ambient HTBC's variation.

It is clear that surface segments to which higher intensity ambient HTBC's are applied (due to the airflow stream velocity magnitude and direction) behave as expected, i.e. they are cooler.
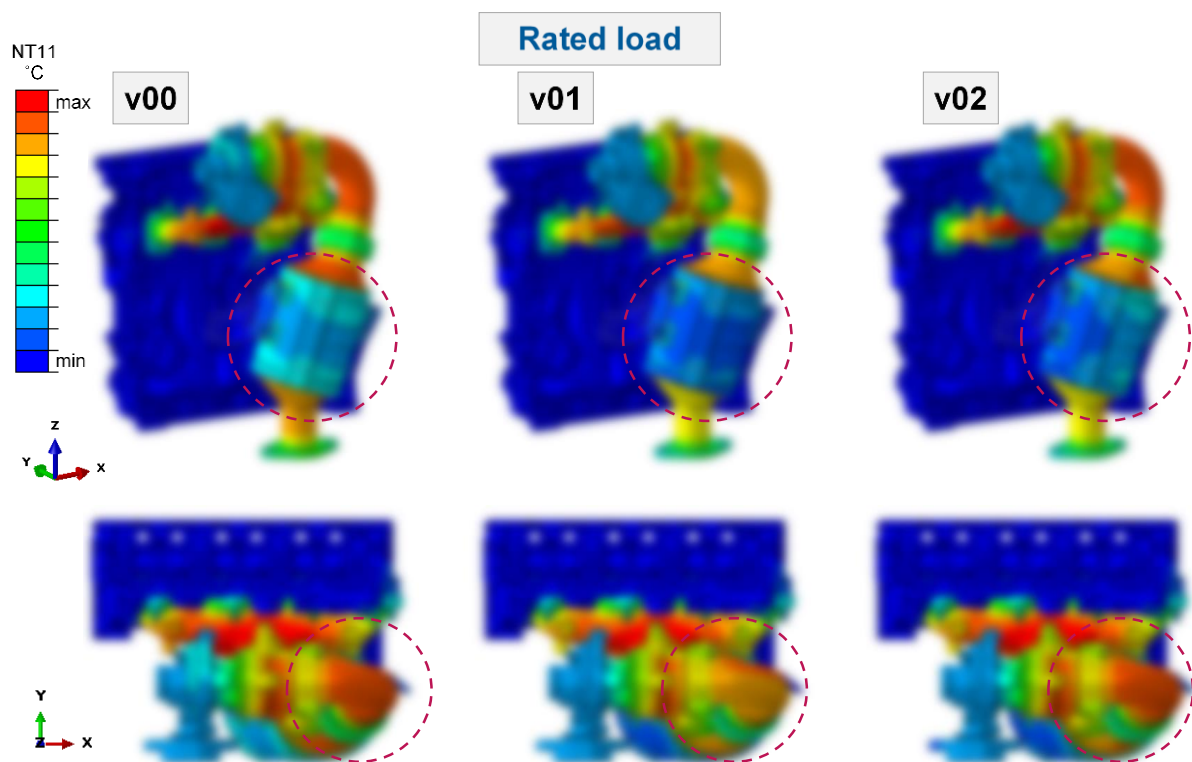

Figure 5.2. Temperature distribution on the whole simulated FE models

The same effect is also visible throughout the entire duration of the heat transfer analyses.

This proves that the engine orientation and EM mounting position influence structural temperature distribution and that this effect is correctly modelled in all three simulated model variants.

Figure 5.3. shows EM temperature distribution at the end of rated load for all three variants.
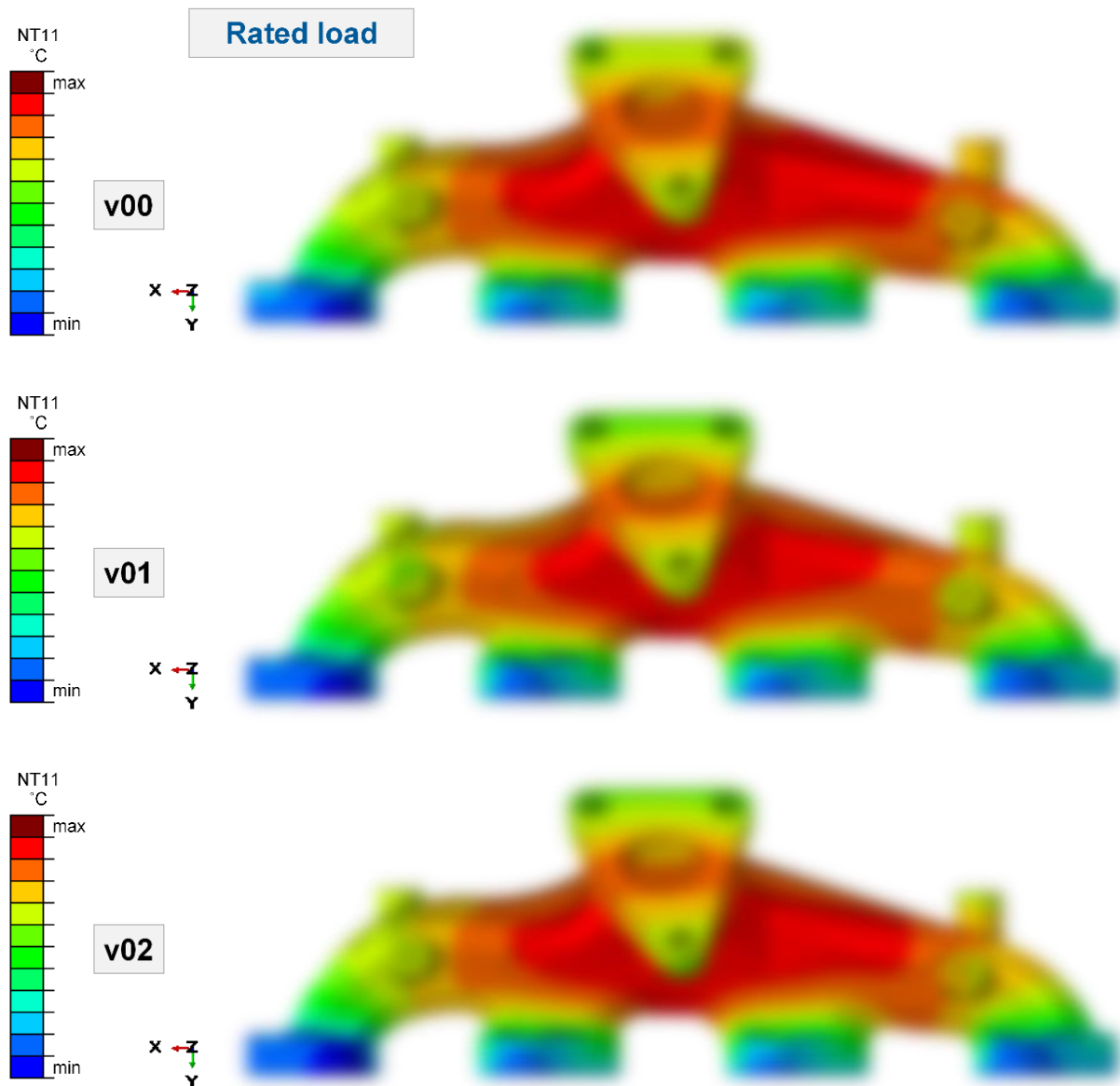It should be noted that the colour scales shown in Figure 5.3. are the same across all variants.

Figure 5.3. Temperature field at the end of rated load for all variants

It can be seen that v00 is generally the hottest one, with the highest temperatures.

On the contrary, v01 is generally the coolest one, with the lowest temperatures.

Temperatures found in v02 are generally somewhere in between, but also a bit closer to the hotter reference variant v00 than to cooler v01 variant.

Similar temperature distribution differences can be recognized at the end of both motored and idle loads which are shown respectively in Figure 5.4. and Figure 5.5.

It should be noted that colour scales are different for each load case, but they remain uniform across all variants shown on the same figure.
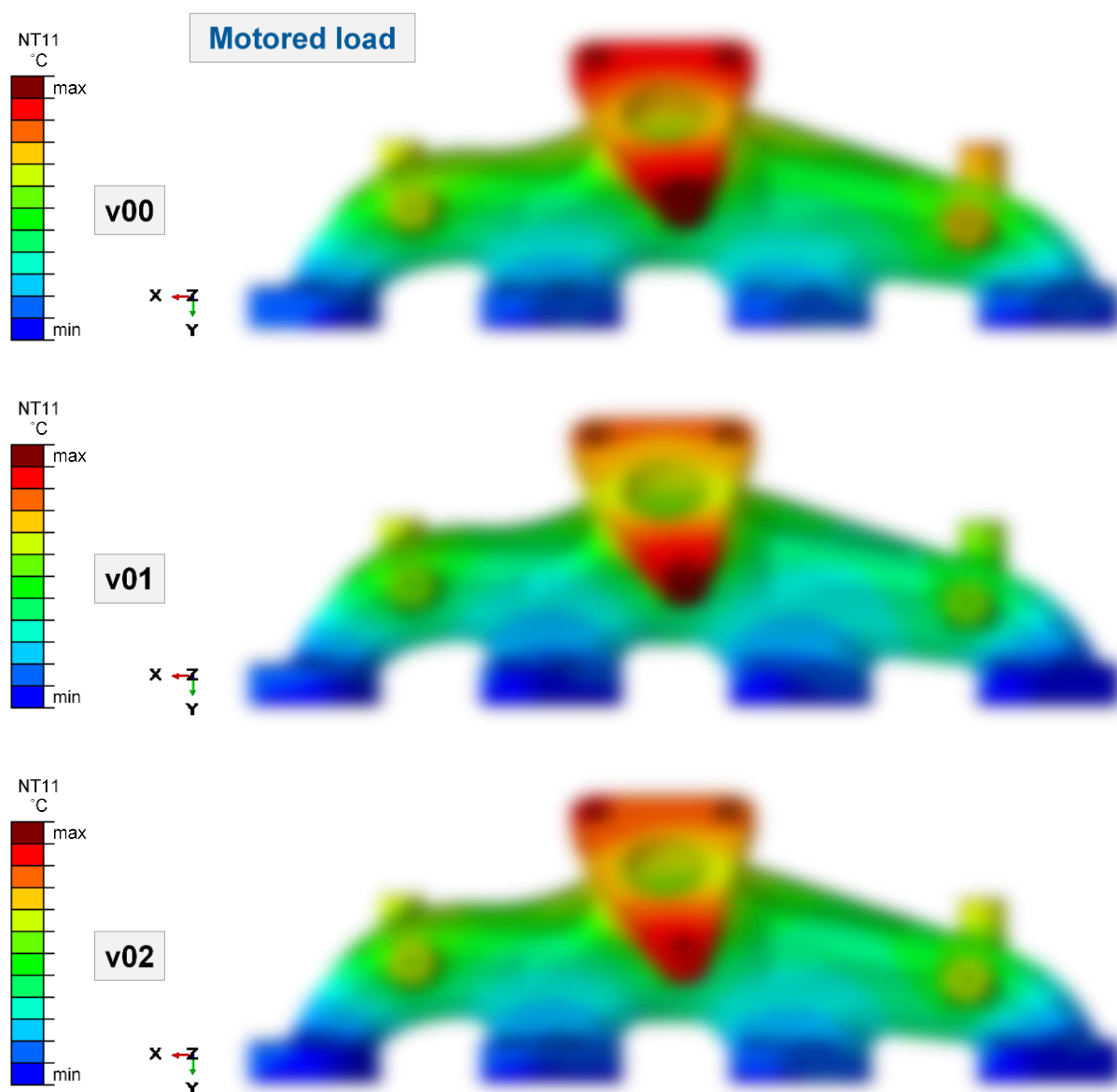

Figure 5.4. Temperature field at the end of motored load for all variants

From Figure 5.4. it can also be seen that at the end of motored load turbocharger flange remained the hottest parts of the EM for all variants. This is the effect of thermal inertia which is more obvious on thicker components just like this flange.

This effect is also visible at the end of the idle load, where TC flange remained the hottest part of EM in all three variants as shown in Figure 5.5.
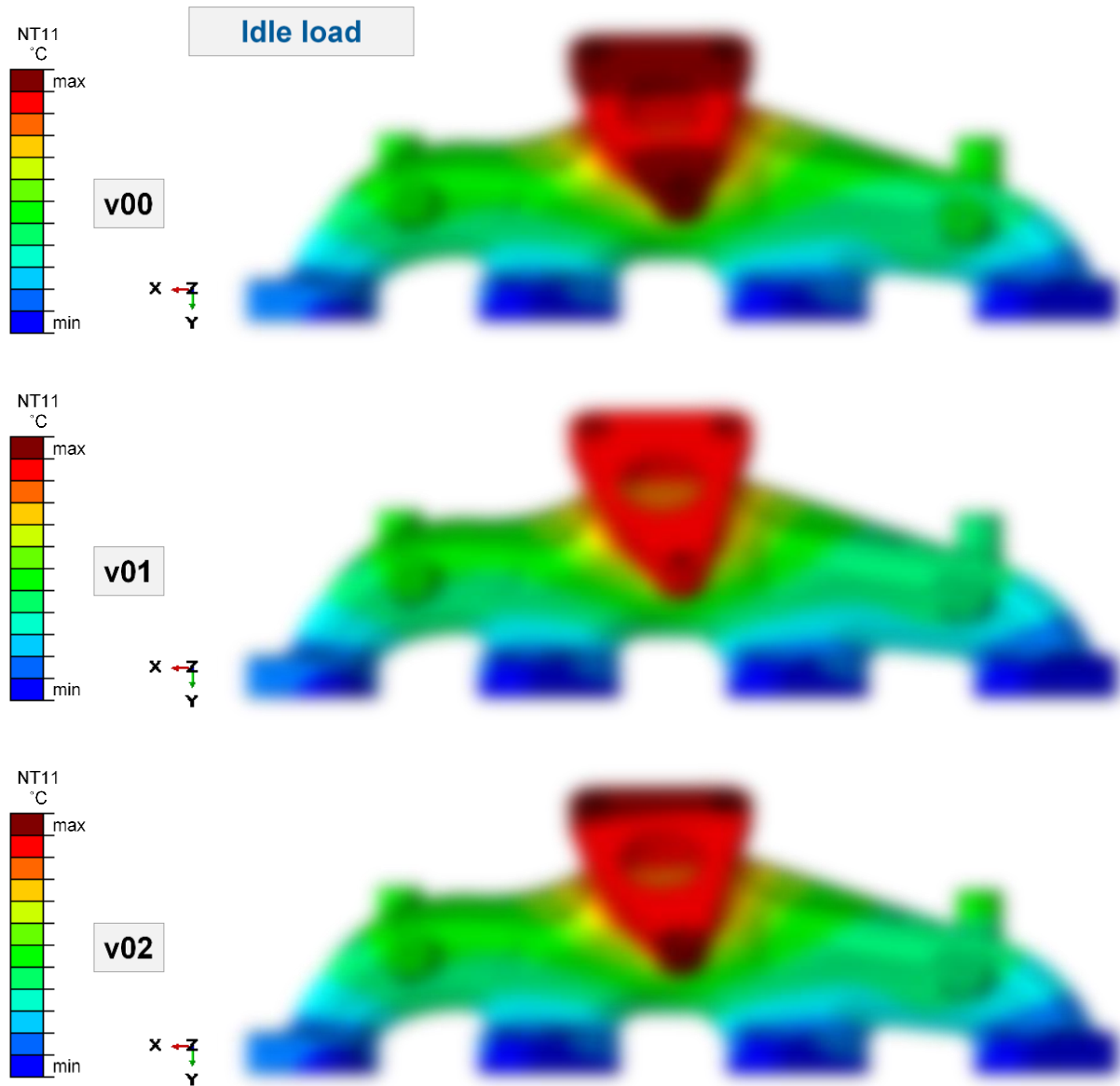
Figure 5.5. Temperature field at the end of idle load for all variants

In order to highlight the magnitude of structural temperature differences between model variants, Figure 5.6., Figure 5.7. and Figure 5.8. are created.

In those figures, absolute temperature distribution is shown on the reference model variant while the remaining two variants show only the temperature difference when compared against the reference variant.

Temperature differences for v01 and v02 are calculated as

$$\Delta T_{v0i} = T_{v0i} - T_{v00} \; [\degree C] \qquad i = 1, 2 \, . \tag{5.1}$$
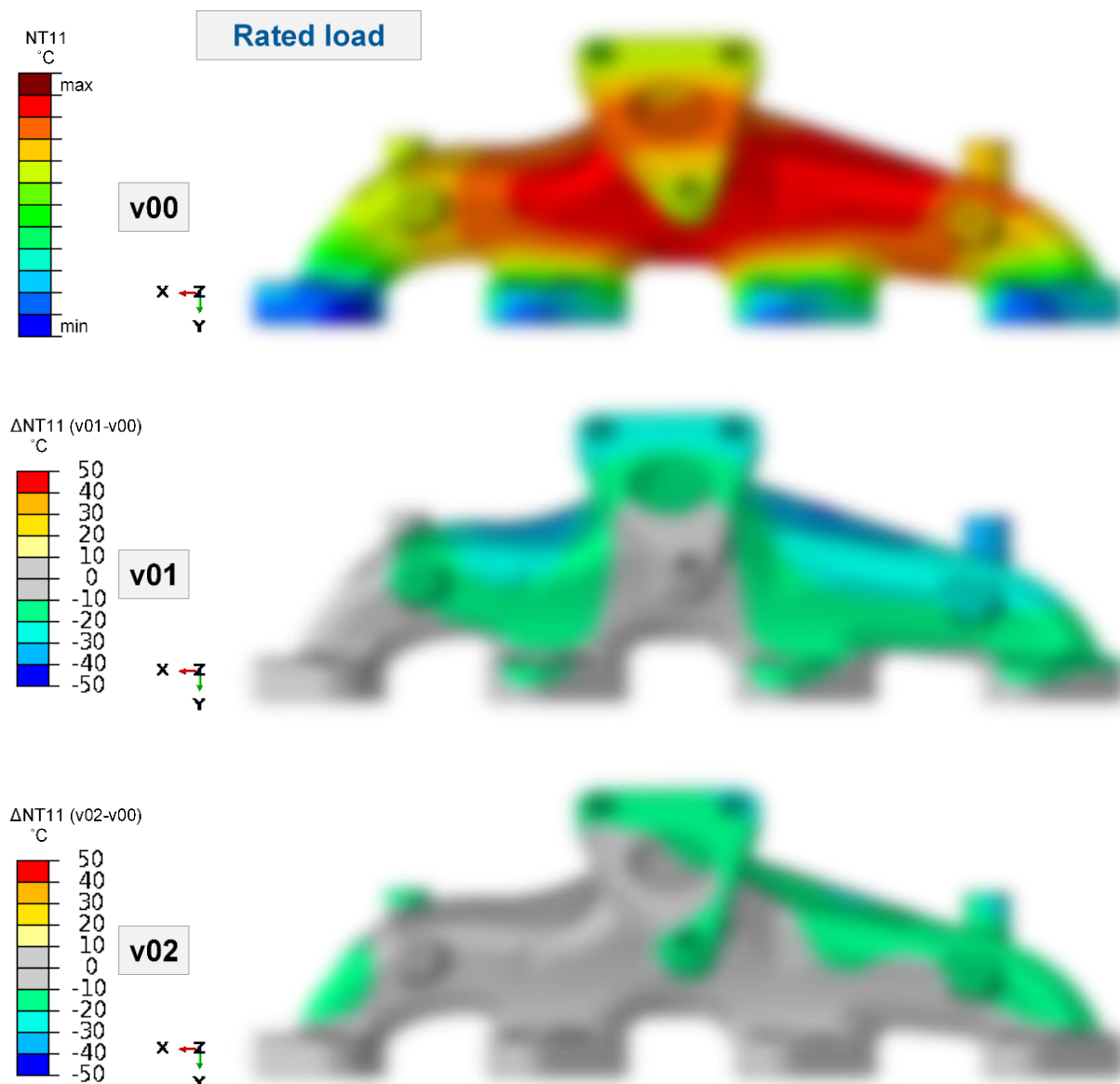
Figure 5.6. Temperature distribution differences across variants at the end of rated load

At the end of rated load, those differences range between -1 ˚C and -41 ˚C for variant v01, and +1 ˚C and -25 ˚C for v02.

The effect of similar HTBC's applied to some ambient surface segments for across variants is evident under TC flange in variant v01, and on the "shadowed" side of TC flange in variant v02 where temperature differences are small (less than ±10 ˚C).

EM flanges to CH and areas around them do not exhibit large temperature differences. This is due to their direct contact with CH, which has greater influence on temperatures in those areas than applied ambient HTBC's.

Figure 5.7. Temperature distribution differences across variants at the end of motored load

At the end of motored load, temperature differences range between -3 ˚C and -77 ˚C for variant v01, and -1 ˚C and -47 ˚C for v02.

Temperature differences are the largest at the end of the motored load because during this loading condition variation of applied ambient HTBC's is the highest.

Areas to which similar ambient HTBC's are applied again show small temperature differences (under TC flange in variant v01, and on the "shadowed" side of TC flange in variant v02).
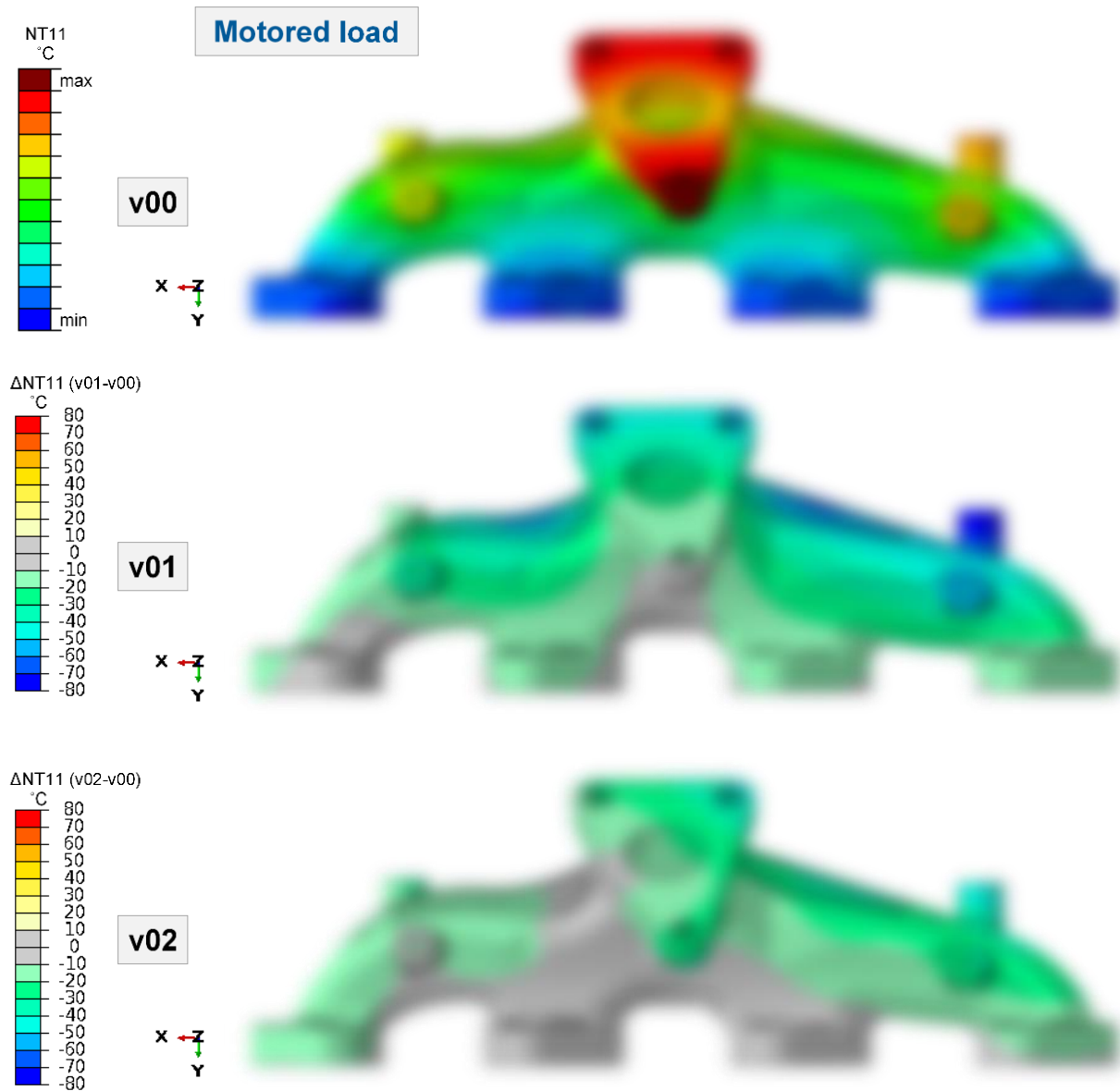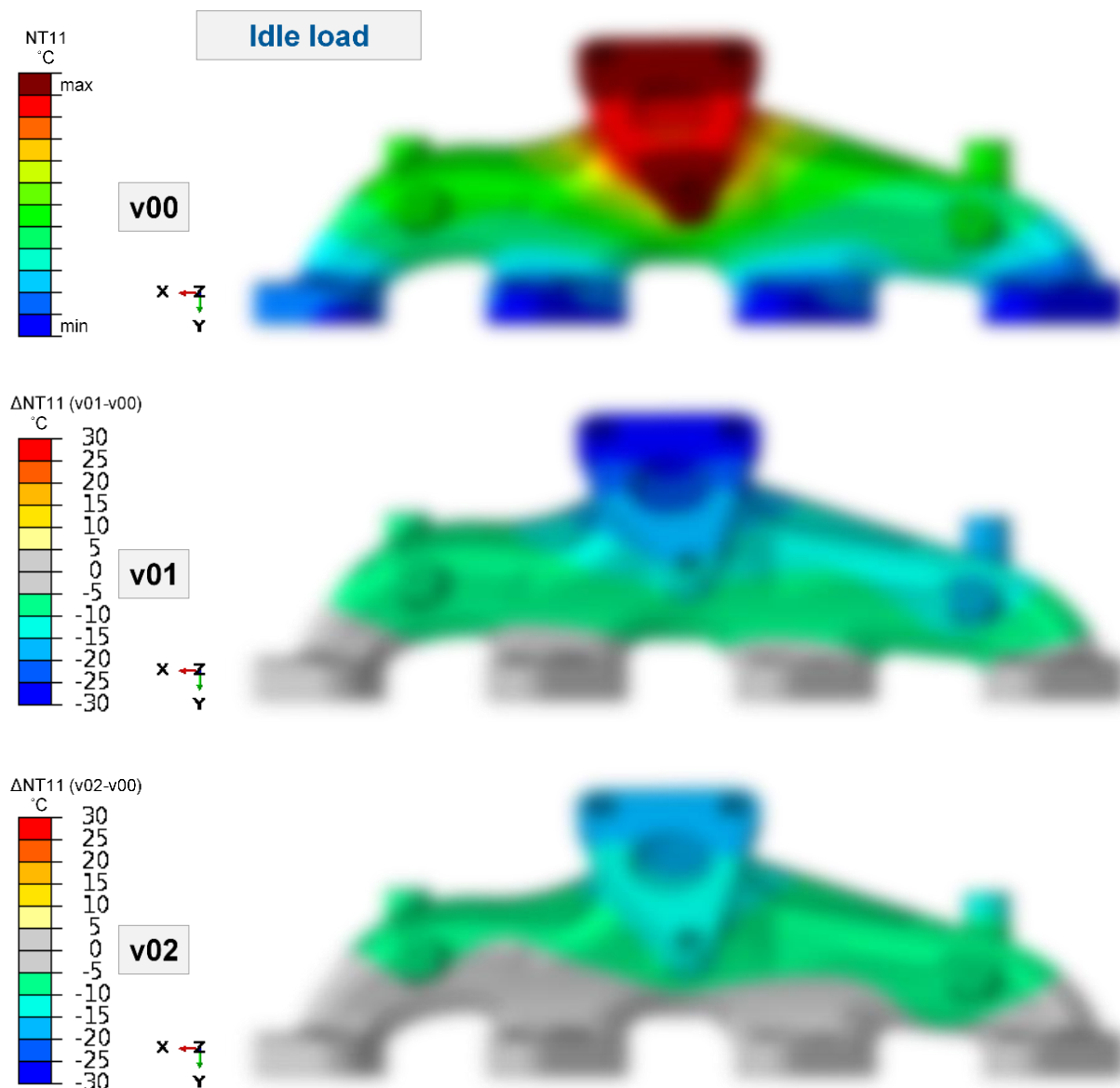
Figure 5.8. Temperature distribution differences across variants at the end of idle load

At the end of idle load, temperature differences range between -1 °C and -28 °C for variant v01, and -1 °C and -20 °C for v02.

Differences are the lowest on flanges to CH and the highest on the TC flange.

Temperature differences at the end of idle load are caused by different temperature levels at the end of motored load and not by the applied ambient HTBC's.

This is because applied ambient HTBC's during the idle load are nearly identical for all three variants.

In conclusion of the heat transfer analyses results evaluation, the following can be said:

- temperature distribution is in line with the applied ambient HTBC's across all variants,

- rear mounted EM reference variant v00 is generally the hottest,

- front mounted EM variant v01 is generally the coolest and shows the highest temperature differences when compared to reference variant v00,

- side mounter EM variant v02 is generally cooler than the reference variant v00 and it shows temperature differences which are smaller than the ones found in v01,

- the largest temperature differences occur during the motored load as expected (because applied ambient HTBC's also differ the most during this load),

- temperature differences at the end of idle load are noticeable, but they are almost entirely consequence of differences in temperature levels found at the end of the motored load.

5.2. Nonlinear Stress-Strain and Fatigue Life Prediction Analyses

It should be noted that colour scales across all variants shown on the same figure are identical.

5.2.1. Nonlinear Stress-Strain Analyses Results
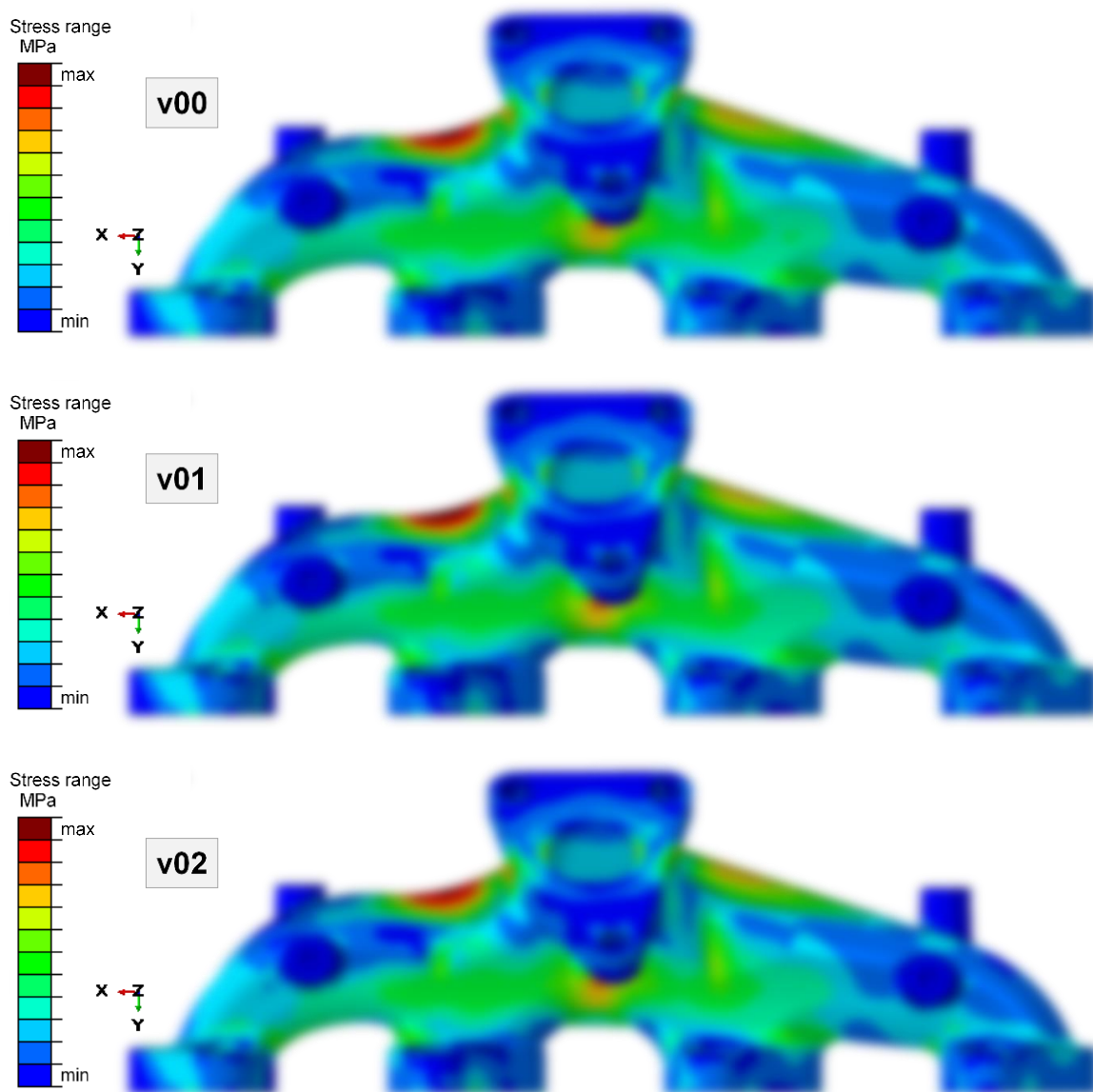
Figure 5.9. EM stress range

Stress range distribution across EM surface is identical for all three variants.

Slight differences between variants can be noticed in overall stress level and at peak stress values.
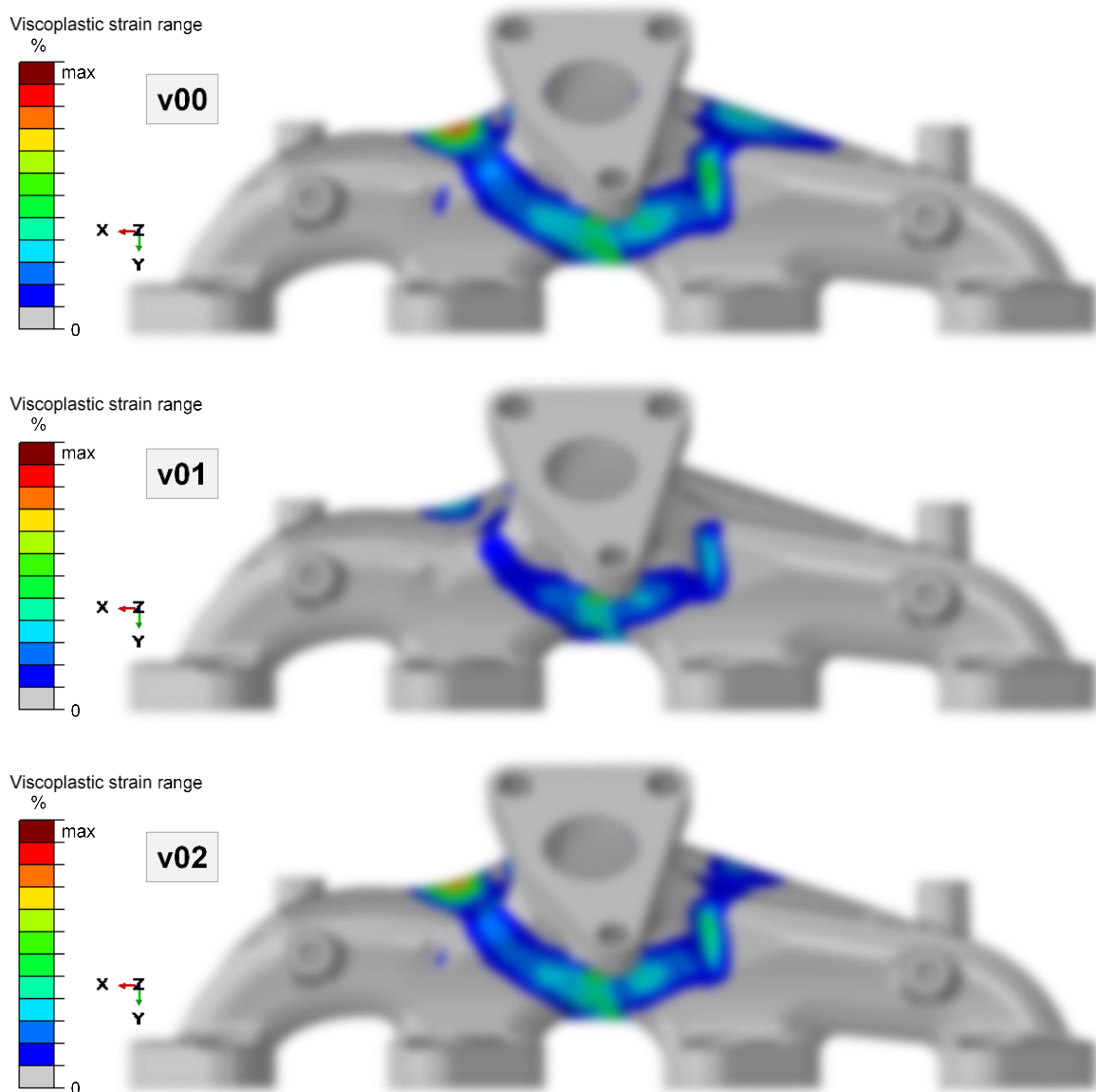
Figure 5.10. EM viscoplastic strain range

Similar to the stress range, the viscoplastic strain range distribution is similar for all three variants.

On the other hand, differences in the levels of strain range are more noticeable between variants. Generally, the lowest viscoplastic strain range is found in variant v01 (the coolest one) while the highest viscoplastic strain range is found in v00 (the hottest one).

Locations with maximum viscoplastic strain range in all variants are on both stiffening ribs near the flange to turbocharger (not clearly visible on the shown figure).
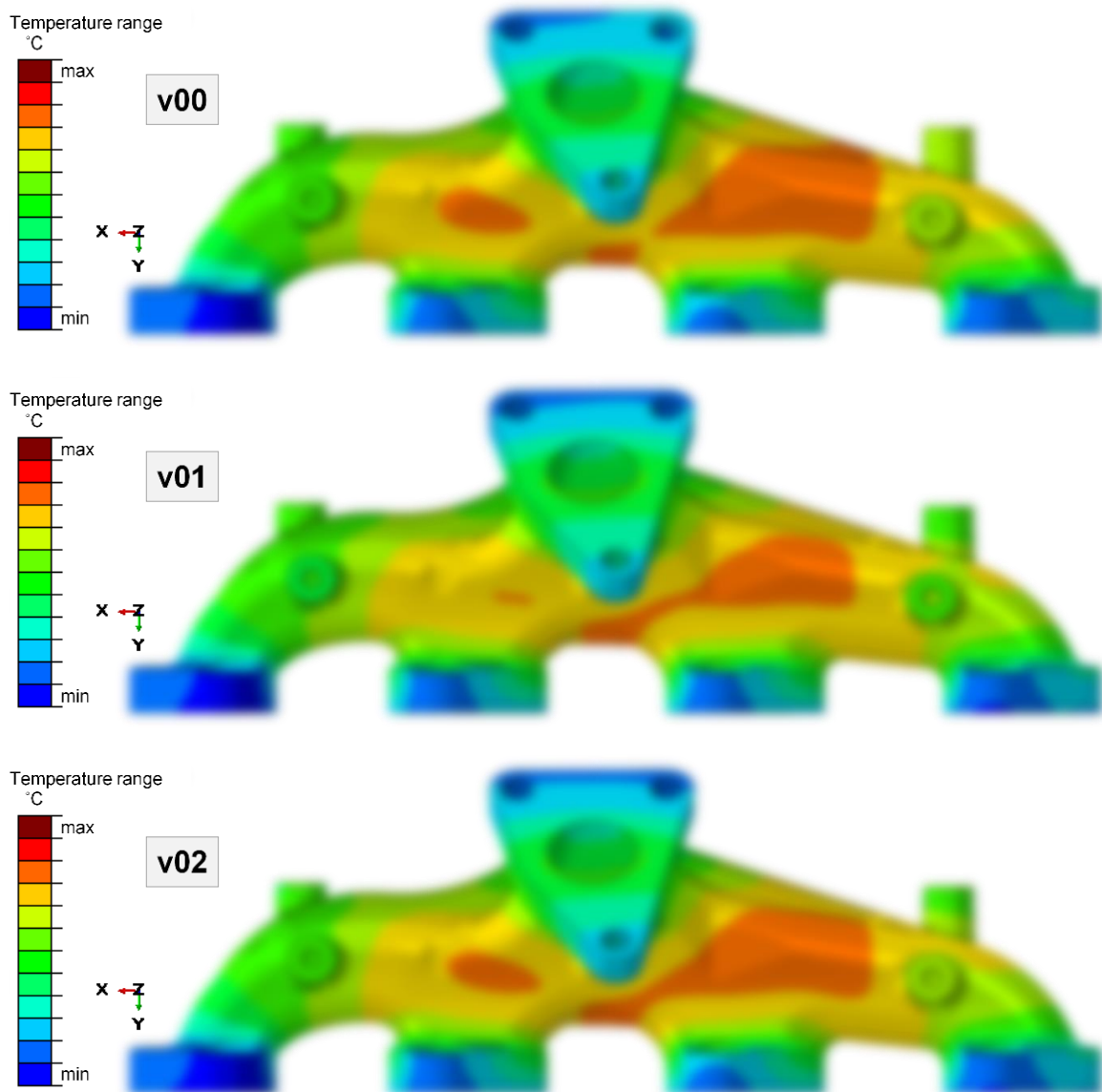
Figure 5.11. EM temperature range

Temperature range distribution is similar for all three variants.

More noticeable differences between variants can be seen at areas at which applied ambient HTC's vary significantly (as expected).

Generally, temperature ranges are the highest in v00 of while they are the lowest in variant v01.

Even though, temperature range value as such is not used as a damage model parameter, it shows that both maximum and minimum temperatures during the last (stabilized) cycle are known. Knowing these two temperatures, average temperature can be calculated.

This means that all parameters which define the damage model are now calculated.

5.2.2. Fatigue Life Evaluation

Once nonlinear stress-strain analyses data required for the TMF life prediction are calculated, the fatigue life can be estimated using the damage model given by Equation (4.1).

TMF fatigue life limit for this case is set to 3000 cycles. Any potential area with predicted TMF life of less than 3000 cycles is considered critical, i.e. non-satisfactory.

All critical areas for each variant are shown in Figure 5.12., Figure 5.13. and Figure 5.14.
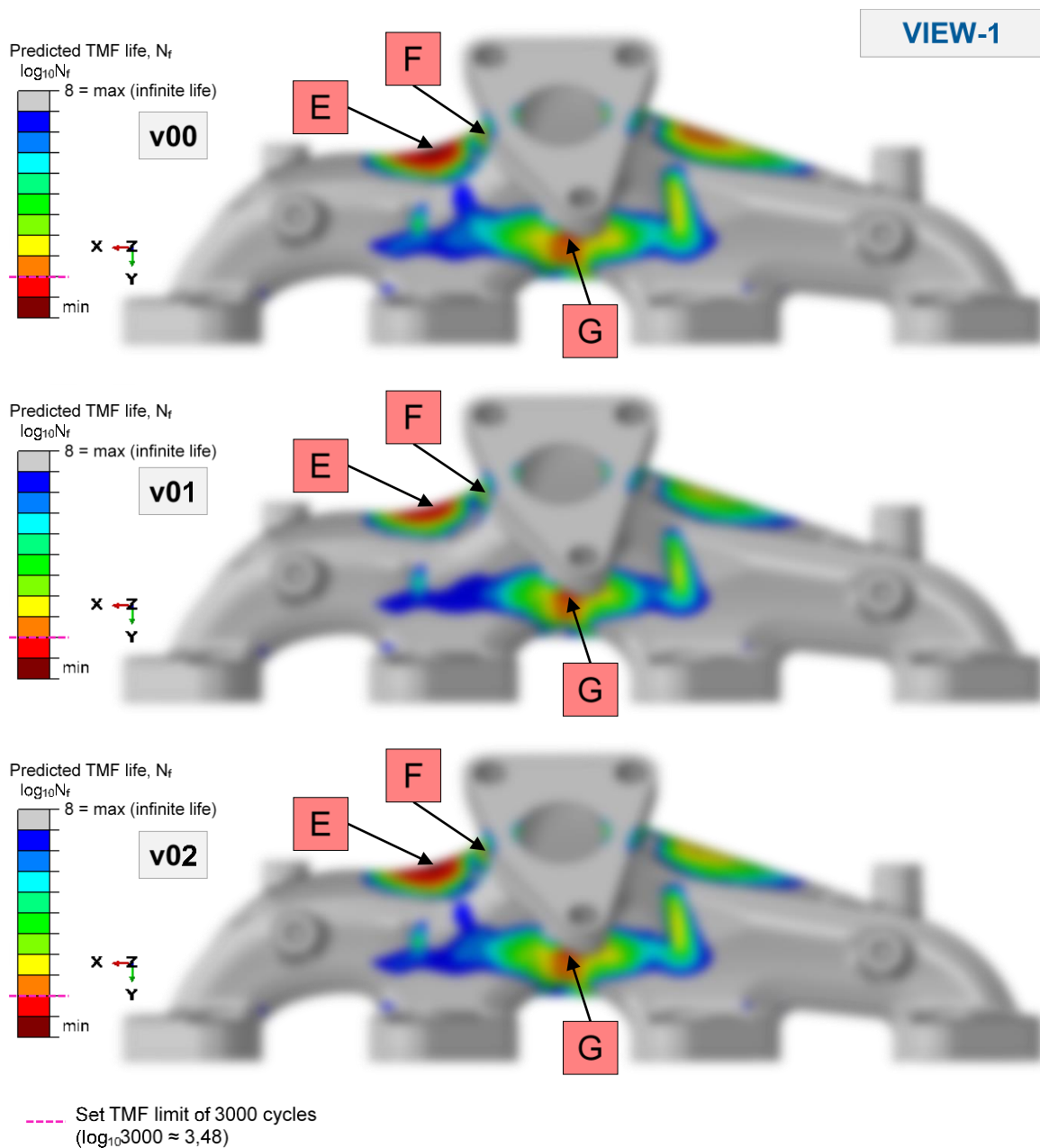
Figure 5.12. EM predicted TMF life, N_f - view-1

Three critical areas can be seen for all three variants in Figure 5.12.

Figure 5.13. shows EM in view-2 (rotated for 180˚ around the Y-axis from view-1). In this figure, two more critical areas can be seen for all three variants.
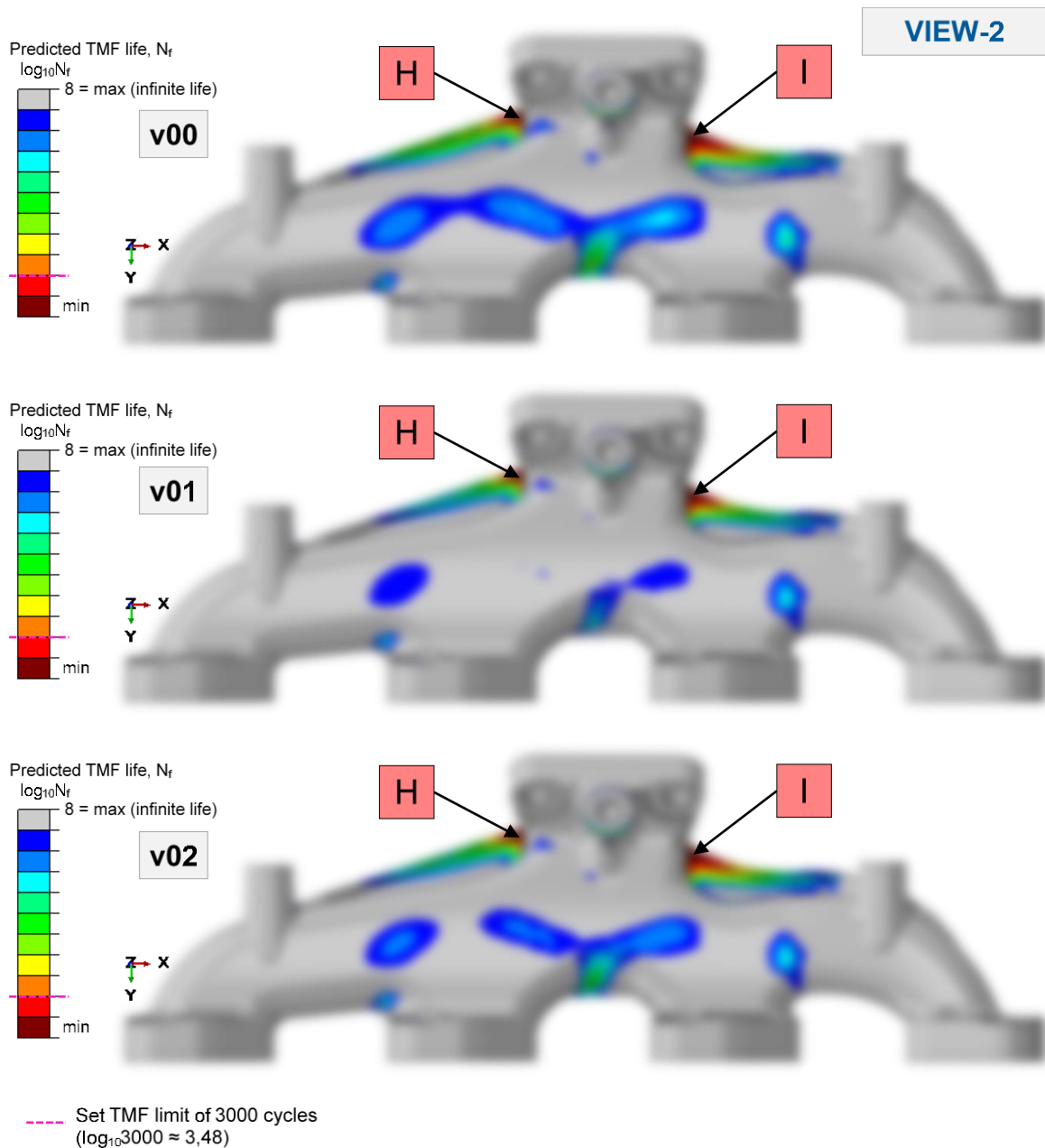
Figure 5.13. EM predicted TMF life, N_f - view-2

Figure 5.14. shows the EM oriented and positioned in the same way as in Figure 5.13. but now with applied Z-plane cut exposing the inner (gas) surface of the EM.

One critical area can be seen on the inner EM surface for all three variants.
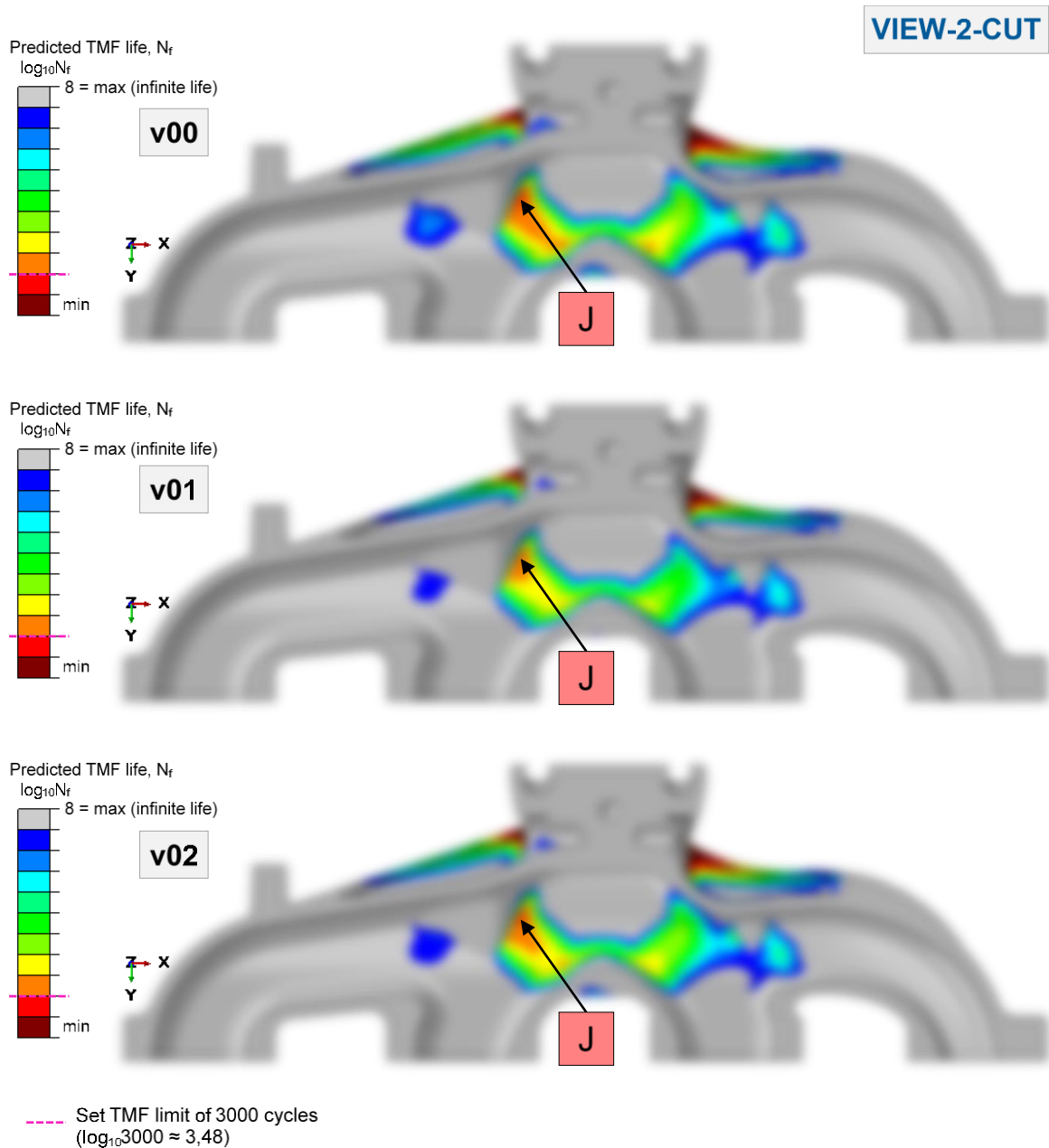
Figure 5.14. EM predicted TMF life, N_f - view-2-cut

The first conclusion which can be drawn by looking at all figures showing critical locations is that each variant shows 6 critical areas on EM.

The locations of those 6 critical areas match between variants, which means that damage mechanism remained the same for all three simulated model variants.

For each critical location, a set of hysteresis plots shown in Figure 5.15. is generated.
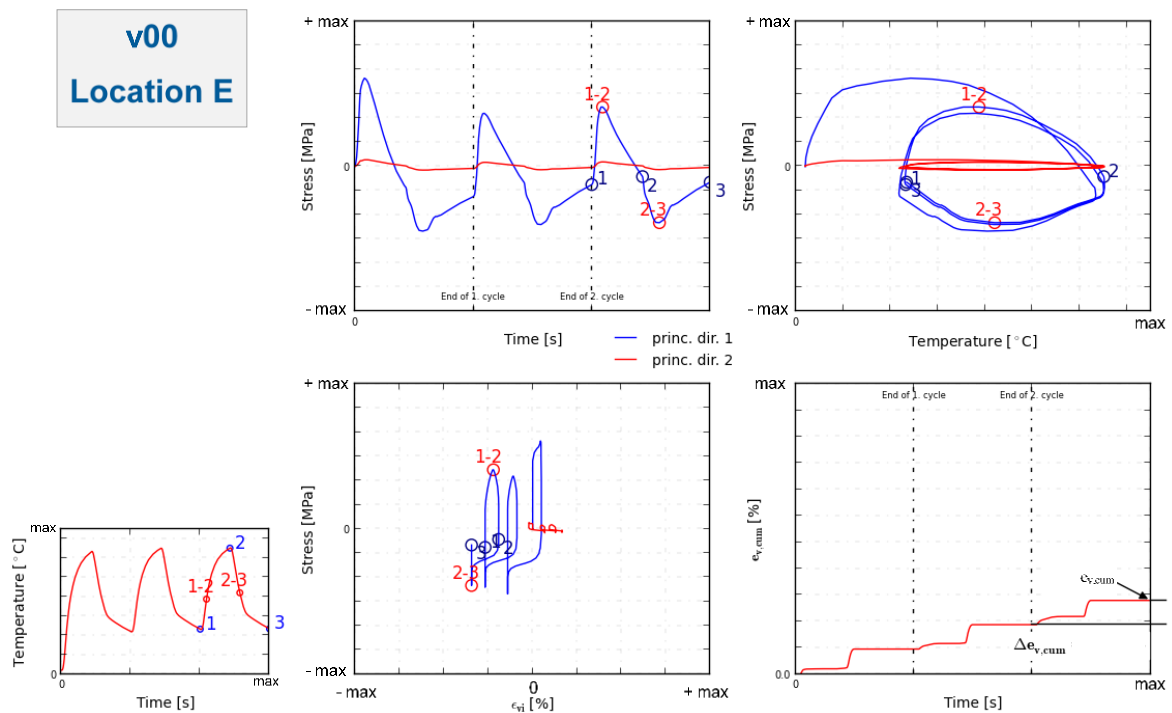
Figure 5.15. Variant v00, critical location E hysteresis plots

One thing which is clear from the set of plots shown in Figure 5.15., is that stress state at location E is almost uniaxial.

Another important observation is that time points at which temperature and stress extremes occur do not coincide.

Extreme stress values are found during the heating and cooling period. To be more precise they are found when temperature gradients are the highest. This means that temperature gradients highly influence the stress levels (and consequentially the predicted TMF life).

On the other hand, the highest increase of accumulated viscoplastic strain happens when temperature level is also the highest. This is the result of exhaust manifold temperature dependent material properties, i.e. elastic modulus decreases with temperature increase.

All these statements, except the one about uniaxial stress state are also true for all other critical locations found across all three variants. Plot sets for the same location across all variants are qualitatively very similar.

Because there is a total of 18 generated hysteresis plot sets (one for each critical location and for each model variant) only the set for v00 at location E will be shown.

In the remainder of this chapter, a comparison of characteristic data calculated at all critical locations between all variants is made.

It should be noted that relative differences are calculated with respect to reference model variant v00 and expressed as percentages.

First, a comparison of calculated TMF life is shown in Figure 5.16.
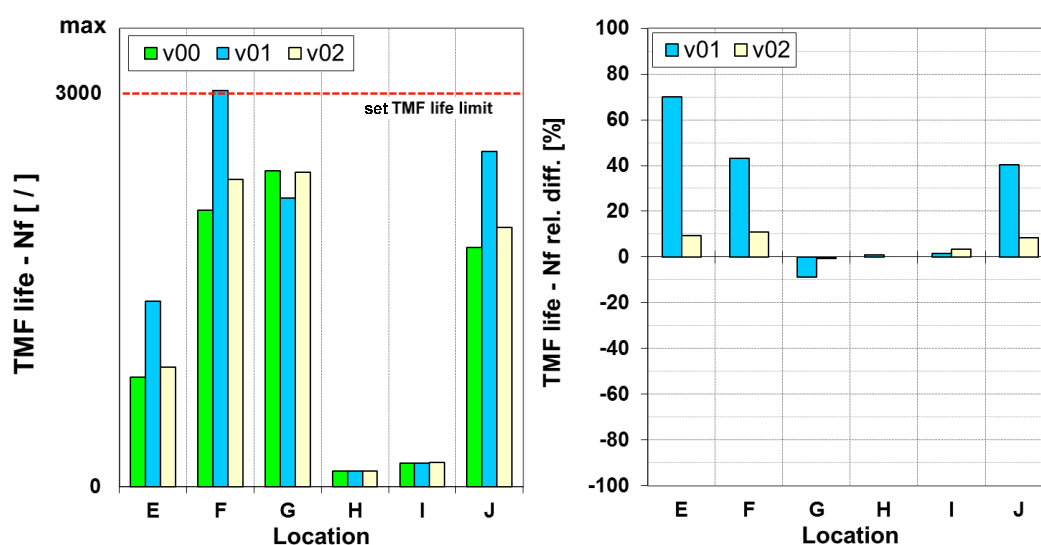
Figure 5.16. Critical locations data comparison - calculated TMF life

It can be noticed from Figure 5.16. that variant v01 shows the longest predicted TMF life at all critical locations except at location G.

Relative differences between variants v00 and v01 are significant and they range up to 70% while those between v00 and v02 with maximum value of 11%.

At locations E, F and J variant v01 shows much longer predicted TMF life than reference variant v00. These differences are 70%, 43% and 40% for E, F and J locations respectively. Variant v01 even predicts TMF life at location F which is just above the limit of 3000 cycles (although by only small number of cycles).

Locations H and I, with the lowest predicted number of cycles, remained "immune" to variation of ambient HTBC's showing neither improvement nor worsening of predicted number of cycles until crack initiation.

At location G, it can be seen that generally the coolest variant v01 shows predicted TMF life which is lower than the one calculated in v00. Total TMF life reduction is 209 cycle which is a relative difference of 9%.

Figure 5.17. shows the stress ranges occurring at the critical locations during the last (stabilized) simulated cycle.
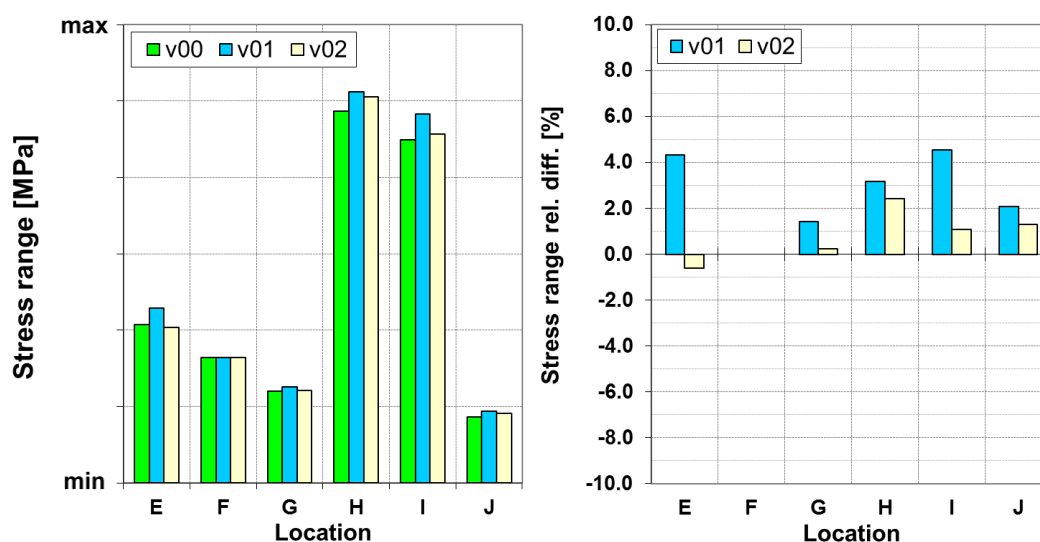
Figure 5.17. Critical locations data comparison - stress range

Relative differences of stress ranges between all variants, shown in Figure 5.17., are much lower than relative differences of predicted TMF life. Larger relative differences are found for v01 but they are all lower than 5%.

Differences between v00 and v02 are also noticeable, but they are not as large as those between v00 and v01.

It can be seen that stress ranges are the highest for v01 at all locations (except at location F where they are identical for all variants). The fact that EM material properties are modelled as temperature dependent explains this because with temperature decrease material becames stiffer, meaning that the stress generated for the same level of strain is higher.

Another interesting thing which can be concluded is that stress ranges at locations with the lowest predicted TMF life are much higher than at other critical locations.

Figure 5.18. shows comparison of viscoplastic strain range at all critical locations.

94
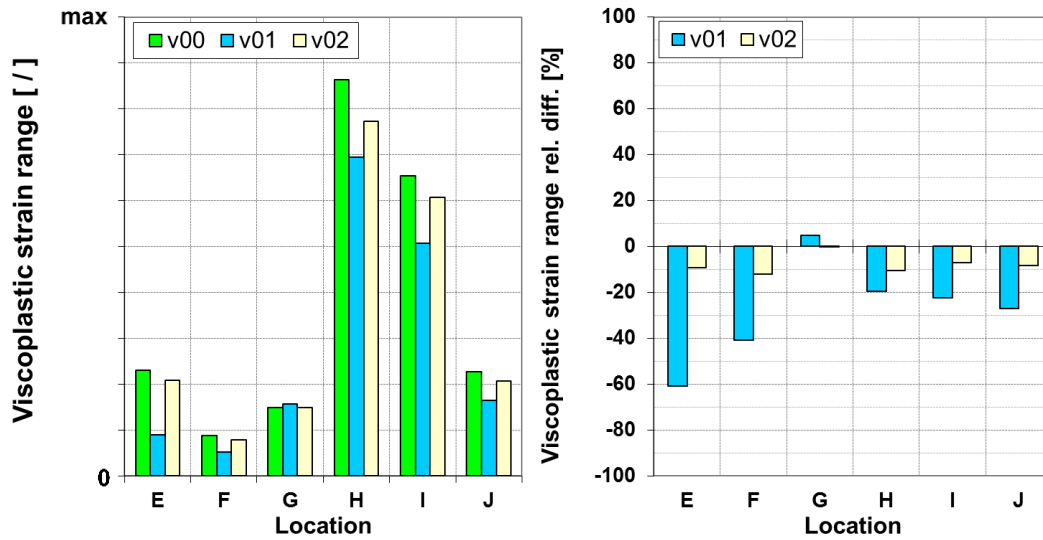
Figure 5.18. Critical locations data comparison - viscoplastic strain range

Viscoplastic strain ranges, depicted in Figure 5.18., show significant relative differences between variants v00 and v01 of up to 61%.

Differences between v00 and v02 are also noticeable (up to 12%), but they are not as nearly as large as those between v00 and v01.

It can be noticed that variant v01 shows much lower viscoplastic strain range at all locations except at location G. Only at this location v01 shows the highest viscoplastic strain value.

As was the case with stress range, locations H an I show viscoplastic strain values which are much higher (up to 4 times) than the ones found at any other location.

Maximum temperatures, which are used as a direct input parameter for TMF lifetime prediction are shown in Figure 5.19.
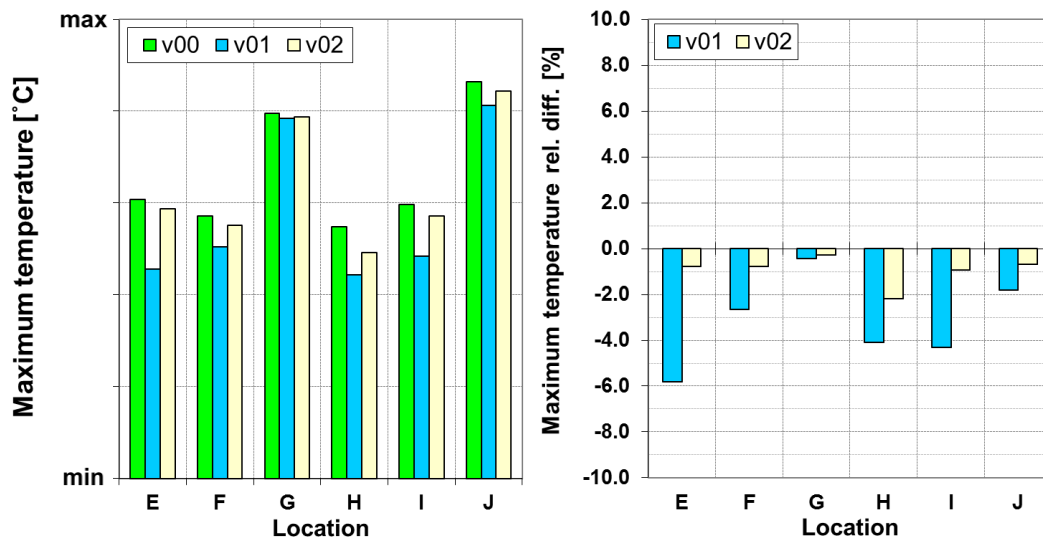
Figure 5.19. Critical locations data comparison - maximum temperature

Maximum temperature relative differences depicted in Figure 5.19. range up to 6% between v00 and v01 and up to 2% between v00 and v02.

In terms of absolute differences, maximum difference of 38 ˚C occurs at critical location E between v00 and v01.

The lowest maximum temperatures at all critical locations are found for front mounted EM variant v01. This corresponds to results of transient heat transfer analyses.

Locations H and I now do not deviate as much from the other locations as was the case with predicted TMF life, stress range and viscoplastic strain range.

All data for critical locations shown graphically in Figure 5.16., Figure 5.17., Figure 5.18., and Figure 5.19. are grouped and shown side by side in Table 5.1.

But before that, it should be noted that at several randomly chosen non-critical locations (not disclosed in this thesis either graphically or in any other form) TMF life significantly increased with the maximum temperature decrease. The improvements seen at some of those locations were even by an order of magnitude. But as was the case with evaluated critical locations, the correlation between temperature drop and predicted TMF life increase was not linear.

Table 5.1. Grouped fatigue evaluation result data for all critical locations

				Fatigue evaluation relevant data at all critical locations				
Loc.	Var.	TMF life N_f [cycles]	Rel. diff.	Stress range [MPa]	Rel. diff.	Viscopl. strain range	Rel. diff.	Max. temp. [°C]	Rel. diff.

Loc.	Var.	TMF life N_f [cycles]	Rel. diff.	Stress range [MPa]	Rel. diff.	Viscopl. strain range	Rel. diff.	Max. temp. [°C]	Rel. diff.
E	v00	800*		**		**		**	
	v01	1400*	70.1%	**	4.3%	**	-60.8%	**	-5.8%
	v02	900*	9.2%	**	-0.6%	**	-9.1%	**	-0.8%
F	v00	2100*		**		**		**	
	v01	3000*	43.1%	**	0.0%	**	-40.7%	**	-2.6%
	v02	2300*	11.1%	**	0.0%	**	-11.9%	**	-0.8%
G	v00	2400*		**		**		**	
	v01	2200*	-8.7%	**	1.4%	**	4.9%	**	-0.4%
	v02	2400*	-0.5%	**	0.2%	**	0.0%	**	-0.3%
H	v00	100*		**		**		**	
	v01	100*	0.8%	**	3.2%	**	-19.7%	**	-4.1%
	v02	100*	0.0%	**	2.4%	**	-10.6%	**	-2.2%
I	v00	200*		**		**		**	
	v01	200*	1.7%	**	4.5%	**	-22.4%	**	-4.3%
	v02	200*	3.4%	**	1.1%	**	-7.1%	**	-0.9%
J	v00	1800*		**		**		**	
	v01	2600*	40.3%	**	2.1%	**	-27.1%	**	-1.8%
	v02	2000*	8.6%	**	1.3%	**	-8.4%	**	-0.7%
		*rounded to the nearest hundred, **classified data							

After the evaluation of all critical locations, it is still not possible to draw one uniform and universal conclusion regarding the influence of ambient HTBC's on predicted TMF life.

In general, it can be concluded that decrease of structural temperature results in better TMF life but the magnitude of that effect highly varies between critical locations.

Huge effect of ambient HTBC's variation on TMF life, where negative relative temperature difference of 6% resulted in a 70% positive difference in predicted TMF life can be seen at location E (and to a lesser extent at locations F and J).

On the other hand, almost the same negative relative temperature difference of 4% shows negligible influence on TMF life at locations H and I (1% and 2% increase).

Location Š G does not correspond well with others, exhibiting the opposite behaviour. Decrease of structural temperature (although slight) resulted in the decrease of predicted TMF life (when the opposite effect is expected).

6. Conclusions and Recommendations for Further Work

6.1. Summary and Main Conclusions

Three main research objectives for this thesis can be identified.

I   To define load cycle and new ambient heat transfer (thermal) boundary conditions which would simulate different engine installation configurations in the engine compartment and apply them to simulation models.

II To investigate the influence of the ambient thermal boundary conditions variation on the structural temperature distribution.

III To investigate the influence of structural temperature variation, imposed by ambient thermal boundary conditions variation, on the exhaust manifold predicted TMF life.

6.1.1. Development and Findings Relating to Research Objective I

Simulated thermo-mechanical loading cycle has been defined. New ambient heat transfer boundary conditions have also been defined and applied to model variants which simulate three standard engine installation configurations.

- Load cycle which simulates the following driving conditions has been defined: 100 km/h highway uphill drive at full load followed by 130 km/h highway downhill drive at motored load and finally stationary vehicle at idle load. Load cycle defined like this is likely to occur sometime during the vehicle's normal operation life.

- Newly defined thermal boundary conditions are based on 3D CFD underhood airflow simulation reports. They account for vehicle speed and engine installation configuration. These thermal boundary conditions are defined using some presumptions and simplifications and this is something which has to be considered when evaluating the results of subsequent analyses.

- Chosen standard engine installation configurations are: transversely oriented engine with front mounted exhaust manifold, transversely oriented engine with rear mounted exhaust manifold and longitudinally oriented engine with side mounted exhaust manifold. The only difference between model variants which simulate those three installation configurations is in the applied ambient thermal boundary conditions.

- Newly defined ambient thermal boundary conditions were applied to ambient surfaces of all three simulated model variants. Even though the application process is based on available 3D CFD reports, some presumptions and simplifications are included in it and this is something to have in mind when evaluating the results of subsequent analyses.

6.1.2. Development and Findings Relating to Research Objective II

Steady state and transient heat transfer analyses were carried out for each model variant. The influence of applied thermal boundary conditions on structural temperature distribution and on overall structural temperature levels is recognized in both steady state and transient heat transfer analyses. Both types of analyses produced results which lead to the same conclusions.

- Differences in both local and global structural temperature distribution between simulated model variants were noticed. This means that the influence of different engine installation configuration on heat transfer process was successfully simulated.
- Calculated structural temperatures were in line with the applied ambient thermal boundary conditions throughout the entire duration of the load cycle.
- Both steady state and transient heat transfer analyses showed that transversely oriented, front mounted exhaust manifold, variant v01 was the coolest one, while the transversely oriented, rear mounted exhaust manifold, (reference) model variant v00 was the hottest one.
- It was also derived that structural temperatures for longitudinally oriented, side mounted exhaust manifold, model variant v02 were between those calculated for v00 and v01.
- Highest temperature differences occur at the end of the motored load because during this loading condition variation of applied ambient thermal boundary conditions is the highest. On the other hand, the smallest temperature differences occur at the end of idle load. This is because applied ambient thermal boundary conditions across variants are almost identical. This means that temperature differences are inherited from the previous motored load.

6.1.3. Development and Findings Relating to Research Objective III

Coupled sequentially thermo-mechanical analyses have been carried out for all three model variants. The results of those analyses were used as input parameters for TMF life evaluation of the exhaust manifold.

- After TMF fatigue life evaluation, all three simulated model variants showed 6 critical areas on the exhaust manifold where predicted TMF life is below the allowed limit of 3000 cycles determined for this engine. The exact locations of all 6 critical areas on all variants are similar, which means that damage mechanism remained principally the same for all variants.

- Reference model variant v00, as generally the hottest one, predicted the lowest number of cycles until crack initiation at all locations except one (location G).

- Model variant v01, as generally the coolest one, predicted the highest number of cycles until crack initiation at all locations except one (location G).

- Model variant v02 predicted slightly better TMF life than the one predicted by the reference variant v00 at all locations except one (location G).

- In general, it can be concluded that decrease of structural temperature results in better TMF life but the magnitude of that effect highly varies between critical locations. Critical locations whose TMF life is highly influenced by the local stiffness effects remain "immune" to ambient thermal boundary conditions variation.

6.1.4. Main Conclusions

- TMF life at critical locations is not influenced only by the level of structural temperatures. It is also highly influenced by the local stiffness effects and global behaviour of the exhaust manifold and the components interacting with it.

- In general, better cooling of the exhaust manifold (as was the case in model variant v01) decreases maximum structural temperature levels and generally results in longer TMF life (except at critical locations which are highly influenced by the local stiffness effects). In one extreme case, relative temperature reduction of 6% (38 ˚C) resulted in 70% relative increase of predicted TMF life. In particular, this can be expected in cases where the temperature is near the maximum allowed temperature for the given material.

- By changing only the thermal boundary conditions, predicted TMF life at non-critical locations can be significantly extended (even by an order of magnitude).

- Current workflow procedure, by which the reference variant v00 was simulated, proved to be the most conservative approach This puts the engineers in a better position since they are working with higher margin of safety.

- Since the influence of engine installation configuration and exhaust manifold position in the engine compartment can be significant with regards to TMF life, the test bed setup should enable consideration of real-life ambient conditions and underhood airflow effects.

6.2. Recommendations for Further Work

Since TMF life prediction is a very broad and complex topic, there was always a possibility that the amount of work and time put into this thesis will not be enough to answer all questions raised by this research.

Therefore, some directions and ideas which could improve and deepen this research are laid out for any potential continuation of this research.

- In the end, complete understanding of influence of thermal boundary conditions variation on predicted TMF life remains somewhat limited. The main reason is that the work done in the scope of this thesis provided "relatively small amount of data". But this "relatively small amount of data" is meant in a sense that all analyses and evaluations are carried out only for one internal combustion engine model. In order to get a better understanding on this topic, one way to continue this research is to carry out the same evaluations on more internal combustion engines. This would produce larger amount of data and perhaps more general conclusions could be drawn then.

- Another remark, regarding any potential continuation of this work, is that applied convective thermal boundary conditions should be calculated by 3D CFD underhood airflow simulation for those exact load cases which will be simulated in the TMF life evaluation. Such calculated convective thermal boundary conditions should be also mapped to engine model surfaces and not applied "manually". This would eliminate the need for any presumptions and simplifications which were used to define and apply thermal boundary conditions in the scope of this thesis.

References

[1] Zieher, F.; Langmayr, F: Engine Simulation in View of Reduced Development Time, FISITA Conference Proceedings, Paper Number F02V081

[2] Beykirch, R., Fritsch, M.: Automatic Structural Optimization of Engine Components in an early Phase of the Design Cycle by using ABAQUS & TOSCA, AUC, 2007. Retrieved on 02.12.2016. from
http://www.ssanalysis.co.uk/hs-fs/hub/419567/file-1584997131-pdf/KB_Papers/ Optimisation_of_Engine.pdf?t=1486127748461

[3] Siefert, T., Riedel, H.: Lifetime Models for High Temperature Components, FISITA - AutoTechnology, Volume No. 7, 2007.

[4] Tonković, Z.: Numerical Analysis of Structures – Lecture Notes (in Croatian), Faculty of Mechanical Engineering and Naval Architecture, Zagreb, 2015.

[5] Spakovszky, S. Z., et al.: Chapter 16.1 Heat Transfer Modes from 16. Unified: Thermodynamics and Propulsion, retrieved on 07.12.2016. from
http://web.mit.edu/16.unified/www/FALL/thermodynamics/notes/node115.html

[6] Robin, A.: Modes of Heat Transfer – Conduction, Convection & Radiation, retrieved on 07.12.2016. from
http://www.spectrose.com/modes-of-heat-transfer-conduction-convection-radiation.html

[7] Galović, A.: Termodinamika 2 (in Croatian), Faculty of Mechanical Engineering and Naval Architecture, Zagreb, 2010.

[8] Sorić, J.: Nonlinear Numerical Analysis of Structures – Lecture Notes (in Croatian), Faculty of Mechanical Engineering and Naval Architecture, Zagreb, 2016.

[9] Pilipenko, A., Computer Simulation of Residual Stress and Distortion of Thick Plates in Multi-electrode Submerged Arc Welding. Their mitigation techniques, Norwegian University of Science and Technology, Trondheim, 2001.

[10] Putar, F.: Numerical Analysis of Welding Residual Stresses and Deformations - Master's Thesis (in Croatian), Faculty of Mechanical Engineering and Naval Architecture, Zagreb, 2014.

[11] Seleš, K.: Numerical Simulation of Welding Process in Large Structures - Master's Thesis (in Croatian), Faculty of Mechanical Engineering and Naval Architecture, Zagreb, 2016.

[12] Lecture 5: Stress-Strain Material Laws from ASEN 3112: Structures, Department of Aerospace Engineering Sciences, University of Colorado at Boulder, retrieved on 09.12.2016. from

http://www.colorado.edu/engineering/CAS/courses.d/Structures.d/IAST.Lect05.d/IAST.Lect05.index.html

[13] Yield surfaces.svg, file retrieved on 10.01.2017. from

https://en.wikipedia.org/wiki/File:Yield_surfaces.svg

[14] Shorr, F. B.: Thermal Integrity in Mechanics and Engineering, Springer - Verlag Berlin Heidelberg, 2015.

[15] Föll, H.: Iron, Steel and Swords script, Chapter: Thermal and Residual Stress, retrieved on 12.12.2016. from

http://www.tf.uni-kiel.de/matwis/amat/iss/kap_8/illustr/s8_4_4.html

[16] Tonković, Z.: Damage and Fracture Mechanics – Lecture Notes (in Croatian), Faculty of Mechanical Engineering and Naval Architecture, Zagreb, 2016.

[17] Čanžar, P.: Experimental and Numerical Modelling of Fatigue Behaviour of Nodular Cast Iron – Doctoral Thesis (in Croatian), Faculty of Mechanical Engineering and Naval Architecture, Zagreb, 2012.

[18] Weicheng, C.: A State-of-the-art Review on Fatigue Life Prediction Methods for Metal Structures, School of Naval Architecture and Ocean Engineering, Shanghai Jiao Tong University, Shanghai, China, 2002.

[19] fe-safe User Manual, Fatigue Theory Reference Manual, Dassault Systèmes

[20] Tonković Z., et al.: Experimental and Numerical Modelling of Deformation Processes of Nodular Cast Iron, IKM, Hannover, 2015.

[21] Kujawski, D.: Fatigue Failure Criterion Based on Strain Energy Density, Politechnika Warszawska, Journal of Theoretical and Applied Mechanics, Warsaw, 1989.

[22] Churkaluk, E.; Constantinescu, A: An Energetic Approach in Thermomechanical Fatigue for Silicon Molybdenum Cast Iron, Materials at High Temperatures Volume 17, 2000. - Issue 3

[23] Matteis, P., et al.: High Temperature Fatigue Properties of a Si-Mo Ductile Cast Iron, 20th European Conference on Fracture (ECF20), Elsevier 2014.

[24] Thermal Mechanical Technical Background, eFatigue LLC, retrieved on 04.01.2017., from

https://www.efatigue.com/hightemp/background/tmf.html

[25] Gocmez, T.; Deuster, U.: Designing Exhaust Manifolds Using Integral Engineering Solutions, retrieved on 21.12.2016. from

http://www.fev.com/fileadmin/user_upload/Media/TechnicalPublications/Design/Exhaust ManifoldDesign.pdf

[26] Comini, G., et al.: Finite Element Analysis in Heat Transfer: Basic Formulation & Linear Problems, Taylor & Francis, Udine, Italy, 1994.

[27] Brannon, R. M.: Geometric Insight into Return Mapping Plasticity Algorithms – Draft (30.07.2002.), retrieved on 19.12.2016. from

https://classes.soe.ucsc.edu/cmps161/Winter14/papers/t4/RelatedWork/RadialReturn.pdf

[28] Huang, J.; Griffiths, D. V.: Return Mapping Algorithms and Stress Predictors for Failure Analysis in Geomechanics, Journal of Engineering Mechanics, vol. 135, Issue 4, April 2009.

[29] Nicouleau, E., et al.: Structural Calculation and Lifetime Prediction in Thermomechanical Fatigue of Engine Components, Elsevier, 2002.

[30] Smolnikar, M.: AVL TMF Lifetime Prediction – Unpublished internal document, AVL List GmbH, released on 06.06.2013.

[31] ABAQUS 6.14., Documentation, Dassault Systèmes

[32] Sorić, J.: Metoda konačnih elemenata (in Croatian), Golden marketing, Zagreb, 2004.

[33] Cook, R. D.: Finite Element Modeling for Stress Analysis, John Wiley & Sons, USA, 1994.

[34] Tetrahedral elements available in ABAQUS for structural analysis? When to use what?, Optimec Consultants inc., retrieved on 16.12.2016. from

http://optimec.ca/news/tetrahedral-elements-available-abaqus-structural-analysis-use/

[35] Galović, A.: Odabrana poglavlja iz kondukcije (in Croatian), Faculty of Mechanical Engineering and Naval Architecture, Zagreb, 2003.

[36] Audi A8 L W12 : 2011, retrieved on 12.04.2017. from

http://cartype.com/pics/8110/full/audi_a8l_w12_s-t_draw_11.jpg

[37] TurboSquid, 3D Models for Professionals, Car Engine 2 by 3d_molier, retrieved on 12.04.2017. from

https://www.turbosquid.com/3d-models/car-engine-3d-model/720097

Appendix

I.   CD-R disc